國立交通大學

材料科學與工程研究所

博 士 論 文

奈 米 碳 材 料 之 場 發 射 特 性 與 應 用 之 研 究

Study of Field Emission Characteristics and Applications on

Carbon Nanomaterials

研 究 生：徐振航

指導教授：陳家富、黃華宗　教授

中 華 民 國 九 十 六 年 十 一 月

奈米碳材料之場發射特性與應用之研究

Study of Field Emission Characteristics and Applications on

Carbon Nanomaterials

研 究 生：徐振航　　　　Student：Cheng-Hang Hsu

指導教授：陳家富、黃華宗　　Advisor：Chia-Fu Chen、Wha-Tzong Whang

國 立 交 通 大 學

國立交通大學材料科學與工程研究所

博 士 論 文

A Thesis

Submitted to Department of Materials Science and Engineering

College of Engineering

National Chiao Tung University

In partial Fulfillment of the Requirements

For the Degree of Doctor of Philosophy

In Materials Science and Engineering

Nov. 2007

Hsinchu, Taiwan, Republic of China

中華民國九十六年十一月

奈米碳材料之場發射特性與應用之研究

研究生：徐振航　　　　　　　　　　指導教授：陳家富、黃華宗

國立交通大學材料科學與工程研究所　博士班

摘　要

在此篇論文中，將對奈米碳材的合成以及其在場發射的應用端做一番探討與研究。為了得到最佳效能，應用在場發射的材料必須具有高傳導性、高深寬比、好的均勻性以及耐久性。雖然奈米碳管(Carbon nanotubes, CNTs)的特性已經被研究多年，在場發射(Field emission)應用的效能以及技術上仍有許多值得探討的空間。事實上為了符合發射極的需求，各式各樣的奈米材料都可供選擇，然而考慮到將製程簡單化以及化合物的多樣性，使用碳材作為發射極不但具有多種的合成方式，也隨之有不同的表現。因此在本研究中，重點將討論奈米碳管以及奈米碳尖的合成技術以及改質之後的特性。

在合成奈米碳材的製程中，主要是以偏壓輔助微波電漿化學氣相沈積的方式(MPCVD)，在裝置中通入氫氣（H_2）、甲烷(CH_4)的氣體反應而成。藉由使用催化劑如鐵(Fe)、鉻(Cr)及鎳(Ni)，不同型態與特性的奈米碳管可以被合成。除了材料本身的特性，為了更進一步增加場發射的效能，如何控制奈米碳管密度的製程以及其特性的測量更顯重要。除此之外，本論文也成功合成新奈米碳材，如奈米碳尖錐以及自組裝碳化鉻奈米碳尖錐(chromium carbide capped carbon nanotips)之合成技術。值得一提的是，這些奈米碳材表現出全然不同的表面型態及特性。對於奈米碳尖來說，其超尖端(0.1nm)的形狀促使其可在較低的電場中(1.4V/μm)啟動，而自組裝碳化鉻奈米碳尖錐來說，則能得到更穩定的場發射電流。

為了達到實際應用，具有閘電極的元件也被製造出來，在其中探討不同元件材料對成長奈米碳材料上的優缺點。最後藉由自組裝奈米探尖錐的優異特性，將其成功的成長於元件中而得到低的驅動電壓(2.6V/μm)特性。

Study of Field Emission Characteristics and Applications on Carbon Nanomaterials

Student：Cheng-Hang Hsu   Advisor：Dr. Chia-Fu Chen

Dr. Wha-Tzong Whang

Institute of Material Science and Engineering

National Chiao Tung University

ABSTRACT

In this thesis, synthesis of carbon nanomaterials were discovered and studied. The major applicable characters are focus on the field emission applications. To achieve optimizing performance, nanomaterials have to be with good conductivity, high aspect ratio, good uniformity and good durability. Carbon nanotubes, know for their novel properties, have been studied for more than a decade. For field emission applications, there are still works to be done to improve the performance and fabrication techniques. In fact, to meet the claims for an emitter, various kinds of nanomaterials are also good candidates. Due to the simplicity of the synthesis and diversity of compounds, carbon materials could be synthesized into various forms and characteristics. In this study, nanomaterials including CNTs and carbon nanotips were synthesized and major modifications to their morphologies were carried out to understand the characteristics. The nanomaterials were synthesized utilizing bias-assisted microwave plasma chemical vapor deposition (MPCVD) using H_2/CH_4 as reaction gases.

Carbon nanotubes were synthesized using catalysts including Fe, Cr and Ni; each one shows unique surface morphology and field emission behavior. Except the intrinsic properties of the CNTs, to further more improve the field emission efficiency, density reduced CNTs

were synthesized and measured. Besides, new kids of nanomaterials including bare carbon nanotips and chromium carbide capped carbon nanotips were synthesized. These nanomaterials show entirely different surface morphologies and characteristics. For bare carbon nanotips the ultra-sharp tip (0.1nm) makes it to turn-on at a low electric field (1.4V/µm). For chromium carbide capped carbon nanotips, the chromium carbide contributes to a more stable emission current.

To achieve practical applications, fabrication of gated structure was also carried out. The suitable materials for the devices are used for fabrication and the advantages and disadvantages are studied. Due to the superior properties, selective growth of chromium carbide capped carbon nanotips were synthesized in the gated structure and low driving voltage (2.63V) of the field emission could be obtained.

致　　謝

Content

List of Tables

List of Figures

Chapter 1 Introduction

1.1 Foreword

With the developments of semiconductor technology, quality of life has been promoted enormously. Consumer products, for example, cell phone, flat panel display, computer, etc., have already become indispensable in our daily life and are vital to global economy. Claims of the consumer products, including light in weight, slim in dimension and efficient in energy consumption are all constantly improved. Most improvement of the mentioned performances come mainly from great developments of fabrication techniques that follow the Moore's Law[1] which was already a prediction over 40 years ago. The improvements of the semiconductor fabrication techniques will no doubt facing a choke point in the near future. Nanotechnology, defined as the dimension of the material less than 100nm, is the key to the next generation of fabrication techniques.

Wealth of interesting and new phenomena are associate with nanometer-sized structures, with the best established examples including size-dependent excitation or emission[2], quantized (or ballistic) conductance[3], coulomb blockade (or single electron tunneling, SET) [4], and metal-insulator transition[5]. It is generally accepted that quantum confinement of electrons by the potential wells of nanometer-sized structures may provide one of the most powerful means to control the electrical, optical, magnetic and thermoelectric properties of a solid-state functional material. Differ from the current fabrication techniques, which are top-down processes,[6] require sophisticated state-of-the-art steps. Instead, a bottom-up process is the spirit of the nanotechnology. Bottom-up (or self-assembly)[7,8] approaches to nanofabrication utilizing chemical or physical energies operating at the nanoscale to assemble basic units into microscopic larger structures. As component size decreases in fabrication, bottom-up technologies provide increasingly important complement to top-down techniques.

Applications are predicted to involve with nanotechnology including optics,[9]

electronics[10], catalyst,[11] ceramics,[12] and storage media,[13,14] etc. Among all the consumer products, for example, cell phone, television and signboard, each is equipped with a display. Display technologies may include electronic fabrication (e.g. IC circuits), optical technology (e.g. backlight, polarizer) or plasma technology (PDP) that makes it always a challenging technology. And also the increasingly choosy claims of display, for example, high contrast, high brightness and power efficiency, new generations of displays are ceaselessly produced. Currently, the LCD and PDP dominate the market, but there are plenty of improvements need to be done. An FED has all the advantages of a display except the fabrication process and cost. The key lies in successful synthesis of nano-emitters to meet the field emission and mass-production requirements.

1.2 Motivation

The major study of this thesis is based on field emission device which may be applied to electron source, magnetron or most important, field emission display. Since the discovery of carbon nanotubes, vast efforts were made not only on carbon nanotube itself but all other pure or compound materials. From the first Mo tips, Si tips, and diamond tips, to carbon nanotubes nowadays, performance of each material progresses even better. The basic demands for a field emitter have to be with low work function, high aspect ration and small tip radius. One goal of this thesis is to synthesis new kinds of nanomaterials which are able to fit the requirements.

Besides, in order to achieve particle application, issues of field emission stability, efficiency and device fabrication should also be concerned. Therefore, we put efforts to further improve current nanomaterials as carbon nanotubes, by changing the catalyst used and the surface morphology. To achieve practical applications, we intended to fabricate the gated structure and synthesize nanomaterials inside to investigate the field emission properties.

Chapter 2   Fundamental Theory and Literature Review

2.1 Introduction to Carbon Materials

Carbon is the lightest element in the 4th group elements, which has unique properties comparative with other elements. More then 500,000 compounds are identified, which are greater than the sum of the other elements. Besides organic structure, which is about 80% among the 500,000 compounds, carbon appears in several kinds in nature. Fig. 2.1 shows various atomic structure of carbon. Zero-dimensional carbon, such as fullerence, was identified by Kroto et al.,[15] also lead to the discovery of carbon nanotubes.[16] One-dimensional carbon, such as nanotube discovered by Iijima, exhibit amazing behaviors and attracts a lot of attentions. Two-dimensional carbon, such as graphite, and 3-dimensional carbon, as diamond, bonds in sp^2, bonds in sp^3, respectively, have already been study widely and extensively. Carbon has an electronic structure of $1s^2\, 2s^2\, 2p^2$. The 2s and 2p wave functions are normally hybridized to form 4 degenerate orbitals in a sp^3 hybridized atom. These carbon-carbon bonds with high strength, for example, the bond strength of a C-C single bond has a value of 356kjmol^{-1} compared to a value of 226kjmol^{-1} for the equivalent Si-Si bond. This makes it possible to form carbon chains of phenomenal lengths, which is a property that allows materials such as carbon fibers to be produced. Since the discovery of carbon nanotubes, unique and novel draw great attentions and efforts in the exploitation of application. Carbon related nanomaterials are considered as the first candidate for nanoscale applications.

In this thesis, application of field emission is the basis point. Therefore, one dimension carbon nanomaterials are concerned to investigate the properties and applications. The following are some introductions to these nanomaterials including carbon nanotubes, carbon nanofibers and carbon nanotips.
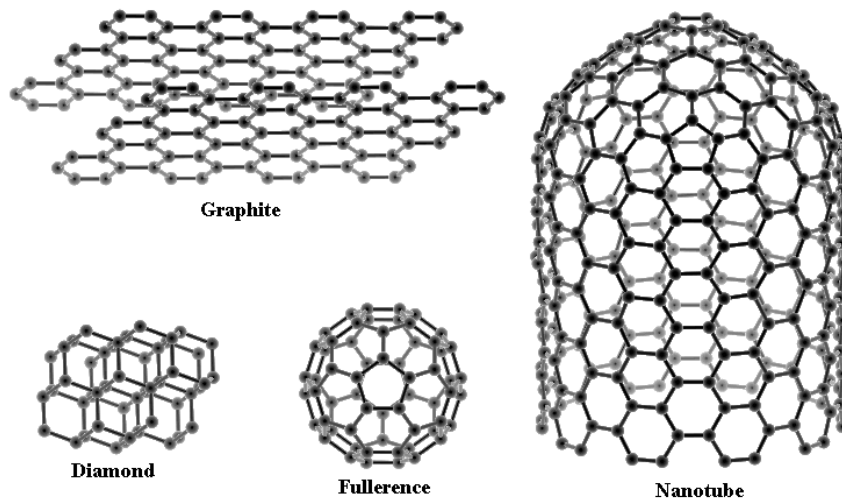
Fig. 2.1 Various atomic structure of carbon: fullerence, graphite, diamond, and nanotube.
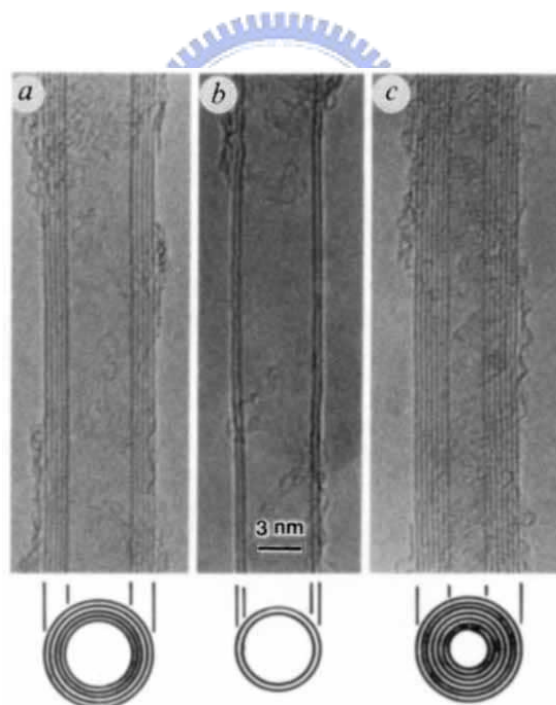
Fig. 2.2 TEM images of CNTs. The parallel lines correspond to the (002) lattice images of graphite. Cross-section images are illustrated in, (a) tube consisting five graphitic sheets with diameter of 6.7nm, (b) tube consisting two graphitic sheets with diameter of 5.5nm and (c) tube consisting seven graphitic sheets with diameter of 6.5nm[16].

2.1.1 Carbon Nanotubes

Figure 2.2 shows typical electron microscopy images of carbon nanotubes. Since the first observation of multi-wall carbon nanotubes (MWNTs) by Iijima,[16] much attraction has been drawn because of their excellent physical properties and potential applications in various fields. For example, carbon nanotube is probably the best conductor of electricity that can ever be possible.[17-19] Carbon nanotube has comparable thermal conductivity with diamond along the tube axis[20]. With the total area per nanotube bundle for normalizing the applied stress, the calculated Young's modulous for an individual (10,10) nanotube is ~0.64 TPa.[21] Strong van der Waals attraction leads to spontaneous roping of many nanotubes which is important in certain applications.

The structural and electrical properties of CNTs could be found in articles[22-25] and book.[26-28] A CNT consists of either one cylindrical graphene sheet (Single-walled carbon nanotube, SWCNT) or several nested cylinders with an inter-layer spacing of 0.34 - 0.36 nm (Multi-walled carbon nanotube, MWCNT). Figure 2.3 shows the cutting graphite sheet along the dotted lines which connects two crystalline graphite equivalent sites on a 2-D.[29] The circumference of CNTs can be expressed in term of the chiral vector, C_h, and chiral angle, θ. The chiral vector is given by Eq. (1):

$$C_h = na_1 + ma_2 \equiv (n,m) \qquad (n, m \text{ are integers}, 0 \leqq |m| \leqq n) \tag{1}$$

where a_1 and a_2 are the primitive vectors length of which are both equal to $\sqrt{3}\ l_{C\text{-}C}$, with $l_{C\text{-}C}$ is the length of C-C bond. The chiral angel determines the amount of twist in the tube. The chiral angles exist two limiting cases that are at 0° and 30°. The chiral angle is defined in Eq. (2) as

$$\cos\theta = \frac{C_h \cdot a_1}{|C_h| \cdot |a_1|} = \frac{2n + m}{2\sqrt{nm + m^2 + n^2}} \tag{2}$$

The zig-zag CNT corresponds to the case of m = 0, and the armchair CNT corresponds to

the case of n = m. The chiral CNT corresponds to the other (n, m) chiral vectors. The zig-zag

CNT (n, 0) is generated from hexagon with θ= 0°, and armchair CNT (n, n) is formed from

hexagon with θ= 30°. The chiral CNT is formed from hexagon with 0°＜θ＜30°. The

inter-atomic spacing of carbon atom is known so that the rolled up vector of CNT can define

the CNT diameter. The properties of carbon CNTs depend on the atomic arrangement,

diameter, length, and the morphology.[30]

There are many possibilities to form a cylinder with a graphene sheet[33] and a few

configurations are shown in Fig. 2.4. Figure 2.4(a)-(c) are SWCNTs of (a) zig-zag, (b)

armchair and (c) chiral type. Figure 2.4(d) represents a MWCNT formed by four tubes of

increasing diameter with a layer spacing of 0.34 nm. One can roll up the sheet along one of

the symmetry axis: this gives either a zig-zag tube, or an armchair tube. It is also possible to

roll up the sheet in a direction that differs from a symmetry axis: one obtains a chiral CNT.

Besides the chiral angle, the circumference of the cylinder can also be varied.

This diversity of possible configurations is indeed found in practice, and no particular

type is preferentially formed. In most cases, the layers of MWCNTs are chiral[31,16] and of

different helicities.[32] The lengths of SWCNTs and MWCNTs are usually well over 1 μm and

diameters range from ~1 nm (for SWCNTs) to ~50 nm (for MWCNTs). Pristine SWCNTs are

usually closed at both ends by fullerene-like halfspheres that contain both pentagons and

hexagons.[33]

The electronic properties of SWCNTs have been studied in a large number of theoretical

works.[33,34,35-37] These models show that the electronic properties vary in a calculable way

from metallic to semiconducting, depending on the tube chirality (n, m) given by[26]

Metallic properties: n-m = 0 or (n-m)/3 = integer

Semiconducting properties: (n-m)/3 ≠ integer

The study shows that about 1/3 of SWCNTs are metallic, while the other 2/3 of SWCNT

are semiconducting with a band gap inversely proportional to the tube diameter. This is due to

the very unusual band structure of graphene and is absent in systems that can be described with usual free electron theory. Graphene is a zero-gap semiconductor with the energy bands of the p-electrons crossing the Fermi level at the edges of the Brillouin zone, leading to a Fermi surface made of six points.[38] Graphene should show a metallic behavior at room temperature since electrons can easily cross from the valence to the conduction band. However, it behaves as a semi-metal because the electronic density at the Fermi level is quite low. Rolling up the graphene sheet into a cylinder imposes periodic boundary conditions along the circumference and only a limited number of wave vectors are allowed in the direction perpendicular to the tube axis. When such wave vectors cross the edge of the Brillouin zone, and thus the Fermi surface, the CNT is metallic. This is the case for all armchair tubes and for one out of three zigzag and chiral tubes. Otherwise, the band structure of the CNT shows a gap leading to semiconducting behavior, with a band gap that scales approximately with the inverse of the tube radius. Band gaps of 0.4-1eV can be expected for SWCNTs (corresponding to diameters of 1.6-0.6nm). This simple model does not take into account the curvature of the tube which induces hybridization effects for very small tubes and generates a small band gap for most metallic tubes. The exceptions are armchair tubes that remain metallic due to their high symmetry.

These theoretical predictions made in 1992 were confirmed in 1998 by scanning tunneling spectroscopy.[39,40] The scanning tunneling microscope has since then been used to image the atomic structure of SWCNTs,[41,42] the electron wave function[43] and to characterize the band structure.[44] Numerous conductivity experiments on SWCNTs and MWCNTs yielded additional information.[45-56] At low temperatures, SWCNTs behave as coherent quantum wires where the conduction occurs through discrete electron states over large distances. Transport measurements revealed that metallic SWCNTs show extremely long coherence lengths.[56,57] MWCNTs show also these effects despite their larger diameter and multiple shells.[58,59]
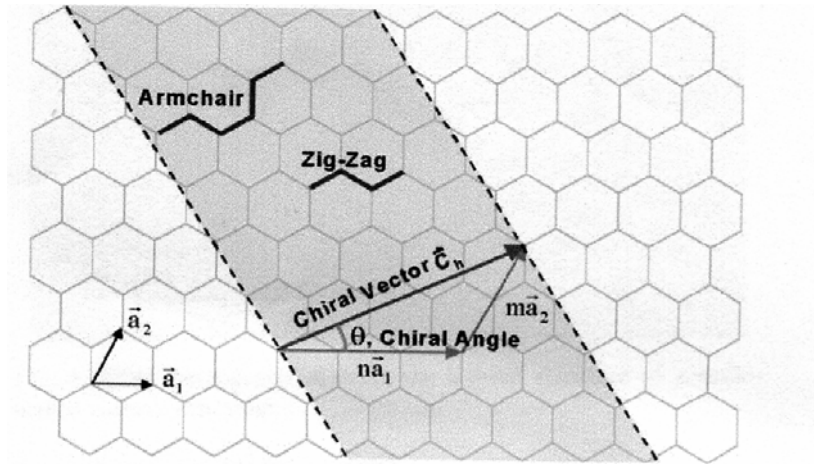
Fig. 2.3   Schematic diagram showing how a hexagonal sheet of graphite is rolled to form a CNT[29].
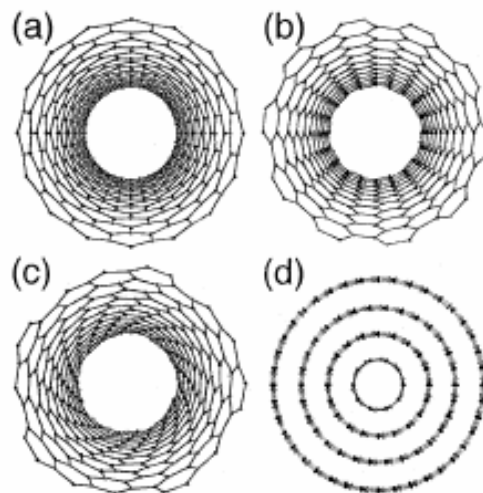
Fig. 2.4 Models of different CNT structures[60].
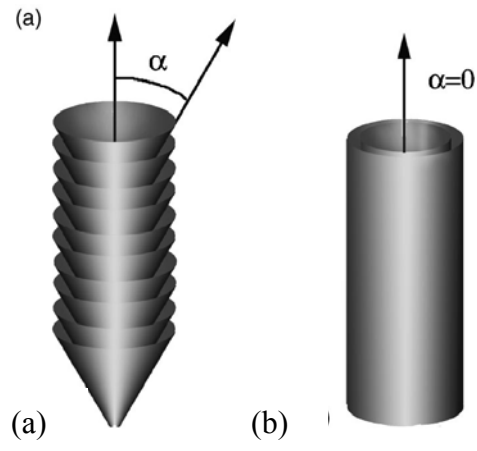
Fig. 2.5 Structure of carbon nanofibers and nanotubes. (a) stacked cone sherringboned nanofiber and (b) nanotube[68].
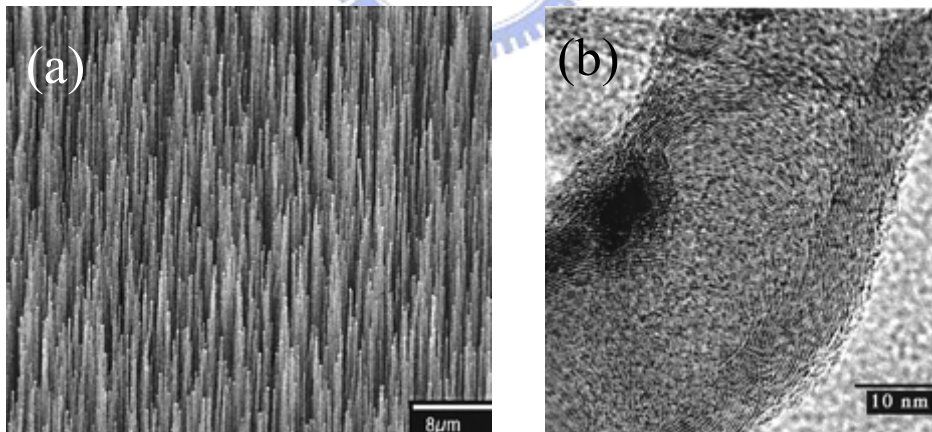
Fig. 2.6 (a) SEM image of carbon nanofiber and (b) TEM image of an individual carbon nanofiber[66].

2.1.2 Carbon Nanofibers[61]

It has been known for over a century that filamentous carbon can be formed by the catalytic decomposition of carbon-containing gas on a hot metal surface. In a U.S. Patent published in 1889,[62] it is reported that carbon filaments are grown from carbon-containing gases using an iron crucible. In the current literature, the term "nanofiber" is preferentially used, featuring distinction in size scale, while in the past simply "filamentous carbon," "carbon filaments," and "carbon whiskers" were applied.[63] In 1985 a form of carbon, buckminsterfullerene C_{60}, was observed by a team headed by Kroto et al.,[64] which led to the Nobel Prize in chemistry in 1997. This discovery was followed by Iijima's[16] demonstration in 1991 that carbon nanotubes are formed during arc-discharge synthesis of C60 and other fullerenes, triggering a deluge of interest in carbon nanofibers and nanotubes. In the 1990s the introduction of catalytic plasma-enhanced chemical vapor deposition (C-PECVD) provided additional control mechanisms over the growth of carbon nanostructures. In 1997 Chen et al. used PECVD for nanofiber synthesis.[65] Their work was followed by the better known work of Ren et al.[66]

Carbon nanofibers (CNFs) are cylindrical or conical structures that have diameters varying from a few to hundreds of nanometers and lengths ranging from less than a micron to millimeters. The internal structure of carbon nanofibers varies and is comprised of different arrangements of modified graphene sheets. A graphene layer can be defined as a hexagonal network of covalently bonded carbon atoms or a single two-dimensional (2D) layer of a three dimensional (3D) graphite. In general, a nanofiber consists of stacked curved graphite layers that form cones [Fig. 2.5(b)] or "cups."[67,68] The stacked cone structure is often referred to as herringbones or fishboned as their cross-sectional transmission electron micrographs resemble a fish skeleton, while the stacked cups structure is most often referred to as a bamboo type, resembling the compartmentalized structure of a bamboo stem. Currently there is no strict

classification of nanofiber structures. The main distinguishing characteristic of nanofibers from nanotubes is the stacking of graphene sheets of varying shapes.

In comparison to carbon nanotubes, carbon nanofibers appear as rod-like in structure, as shown in Fig. 2.6.[69,70] Several methods are used for synthesizing carbon nanofibers, such as microwave plasma chemical vapor deposition, hot filament chemical vapor deposition, plasma enhanced chemical vapor deposition, etc. Catalyst is usually the essential element for the growth of carbon nanofibers. Gated field emission devices using single carbon nanofiber cathodes has also been reported.[71]

2.1.3 Carbon Nanotips

A carbon nanotip has a solid carbon structure which may be ether amorphous or graphite. Compare to its root part, the diameter of its head is much smaller and normally less than 10nm. Both amorphous carbon and graphite are considered conducting metallically;[72] therefore, combine with its small radii, it is suitable for applications as field emitters.[73] Other applications such as scanning probe microscope tips and nano indenters[74] are also proposed mainly due to the chemical inertness of the carbon surface, and much higher bending stiffness compared to carbon nanotubes.

Different growth methods for fabricating carbon nanotips may include electron–beam -induced deposition (EBID),[75-77] chemical vapor deposition (CVD),[78–80] and plasma-enhanced chemical deposition (PECVD).[81] In our previous work, well aligned carbon nanotips are grown on both bare silicon and platinum film by microwave plasma chemical vapor deposition.[82-83] Generally, the growth of carbon nanotips needs no catalyst, so the top of the tip is only amorphous carbon or graphite. Fig. 2.7 (a) shows SEM plane view image of carbon nanotips, the tip angle is 29°. Fig. 2.7(b) shows TEM image of a single carbon nanotip, the image shows a sharp tip of graphite structure. Fig. 2.7(c) shows the field emission behavior that turns on at low electric field.
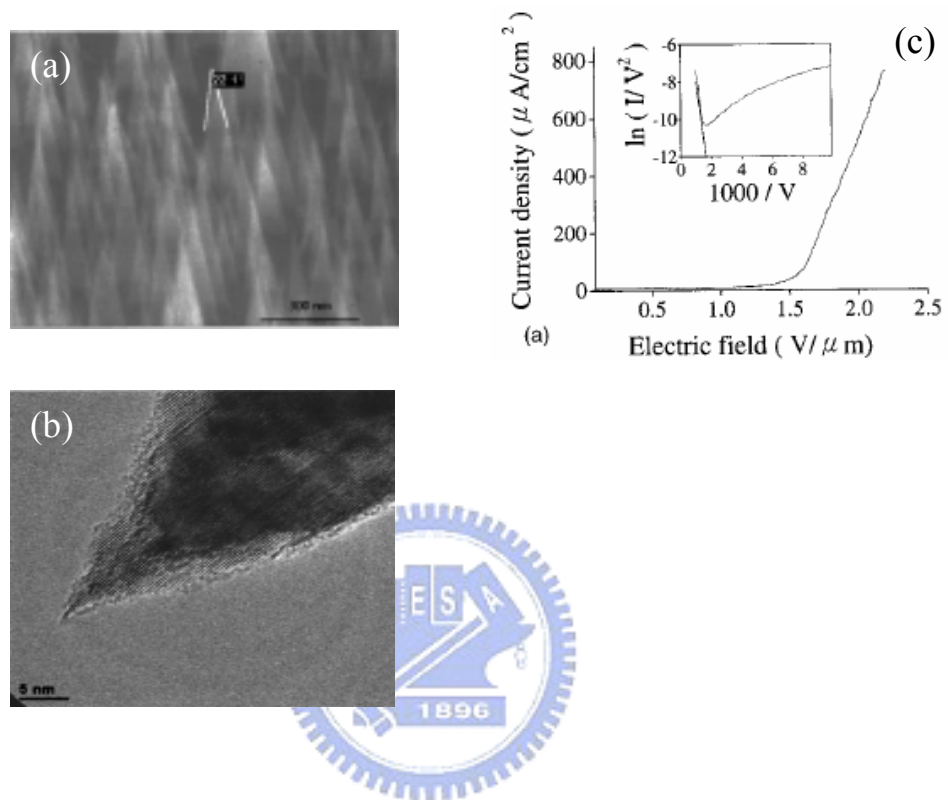
Fig. 2.7 (a) top-view of SEM image of carbon nanotips, (b) a single carbon nanotip TEM image and (c) field emission property of carbon nanotips[83].

2.2 Methods for Synthesizing Carbon Materials

Arc Discharge

Arc discharge is the first and the effective way to produce single-wall carbon nanotubes (SWNTs) and multi-wall carbon nanotubes (MWNTs).[84-86] The arc discharge equipment contains a stainless steal vacuum chamber with about 500 torr pressure filled with Helium. Two separated graphite electrode are biased with high current density (50~150A) to about 25~40V. Arc is then induced, and the graphite target is vaporized. Products are deposited on cathode or chamber which includes fullerence, tubes, nano particles and amorphous carbon, etc. Impurities are one of its disadvantages, which need further purifications. Figure 2.8 shows schematic diagram of typical arc discharge equipment.[87]

Laser Ablation

Smalley et al.[88,89] discovered that single-wall carbon nanotubes can be produced by laser ablation with good quality and efficiency, which draws a lot of attention. A carbon target is evaporated by high power continuous CO_2 laser or pulse Nd:YAG laser source. The evaporated species are carried out by Argon or Helium to the water-cooled copper finger or copper wire; single-wall nanotubes are then formed. One specialty is that no amorphous carbon is formed on nanotubes. It has to be noted that, fullerence and multi-wall nanotubes can also be obtained by this method. Fig. 2.9[90] shows schematic diagram of laser ablation equipment.
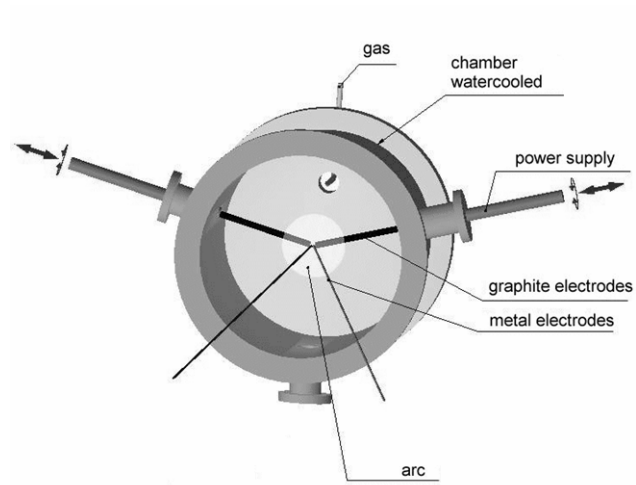
Fig. 2.8 Schematic diagram of arc discharge equipment (Krätschmer-Huffmann).
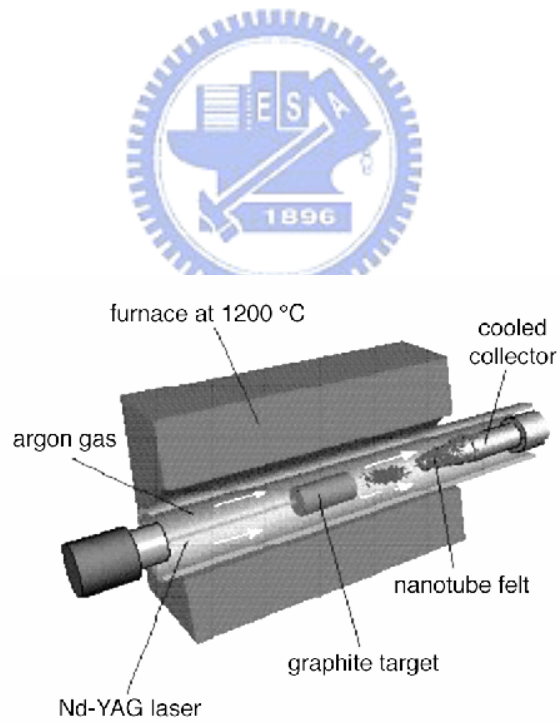
Fig. 2.9 Oven laser-vaporization apparatus[90].

Chemical Vapor Deposition (CVD)

Chemical vapor deposition includes thermal CVD, Hot filament CVD, microwave plasma CVD, etc. Catalysts are normally used for the growth of carbon related material. Typically chemical vapor deposition are used for the production of carbon fibers.[91,92] It is not until 1993 that Yacaman et. al.[93] successfully use chemical vapor deposition to deposit carbon nanotubes. And till 1997 microwave plasma enhanced chemical vapor deposition is used to deposit carbon nanofibers and carbon nanotubes.[94,95] Hydrocarbon gases are usually mixed with hydrogen (or ammonia) to be the reaction gas.[96] Products may be carbon nanotubes, amorphous carbon, carbon fiber, or even carbon nano tips, which are correlated to growth temperature, flow rate, reaction gas, growth time, bias, and catalyst. Compare with the methods above, CVD has the advantage of low process temperature, relative good uniformity, convenience, large area growth, and easy for in-situ doping.[97]

Bias Assisted Microwave Plasma Chemical Vapor Deposition (MPCVD)

Microwave plasma chemical vapor deposition is one of the important facilities for thin film deposition, micro manufacturing, and surface treatment.[98] By the advantage of high ion density, high degree of dissociation, high reactivity, and low process temperature, a lot of kinds of substrates are capable of fabrication under low temperature with deposition and etching, which is meaningful for LSI process, microelectronic device, optoelectronic device, polymer, and thin film sensor.

By applying electric field, the reaction gas breakdown to induce electrons and ions. With electromagnetic field obtained by microwave or RF power, more electrons and ions are generated by colliding with the un-dissociated gas. Stable plasma is reached when the generation rate and consumption rate are equal for all species. Unlike traditional thermal plasma, temperature of electrons, ions, and neutral particles in low temperature plasma induced by discharge are not identical. The temperature of electron is about $1000^{\circ}K$, while the

ions and neutral ones are below 500°K. Therefore, low temperature plasma is a non-equilibrium plasma with not only few ions, electrons, but also excite state, transient state, and free radicals. By manipulating these high energy species, reaction which is hard for steady state species are attainable.

Take diatomic plasma for example, the procedure may appear as followed:

(Ⅰ)Ionization $\qquad A_2 + e^- \rightarrow A_2^+ + 2e^-$

(Ⅱ)Dissociative ionization $\quad A_2 + e^- \rightarrow A^+ + A + 2e^-$

(Ⅲ)Attachment $\qquad A_2 + e^- \rightarrow A_2^-$

(Ⅳ)Detachment $\qquad A_2^- + e^- \rightarrow A_2 + 2e^-$

(Ⅴ)Recombination $\qquad A_2^+ + e^- \rightarrow A_2$

(Ⅵ)Atom recombination $\qquad 2A^\bullet \rightarrow A_2$
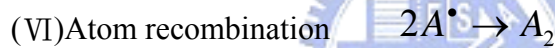
*any polyatomic molecule is substituent for mentioned above.

($^\bullet$) stands for free radical.

Basically, microwave plasma chemical vapor deposition does not need any electrode or even heater. But in this thesis, bias plays an important role in the growth of nanomaterials, and also an essential term.

When a DC bias is added on to the substrate, before the ions pass through the plasma sheath area, the movement of the ions do not effect by the collision between the ions, comparatively and statistically. Also means the ions can strike the substrate directly and vertically by the applied field.[99]

2.3 Growth Mechanism for Nanomaterials

Due to huge amount compound and various atomic bonding of carbon, plenty of kinds of methods are used for the growth of carbon related nanomaterials. Each method has its advantages, disadvantages, distinguishing feature, and a range for suitable use. Most of them have been successfully synthesize carbon nanotubes.

The model used for describing the growth of nanomaterials still is an issue because of the difficulty for observation under such extremely small scale. Even though, several mechanisms are brought up to characterize the behavior for the growth. Here we discuss some growth models which are considered to be the major mechanism for nanosize material.

Growth mechanism of various kind of bottom-up nanosize materials are generally considered to be three models: Vapor-Solid (VS) model, Vapor-Liquid-Solid (VLS) model, and recently, Solution-Liquid-Solid (SLS) model. Some modifications[100] have also been published which will not be discussed here.
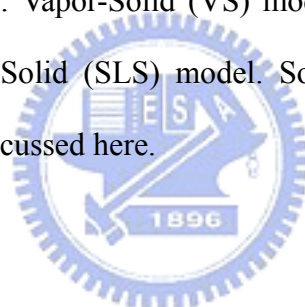
Vapor-Solid (VS) Model

Figure 2.10 shows an approximately growth model of vapor-solid growth mechanism. The diagram takes the growth of GaN for example. Epitaxial growth can be achieved without catalyst or liquid phase. The sum of thermodynamic surface energy and heat of fusion become the driving force for VS growth. The growth rate of VS is dominated by the rate of atoms or molecules diffusion and rearrangement. Compare with the growth mechanism with catalyst, the VS mechanism has a lower growth rate.

Vapor-Liquid-Solid (VLS) Model

The mechanism[101] was first introduced in the 1960s to explain the growth of silicon whiskers or tubular structures[102]. In this model, growth occurs by precipitation from a

supersaturated liquid-metal-alloy droplet located at the top of whisker, into which silicon atoms are preferentially absorbed from the vapor phase. The similarity between the growth of carbon nanotubes and the VLS model has also been pointed out by Saito et al[103-104] on the basis of their experimental findings for multi-walled nanotube growth in a purely carbon environment (Fig. 2.11). Solid carbon sublimates before it melts at ambient pressure, and therefore these investigators suggested that some other disordered carbon form with high fluidity, possibly induced by ion irradiation, should replace the liquid droplet.

Solid-Liquid-Solid (SLS) Model

Figure 2.12[105] shows diagram of solution-liquid-solid growth mechanism which takes Ⅲ-Ⅴ materials for example. No catalyst is used for solution-phase synthesis. The materials are produced as polycrystalline fibers or near-single-crystal whiskers having width of 10 to 150 nanometers and length of up to several micrometers[106]. This mechanism shows that process analogous to vapor-liquid-solid growth operated at low temperatures, while requirement of a catalyst that melts below the solvent boiling point to be its potential limitation.
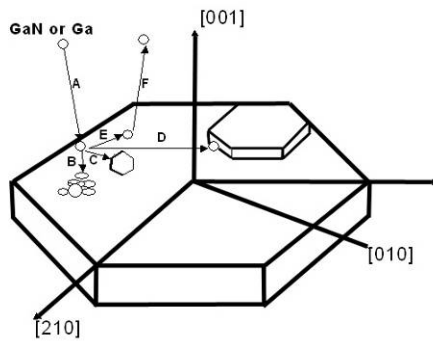
Fig. 2.10 Schematic diagram of vapor-solid (VS) growth model.
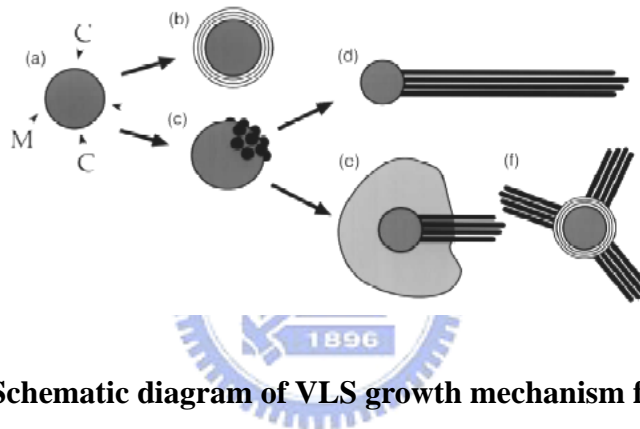
Fig. 2.11 Schematic diagram of VLS growth mechanism for nanotubes.[103]
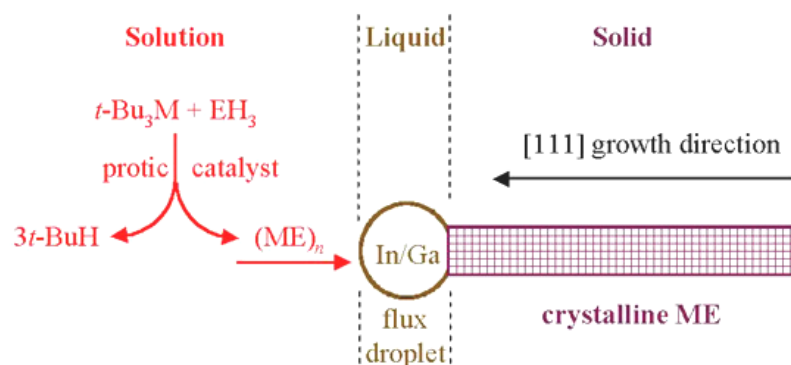
Fig. 2.12 Schematic depiction of SLS growth mechanism.[105]

2.4 Introduction to Field Emission Theory

The science of field emission began in 1928,[109] when Fowler and Nordheim presented the first quantum mechanical model for describing field induced electron emission from a metallic surface; a model still in use today. In deriving their model, Fowler and Nordheim first assumed that the conduction electrons in the emitting metal are describable as a free-flowing 'electron cloud' - following Fermi-Dirac statistics -and are bound to the metal by an energy barrier at the surface. Under the influence of a field, these conduction electrons can be induced to tunnel through the barrier into vacuum, producing a field-induced electron emission from the metal surface. The presence of the electric field makes the width of the potential barrier finite and therefore permeable to the electrons. This can be seen in Fig. 2.13 which presents a diagram of the electron potential energy at the surface of a metal. Fowler and Nordheim further assumed that the surface barrier can be approximated with a one dimensional energy function without losing significant accuracy.

Field Emission from Metals

The dashed line in Figure 2.13 shows the shape of the barrier in the absence of an external electric field. The height of the barrier is equal to the work function of the metal, φ, which is defined as the energy required removing an electron from the Fermi level E_F of the metal to a rest position just outside the material (the vacuum level). The solid line in Figure 2.13 corresponds to the shape of the barrier in the presence of the external electric field. As can be seen, in addition to the barrier becoming triangular in shape, the height of the barrier in the presence of the electric field E is smaller, with the lowering given by[107]

$$\Delta\phi = \left(\frac{eE}{4\pi\varepsilon_0} \right)^{1/2}$$

(3)

where e is the elementary charge and ε_0 is the permittivity of vacuum.
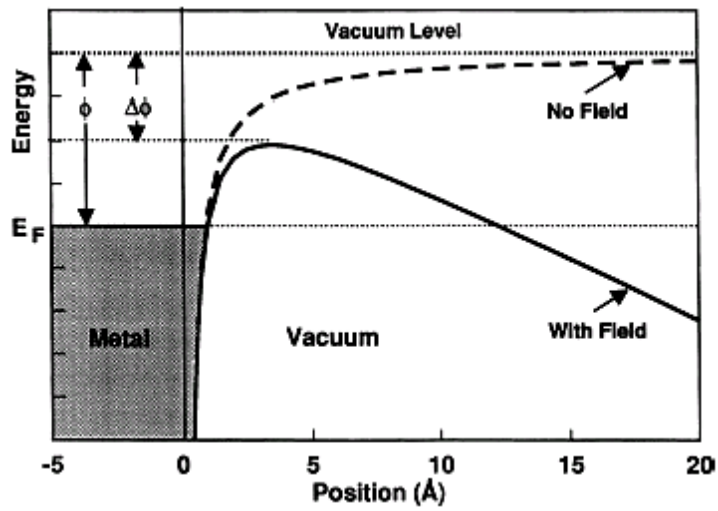
Fig. 2.13 Diagram of potential energy of electrons at the surface of a metal[108].
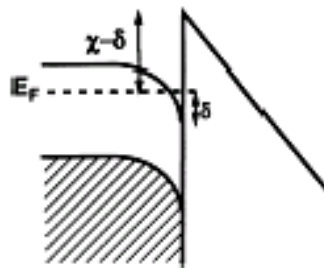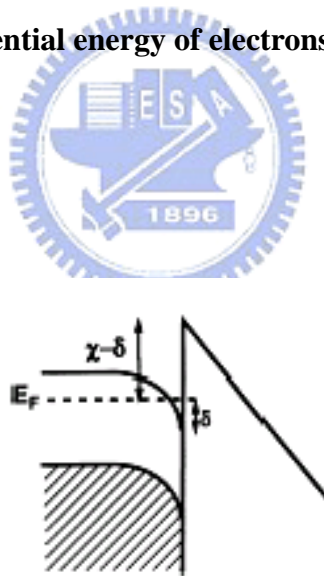
Fig. 2.14 Diagram of the potential energy of electrons at the surface of an n-type semiconductor with field penetrates into the semiconductor interior.[108]

Knowing the shape of the energy barrier, one can calculate the probability of an electron with a given energy tunneling through the barrier. Integrating the probability function multiplied by an electron supply function in the available range of electron energies leads to an expression for the tunneling current density J as a function of the external electric field E. The tunneling current density can be expressed by Eq. (4) which is often referred to as the Fowler-Nordheim equation[109]

$$J = \frac{e^3 E^2}{8\pi h \phi t^2(y)} \exp\left[\frac{-8\pi(2m)^{1/2} \phi^{3/2}}{3heE} v(y)\right] \quad (4)$$

where y=Δφ/φ with Δφ given by Eq. (3), h is the Planck's constant, m is the electron mass, and t(y) and v(y) are the Nordheim elliptic functions; to the first approximation $t^2(y)$= 1.1 and v(y) =0.95 - y^2. Substituting these approximations in Eq. (4), together with Eq. (3) for y and values for the fundamental constants, one obtains

$$J = 1.42 \times 10^{-6} \frac{E^2}{\phi} \exp\left(\frac{10.4}{\phi^{1/2}}\right) \exp\left(\frac{-6.44 \times 10^7 \phi^{3/2}}{E}\right) \quad (5)$$

where J is in units of A cm^{-2}, E is in units of V cm^{-1} and φ in units of eV. Plotting log (J/E^2) vs. 1/E results in a straight line with the slope proportional to the work function value, φ, to the 3/2 power. Eq. (5) applies strictly to temperature equal to 0°K. However, it can be shown that the error involved in the use of the equation for moderate temperatures (300°K) is negligible.[110]

Field Emission From Semiconductors

To a large degree, the theory for electron emission from semiconductors can be derived parallel to the theory for metals. However, special effects are associated with semiconductors due to the state of their surface and the fact that an external field applied to a semiconductor may penetrate to a significant distance into the interior. For the case when the external electric field penetrates into the interior of an n-type semiconductor and the surface states are neglected, log(J/E^2) is shown to be a linear function of 1/E[111]. However, in place of the work

function φ in the Fowler-Nordheim equation one needs to substitute a quantity χ-δ, where χ is the electron affinity defined as the energy required for removing an electron from the bottom of the conduction band of the semiconductor to a rest position in the vacuum, and δ denotes the band bending below the Fermi level. These parameters are illustrated in Fig. 2.14. The linear dependence of $\log(J/E^2)$ on $1/E$ is expected only if the density of the current flowing through the sample is much smaller than the current limiting density $J_{lim} = en\mu_n E/\varepsilon$, where μ_n is the electron mobility and n is the electron concentration in the bulk of the semiconductor.[112,113] At $J \approx J_{lim}$, the Fowler-Nordheim character of the relationship $J(E)$ passes into the Ohm's law (if the dependence of electron mobility on the electric field is neglected) which results in the appearance of the saturation region in the emission current vs. voltage curve.[114] Such saturation regions were observed experimentally for lightly doped n-type semiconductors and for p-type semiconductors.[115,116] Electron emission from semiconductors has been a subject of more recent theoretical considerations which takes into account complications due to electron scattering, surface state density, temperature, and tip curvature.[117-119]

Local Field Enhancement Factor

The Fowler-Nordheim equation predicts that a field of 10^7 V/cm would be necessary to generate an emission current density of $10^8 A/cm^2$ from a tungsten tip. However, experimental emission data tends to be on the order of ten to one hundred times greater than the predicted emission current density. Schottky postulated that such an enhancement factor would be due to nanostructures on the tip surface. The geometry of these nanostructures concentrates the applied field locally and so they are locations of high electron concentrations. An example of this effect is shown in Figure 2.15(a). If a voltage is applied across two parallel plates separated by vacuum the field lines will concentrate at small structures, commonly nanometer scale structures.
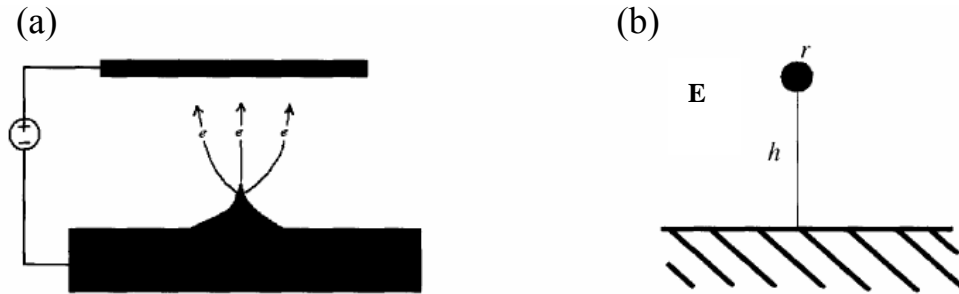
Fig. 2.15 (a) Local Field Enhancement due to nanostructure and (b) Model for local field enhancement.
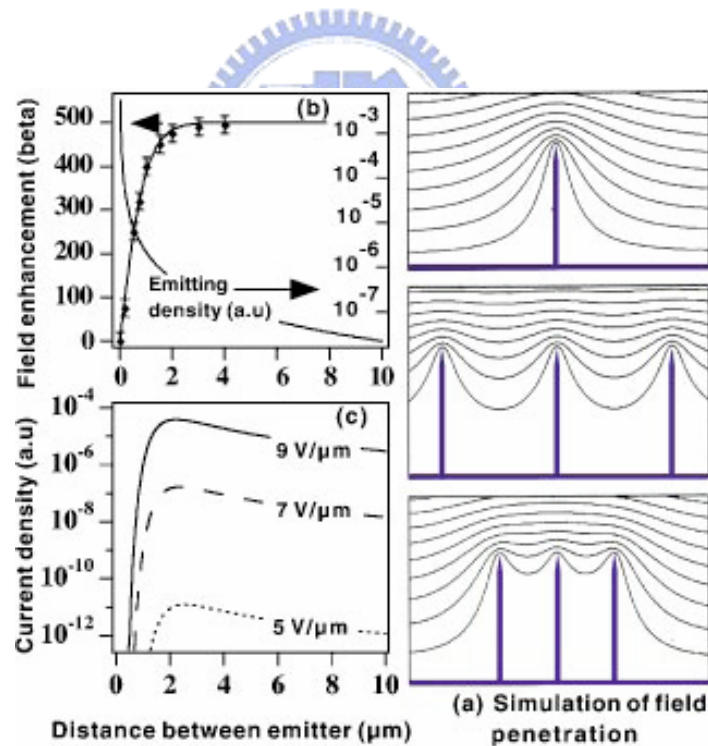
Fig. 2.16 (a)Simulation of the equipotential lines of the electrostatic field for tubes of 1 mm height and 2 nm radius, for distances between tubes of 4, 1, and 0.5 mm; along with the corresponding changes of the field enhancement factor ß and emitter density (b), and current density (c) as a function of the distance[120].

The apparent enhancement of the applied field is represented by the ß coefficient, which has been dubbed the "local field enhancement factor". The local field enhancement can be considered a product of the nanoscale protrusion from the metal surface. The local field enhancement can be similarly produced by other nanostructures. The factor is related to the tip radius, r, and the height, h, of the material and field enhancement can be expressed as (6):

$$E = \beta V \tag{6}$$

To incorporate the local field enhancement factor and the constants into the previous equations, the substitution suggested by equation (6) is made. The simplified Fowler-Nordheim equation becomes:

$$I = J \times \alpha = A \times V^2 \exp(-B/V) \tag{7}$$

where

$$A = 1.42 \times 10^{-6} \times \alpha \times \beta^2 / \phi \times \exp(10.4 / \phi^{1/2}) \tag{8}$$

$$B = 6.44 \times 10^7 \times \phi^{3/2} / \beta \tag{9}$$

Along with the I-V curve, a "Fowler-Nordheim plot" is generally shown for a material. Its linearity clearly illustrates whether or not the non-linear I-V curve can be represented by field emission. If the field emission data is properly described by the Fowler-Nordheim equation, the plot shows a straight line with a projected y-axis intercept of B and slope of A.

Screening Effect

The Fowler-Nordheim equation has predicted the field emission behavior for a film or a single emitter (which also include a single emitter in the gated device). However in normal cases, the field emission current does not achieve the predicted value since nanostructures are usually synthesized with massive amount. In fact, for high density films, screening effect reduces the field enhancement that account for the decreased emission current. For films of medium density, there is an ideal compromise between the emitter density and the inter-emitter distance, which is sufficiently large to avoid screening effects. A better control of density and morphology (and hence of the β factors) of the films is thus clearly required for future applications.

In the previous reports[120,121], a predicted inter-emitter distance of about 2 times the height of the CNTs optimizes the emitted current per unit area. Simulation of an ideal density of 2.5×10^7 emitters/cm^2, or equivalently to 625 emitters per 50x50 mm2 pixel was obtained.
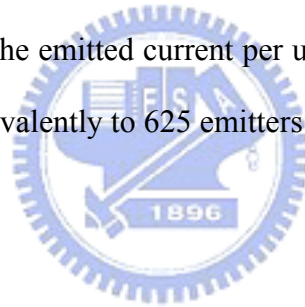
Introduction to Field Emission Device (Display)

The application of field emission is basically the electron source which may be applied into vacuum tubes, magnetrons, electron guns in TEM or SEM, cold-cathode pressure sensors and displays. Here we focus on the application of display technology which nowadays called field emission display (FED).

Fig. 2.17(a) shows the structure of one form of a FED based on emission of electrons from sharp-tipped cones. The cones are small, and each pixel contains hundreds or thousands of them. Instead of thermo-ionic emission, electrons are released in the high electric field that occurs close to the microscopic tips. The field at the tips is determined by the microscopic geometric and the difference in the voltage between the gate and cathode. After emission, the electrons are accelerated towards a phosphor coated on an optically transparent anode on the opposite substrate. The anode voltage is limited by breakdown between spacers. Since the FED needs no magnetic coils to change the trajectory of the electrons, there's no need for such a dimension like traditional CRT is. Fig. 2.17(b) demonstrates the dimension difference between a CRT and a FED.

Table 1. shows the power efficiency of the state-of-the-art display technologies which reveals the potential advantage of FED. To date, FEDs are still serious competitors to LCDs and concentrate their most important advantages, such as small thickness (less than 1cm), low power consumption (comparable and even less than LCDs), together with such important feature as high luminance efficiency (>5lm/W), high brightness (300-600cd/m^2), perfect linear grayscale, wide view angles, and CRT image quality. At the same time, FEDs have no problems with color convergence and x-rays and magnetic irradiation, which is typical for the conventional CRTs. The FEDs do not require polarizers or backlighting and cannot contain black (dead) pixels, as in the LCD case.

(a)   (b)
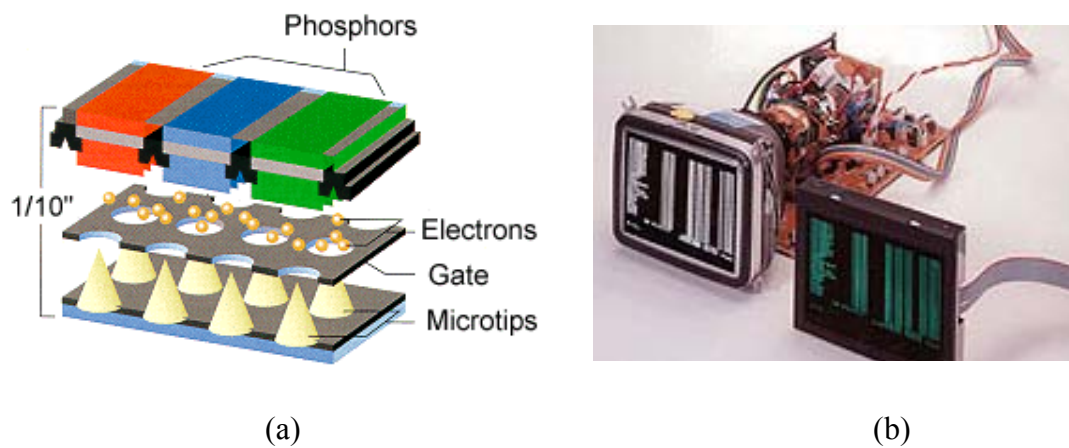
Fig. 2.17 (a) Schematic diagram of a field emission cell (b) comparison between traditional CRT (left) and FED (right) modules.
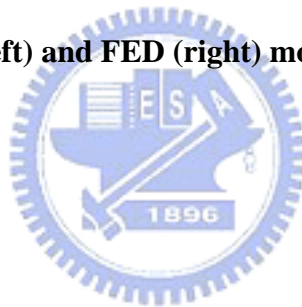
Light-generating mechanism/display technology	Luminous Efficiency(lm/W), white light
Theoretical limit	220
Photoluminescence: TL lamp	80
Cathodoluminescence at 30kV	30
CRT with 50% GT at 30kV	3
FED with 50% GT at 8kV	6-7
RPTV (CRT) at projection screen	2.3
PDP with 50% GT	0.8
LCD TV	~3
Inorganic LED	5-10
OLED/PLED	3-5
Thin-film electroluminescence	1-2

Table 1. Power efficiency of current display technologies.

Chapter 3 Experimental Details

3.1   Fabrication of Metal-Insulator-Silicon Structure

In order to achieve practical application, fabrication of the triode structure (or gated device) is a necessary step prior to the deposition of nanomaterials. Properties of high current density, controllability of emission current, can therefore be attained. Thanks to modern semiconductor technologies, fabricating the triode structure has become facile. There are several ways to fabricate a gated structure and there are vast structures with the same idea have been invented. In this thesis, we fabricate the very original circular triode structure, which was once used to fabricate a Spindt-type structure, to study its characteristics.

Figure 3.1 shows a detail flow chart for fabricating a triode structure. We design a MIS structure and fabricate it by standard semiconductor process technologies. Starting substrate is a polished n-type, (100) oriented wafer with resistivity of 4~6 Ω-cm. The selection of Pt as the electrode has several reasons. First is due to the high melting point that makes it hard to be vaporized and be more resistant to ion-bombardment in the later MPCVD process. Second, the inertia of Pt makes difficult to form compounds. Third, the most important, Pt is relatively hard for the VLS process of carbon that could disturb the selective growth of the nanomaterials. In fact, doped poly silicon has been used to fabricate the structure because of its simplicity in the process steps, but it shows poor resistance that makes it etched away. Therefore, compare with poly silicon, Pt has the fourth advantage, which is good electron conductivity. However, these advantages make the device much complex and require additional steps to fabricate, including several photolithography alignments and lift-off process since Pt is not suitable for reactive ion etching.

All processes for fabricating MIS structure here are supported by National Nano Device Lab and Nano Facility Center, NCTU. The list below shows the model for the fabrication processes.

Photolithography	G-line Stepper, ASM PAS2500/10 Stepper
Horizontal furnace and LPCVD	ASM/LB45 Furnace System
Oxide etcher	TEL, TE-5000
Sputtering system	ULVAC EBX-10C Dual E-Gun Evaporation System
Clean bench	SANTD CLARA PLASTICS Model 1100B
Vertical furnace	ASM Vertical Furnace system

Table 2 Facilities for fabricating the FED device.

1. 6" n-type (100) Si wafer

2. Deposit wet oxide (5800Å) by furnace

3. Photoresist mask by photolithograhy

4. Etch of SiO$_2$ (5800Å) by oxide etcher

5. Deposit Chromium (200Å) by E-Gun evaporator

6. Removal of photoresist by lift-off process

7. Photoresist mask by photolithography

8. Deposit Titanium (500Å) and Platinum (1500Å) by E-Gun evaporator

9. Remove photoresist by lift-off process

10. Selective growth of Carbon nanotips by BAMPCVD

Si   SiO$_2$ PR   Cr

Pt   Ti   Nanotips

Fig. 3.1 Fabrication procedure of a MIS structure.
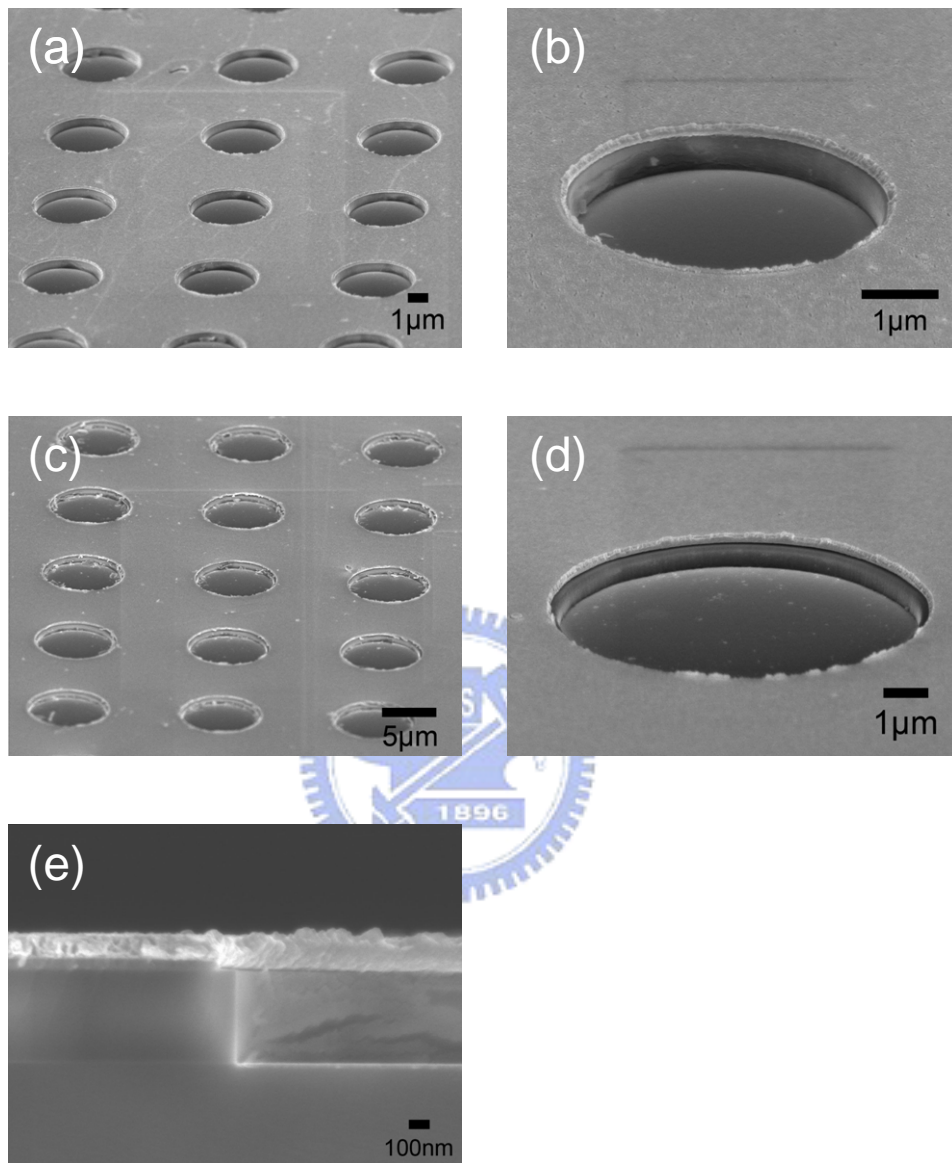
Fig. 3.2   SEM images of the triode structure (a) a 50 x 50 array (b) close-view of the array (c) cross-section view (d) an individual hole.
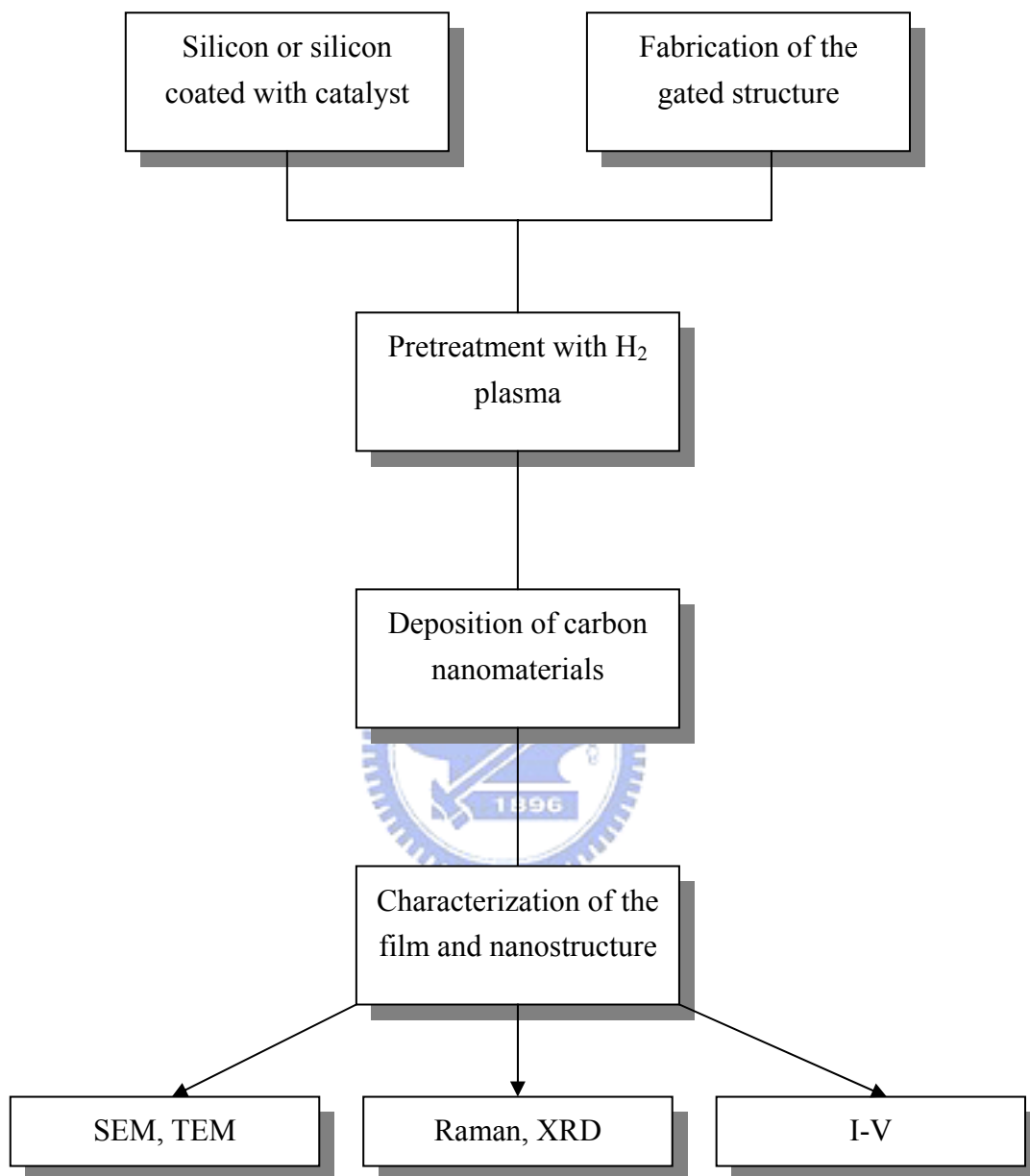
Fig. 3.3 Flow chart of experimental procedure.

3.2   Deposition of Carbon Nanomaterials by Bias-assisted Microwave Plasma Chemical Vapor Deposition

Figure 3.3 show approximately the experimental procedure. In most conditions we use two step pretreatments, which include wet cleaning and H_2 plasma treatment. The substrates are first cleaned with organic solvents and washed with de-ionized water with ultrasonic. Pure nitrogen gas is then introduced to dry the substrate before loading into the CVD chamber.

The chamber is evacuated to a pressure of $\sim 10^{-2}$ Torr with a rotary pump. To begin the H_2 pretreatment process, the reactant gas hydrogen is then introduced into the chamber at a rate of 200 sccm to a setting pressure of 15Torr. The microwave power of 400W is applied and the plasma is obtained. The plasma's horizontal position is adjusted by the plunger to fully immerse the sample in the plasma. The reflected power is minimized to < 10 W with the assistance of a three-stub tuner.

After the hydrogen plasma pretreatment, the reactive gases are introduced into the system by directly changing the mass flow meter. The reactive gases used in deposition are a mixture of CH_4 and H_2. In order to verified the new material we discovered here, several parameters are introduced which include H_2 plasma pretreatment time, methane concentration, growth time, and applied bias.

Figure 3.4 schematically depicts the layout of the Bias-assisted MPCVD system. A quartz tube is vertically attached to a rectangular waveguide used as deposition chamber. The microwave from a magnetron source (model IMG 2502-S, IDX Tokyo, Japan) is supplied to the quartz tube through an isolator, three-stub tuner, and a power meter. Then the microwave power is coupled to the quartz tube through an aluminum waveguide with a hole drilled through from top to bottom face. Aluminum tubes extend out from both holes; the tube extensions are water-cooled as well. A sliding short circuit is then attached at the end of the waveguide. The lower position of the quartz tube is connected a stainless steel multi-port chamber equipped with a rotary pump.

The substrates are positioned in the middle of the quartz tube waveguide intersection and held vertically by a substrate holder which is 20mm in diameter, made of molybdenum. Under the holder, attached a tantalum wire which is connected to the bias system; it was used as the lower electrode in the bias treatment stage. A quartz protector under the holder to protect the plasma not attracted to the tantalum wire attached to the molybdenum. The upper electrode, a molybdenum plate of 20mm in diameter which is placed 35 mm above the substrate, also attached to a tantalum wire.   The controlled amount of the source gases was introduced into the chamber by mass flow controllers (model 647B, MKS instrument, Inc., USA) from the upper end of the quartz tube. A small window was cut in the waveguide at the center of the plasma cavity, allowing direct observation of the plasma.

In this thesis, nanomaterials including CNTs and carbon nanotips are synthesized with various catalyst and growth parameters. The optimized parameters are listed in Table 3.
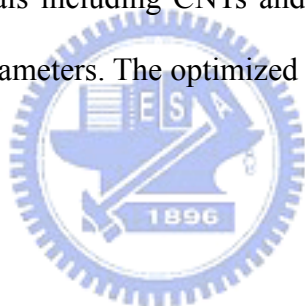
	Carbon nanotubes			Carbon nanotips	
Catalyst	Fe	Cr	Ni, Ni/Au	Cr	Catalyst free
Microwave power	400 W				
Operating Pressure	15 Torr				
H_2 treatment	15 min	30min	None (annealed)	15 min	
Gases	$H_2/CH_4=40/10$			$H_2/CH_4=30/10$	
Bias	None		150V		
Growth time	15min				30min
Substrate temperature	~700℃				

Table 3 Growth conditions for carbon nanomaterials.
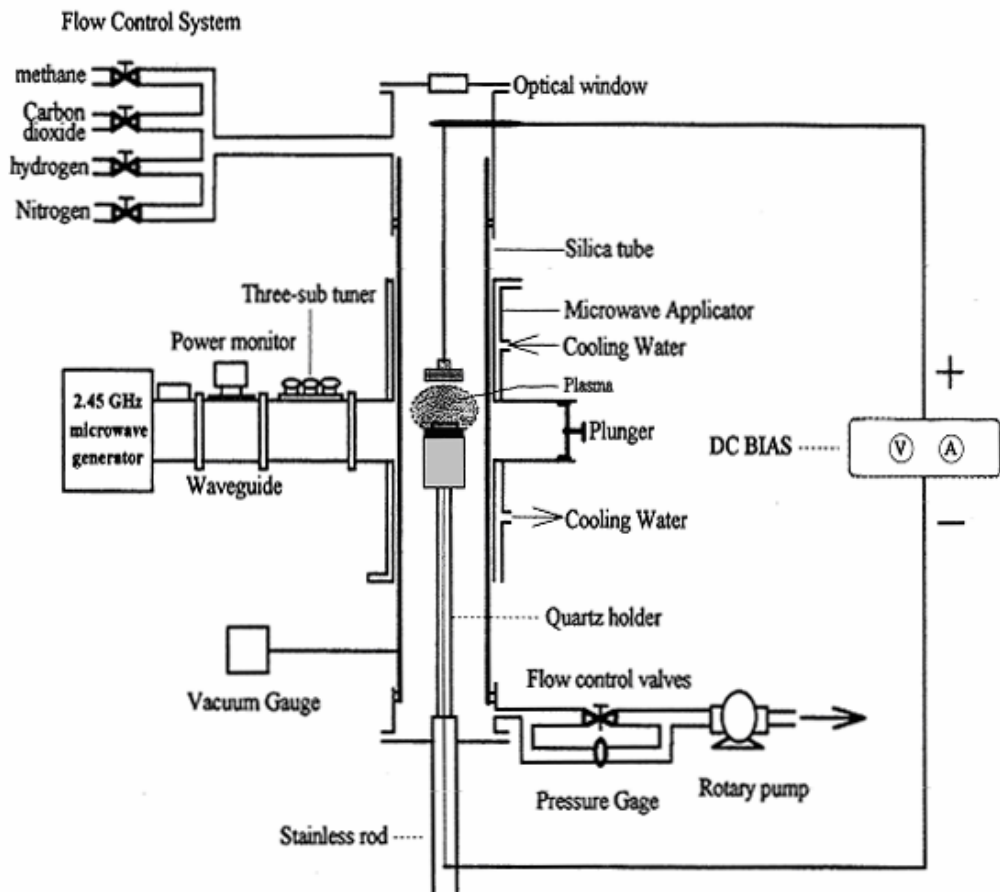
Fig. 3.4 Schematic diagram of the bias assisted microwave plasma chemical vapor deposition system.

3.3 Analysis Instruments

Scanning Electron Microscopy (SEM)

Scanning electron microscopy is used to observe the surface morphology of wide range kinds of objects. It has the advantage of rather easy sample preparation, high image resolution, large depth of field, and high magnification. A common SEM contains an electron gun to generate electron beams, which will be accelerated under 0.4-40kV voltage. By deflecting the incident beams with the focusing coils, a two dimensional image can be obtained by detect the reflected secondary electrons and the backscatter electrons.

The model we use most here is field emission type SEM JEOL-6500. Accelerating voltage is 15kV with current of 10μA. Working distance is 10mm under 9.63×10^{-5}Pa.

Transmission Electron Microscopy (TEM)

In a typical TEM a static beam of electrons at 100-400kV accelerating voltage illuminate a region of an electron transparent specimen which is immersed in the objective lens of the microscope. The transmitted and diffracted electrons are recombined by the objective lens to form a diffraction pattern in the back focal plane of that lens and a magnified image of the sample in its image plane. A number of intermediate lenses are used to project either the image or the diffraction patter onto a fluorescent screen for observation. The screen is usually lifted and the image formed on photographic film for recording purposes.

The TEM used for the study is filament type Philips Tecnai-20 equipped with CCD camera for high resolution image.

Raman Spectroscopy

While photons illuminate a molecule or a crystal, they react with the atoms accompany with momentum change or energy exchange. By collecting the scatter photons, we can obtain a sequence of spectrum, including Raman scattering (inelastic scattering) and Reyleigh scattering (elastic scattering). The photon of Raman scattering can be classified into two kinds, Stoke side which photons loss energy or the molecules gains energy, and anti-Stoke side,

which photons gains energy or molecules loss energy. Generally, Stoke side is used to characterize the material. As Raman spectrum provides information of crystallinity and bonding, it has become the most direct and convenient way to identify carbon related materials. The Raman spectrum peak of C-C and C=C bond in crystalline graphite are 1380 (D0peak) and 1580 cm^{-1}(G-peak), respectively, as shown in figure 3.5. The ratio of D-peak intensity (I_D) and G-peak intensity (I_G), I_D/I_G is commonly used for characterizing the degree of graphitization for carbon materials. In a series of test of samples, lower the ratio indicates a better graphitization.[122-124]

The instrument we use is a Renishaw Raman microscope, Model 2000, equipment settings are shown in figure 3.6. The source we use is He-Ne laser with wavelength of 632.82nm and power of 200mW. The spectral slit width is 0.4cm^{-1}.

Field Emission Measurement

A display needs ~0.1 mA/cm^2 current density assuming an anode voltage of ~2 kV. The turn-on and threshold field for 10μA/cm^2 and 10mA/cm^2, respectively have been used as the parameters to characterize various emitter.[125] Fig. 3.7 shows the setup of a field emission measurement facility. To ensure the precision of the gap between the cathode and anode, spacers which are soda-lime glasses with thickness of 150μm are directly attached onto the sample. The anode is an ITO conductive glass with thickness of ~1mm. The length of the field emission area is defined as the distance between the two spacers and the width is the width of the sample itself. High voltage source (Keithley-237) is connected to the anode and cathode by physical contact. The experiment is carried out in a vacuum chamber with pressure of 1x10^{-6}Torr.
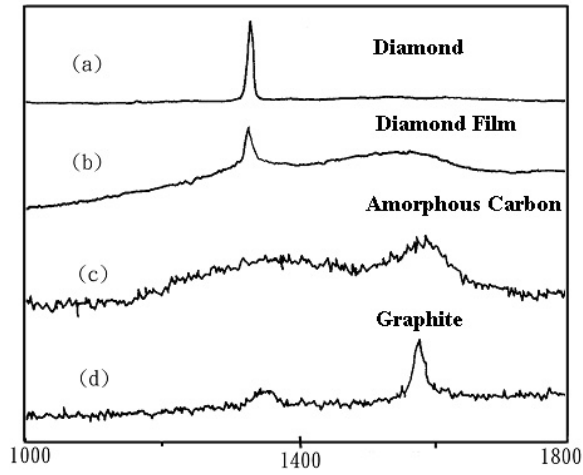
Fig. 3.5 Raman shift of (a) diamond, (b) diamond film, (c) amorphous carbon, (d) graphite.
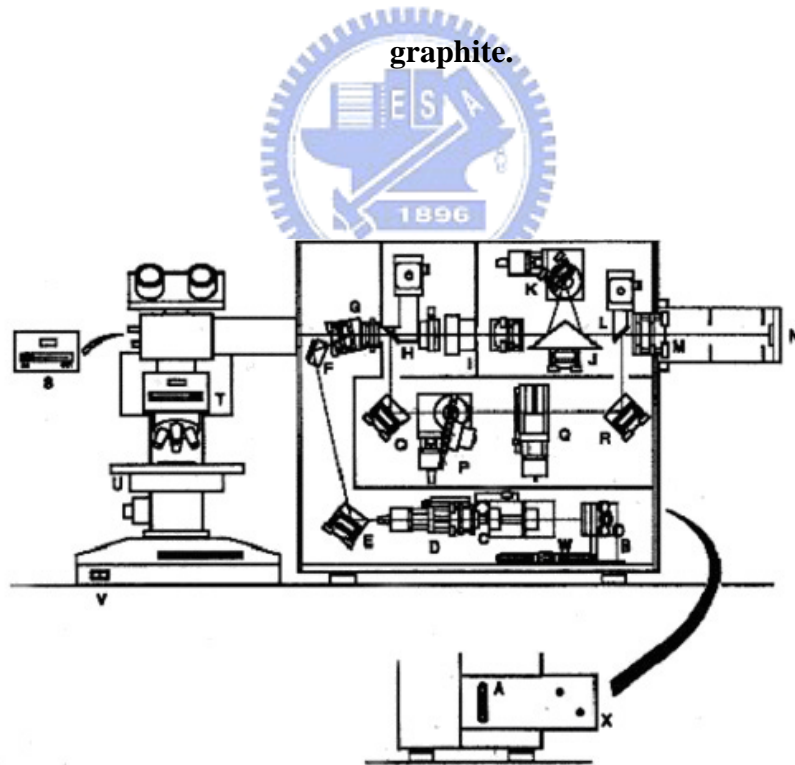
Fig. 3.6   Schematic diagram of micro-Raman equipment.

HV +

Vacuum 1x10^{-6}Torr

High voltage source
(Keithley 237)

Anode

Spacer

Cathode
(Emitter)

HV -

Field emission area
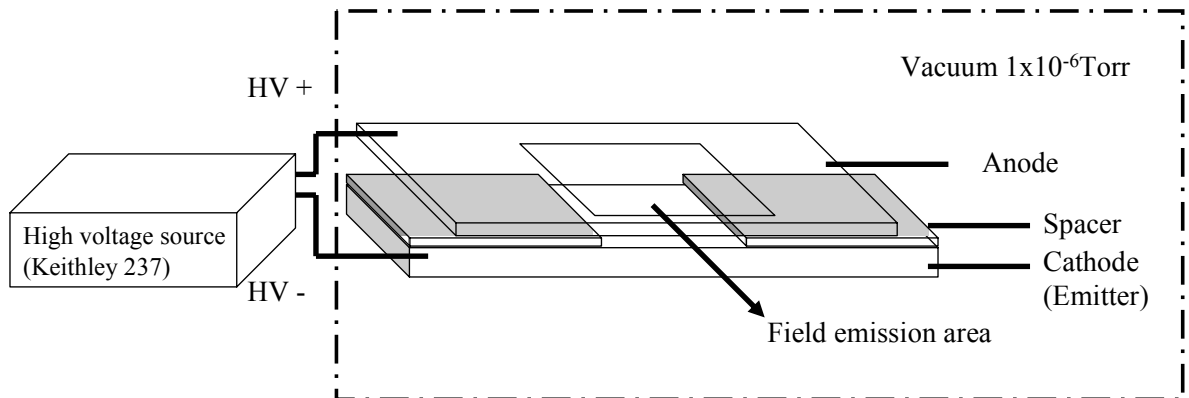
Fig. 3.7 Schematic diagram of field emission measurement setup.

Chapter 4   Results and Discussions

4.1 Carbon Nanotubes Grown by MPCVD

4.1.1 Using Fe as Catalyst to Grow CNTs

In the chapter 2, numerous reports have shown the superior field emission properties of carbon nanotubes. To achieve practical applications, high efficient synthesis and good uniformity of carbon nanotubes are the basis requirements. Reports have proposed a Vapor-liquid-solid (VLS) growth mechanism[101,102] to explain the growth behavior for the carbon nanotubes synthesis. Due to the electron configuration and solubility of carbon in metals, the transition materials, such as Fe, Co and Ni are commonly used as catalyst to grow carbon nanotubes.[126,127] In this study, the CNTs were synthesized using hydrogen and methane under 400W microwave power with no bias added.

Fig. 4.1(a) and (b) show the carbon nanotubes grow with high density with good uniformity. The average diameter and length of the CNTs is 50nm and 30μm, respectively, with growth time of 15mins. The estimated growth rate is 2μm/min. Report[128] has shown that additional DC bias could lead to a better vertical alignment of CNTs. In the study, we have only found that with bias added, the growth rate could increase obviously accompany with slightly diameter change. Here in this case, even without additional bias, the results show that the CNTs are also exhibit macroscopic vertical alignment. The reason should due to the high density of growth sites and high growth rate causing the CNTs grow upward instead of growing to other directions.

Fig. 4.2(a) shows the TEM image of a typical tubular structure of the CNT's body. Clear graphite structure of the multi-wall CNT (MWCNT) can be seen in the figure. The hollow structure which is also called a "bamboo-shape" structure appears periodically. The width and length of the cavity are approximately 10nm and 20nm, respectively. Fig. 4.2(b) shows the residue catalyst on top of a CNT. The VLS growth mechanism proposes both tip-growth and

base-growth behavior while in this study we found no base-growth CNT in the TEM analysis.

To identify the degree of graphitization, Raman spectroscopy analysis was carried out. Fig. 4.3 shows a Raman spectrum obtains from a raw sample. The D-peak (I_D) located at 1345.4cm^{-1} and G-peak (I_G) located at 1576.56 denote the disorder phase and graphite, respectively. The corresponding I_D/I_G ratio is 0.96 which shows a good graphite structure of the CNTs.

The measurement of field emission property is shown in Fig. 4.4. Fig. 4.4(a) shows the cathode-to-anode I-V measurement and the inset shows the F-N plot of the field emission behavior. The turn-on field (E), defined as the electric field required to emit a current density of 10μA/cm^2, is 1.49V/μm. Fig. 4.4(b) shows the life-time test of the CNTs with constant electric field of 5V/μm. The decreasing and zigzag curve shows an unstable field emission current under same electric field at the beginning. However, it is shown that approximately after 30 minutes of emission, the current density appears with less fluctuation. Efforts have been made to investigate "aging" of field emission on CNTs.[129,130] The proposed mechanism was due to the heat that generate during field emission by ohmic heating. The physical and chemical change, for example, the CNTs shorten and normalized their lengths and the rearrangement of carbon atoms that increases the degree of graphitization. Here we propose that the screening effect which is mentioned in chapter 2 also has great effect on the field emission efficiency. The growth of CNTs using plasma as energy source is so far unable to achieve microscopic identical length. A protrusion of the CNT may suffer a higher electric field and emit more current. The high loading of the emission current therefore leads to failure due to ohmic heating.
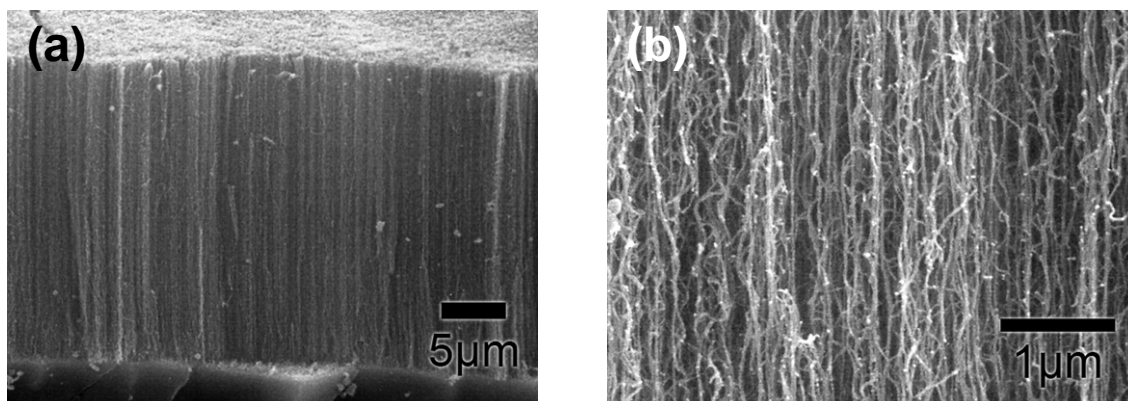
Fig. 4.1 SEM images of carbon nanotubes: (a) Cross-section view (b) Magnified view.
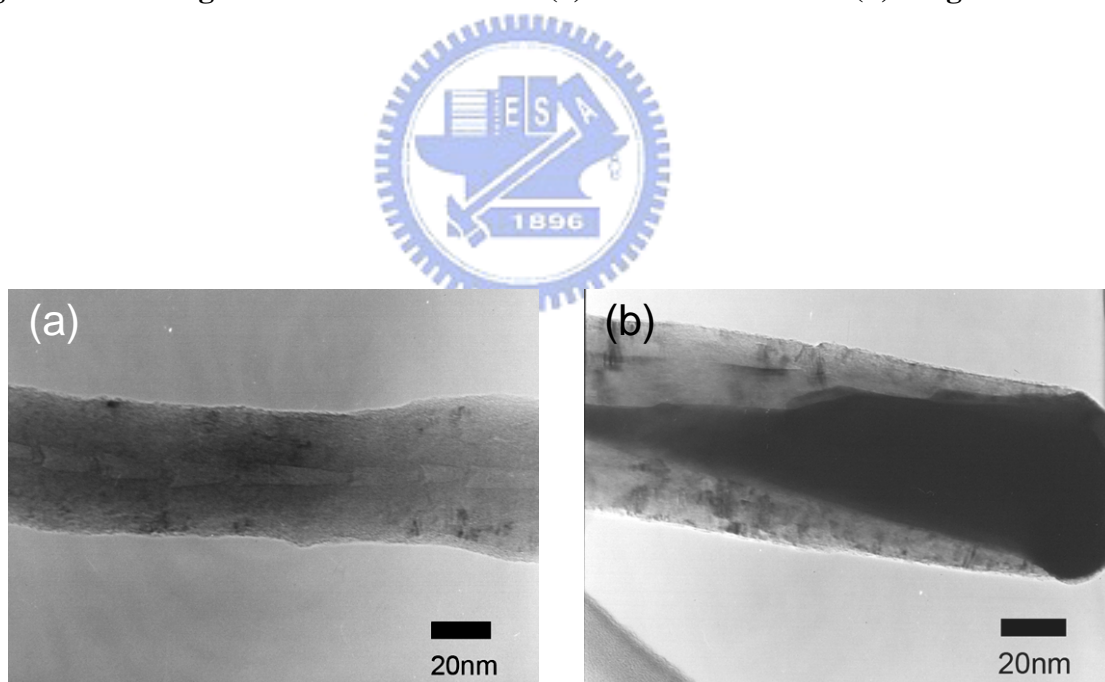
Fig. 4.2 TEM image of the carbon nanotube; (a) the fish bone body and (b) the catalyst on the tip.
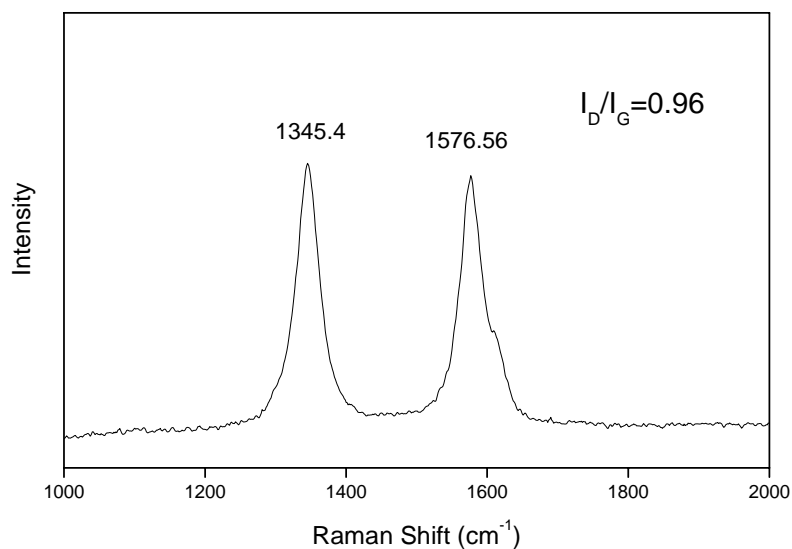
Fig. 4.3 Raman spectrum of carbon nanotubes grow at different H_2 and CH_4 flow.
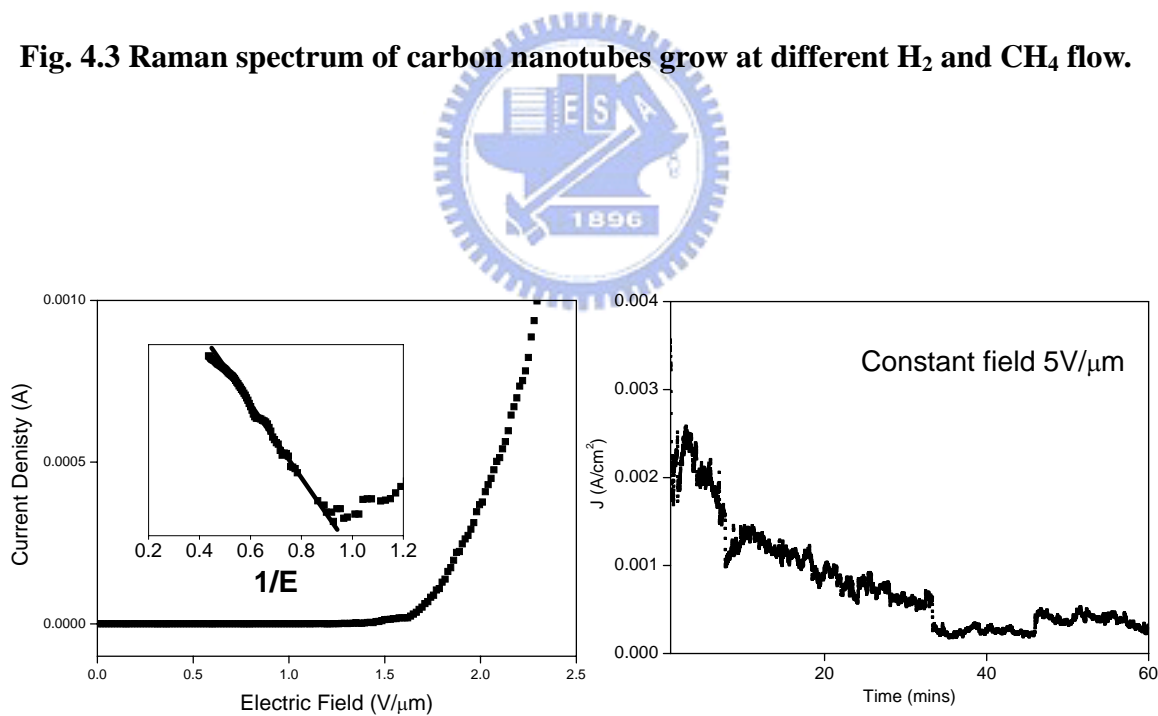
Fig. 4.4 Field emission measurement of carbon nanotubes; (a) I-V measurement and (b) life-time measurement. The inset in (a) is an F-N plot showing field emission behavior.

4.1.2 Using Cr as Catalyst to Grow CNTs

Although Fe has superior properties for synthesizing carbon nanotubes with high density and high degree of alignment, the material is not environmental friendly to the semiconductor manufacturing process. Fe has a magnetic nature which makes it easily to contaminate production facilities and also easily rusts into iron oxide that changes the surface chemistry.[131-133] In the study we show that chromium, which is commonly used as metal connect, could also be used as a catalyst for synthesizing carbon nanotubes. Chromium is not only a non-magnetic material but also tend to form a thin protective layer on the surface. However, unlike iron, chromium has a less solubility for carbon and also more tend to form chromium carbide. Therefore, it requires proper treatments to make it suitable for the carbon nanotubes growth. Currently, report on using Cr as catalyst to grow CNTs is still few.

The Cr film was prepared by sputter of 20nm and was treated with hydrogen plasma under 400W microwave power for 30min prior to the CNT growth. The growth conditions are similar to the Fe case except an additional DC bias is applied during the growth of CNTs. We have found that no CNTs will grow if there's no or sufficient bias present and only random distributed carbon particles existed. Fig. 4.5 shows the surface morphologies of different H_2 plasma treatment time. The average particle sizes are about 80nm, 60nm and 50nm correspond to Fig. 4.5(a), (b) and (c). Compare with Fig. 4.5 which shows CNTs growth with different H_2/CH_4 flow ratio, it is found that only when the catalyst particle size is below 60nm the CNTs could be formed. The long duration of the pretreatment process is necessary for the growth of CNTs with the Cr thickness; otherwise the chromium carbide capped carbon nanotips would grow, which will be discussed later.

Fig. 4.6 shows SEM images of. The results show the CNTs start to grow effectively when H_2/CH_4 reaches 30/10. Compare with the CNTs growth from Fe, CNTs grow from Cr show a much less density, smaller diameter and length. More importantly, the images show clearly tip shape structures in contrast to CNTs grow from Fe. The average diameter of the tip

is 10nm, which is much less than 50nm in the Fe case. With increasing hydrogen flow, the diameter of the tip tends to become sharper. The CNTs grow at low-yield when the H_2/CH_4 reaches 60/10 due to the high etching rate. The cross-section images are shown in Fig. 4.7. The lengths of CNTs are no more than 5μm. Compare with CNTs grow with Fe, the CNTs grow with much lower rate of 0.33μm/min.

Fig. 4.8 shows the TEM images obtain from the CNT growth under H_2/CH_4=40/10. Fig. 4.6(a) shows a tip-shape CNT with a typical tubular structure can be seen. Fig. 4.6(b) shows a catalyst on top of the CNT and a graphite structure of the CNT body. The diameter measured from the TEM image is 10nm. Fig. 4.9(a) shows the Raman analyst of the raw sample. With the increasing hydrogen content, the degree of graphitization increased, which can be seen in Fig. 4.9(b).

Results of field emission measurement are shown in Fig. 4.10. Fig. 4.10(a) shows the I-V curve of a typical field emission character. The inset in Fig. 4.10(a) shows the F-N plot from the I-V curve that indicates a field emission behavior. The measured turn-on field is 1.55V/μm, defined as the field required emitting a current density of 10μA/cm^2. The stability test is carried out and is shown in Fig. 4.10(b). Similar to the field emission stability test for the CNTs grow with Fe, the field emission stability of Cr case becomes better after 30 minutes of emission.
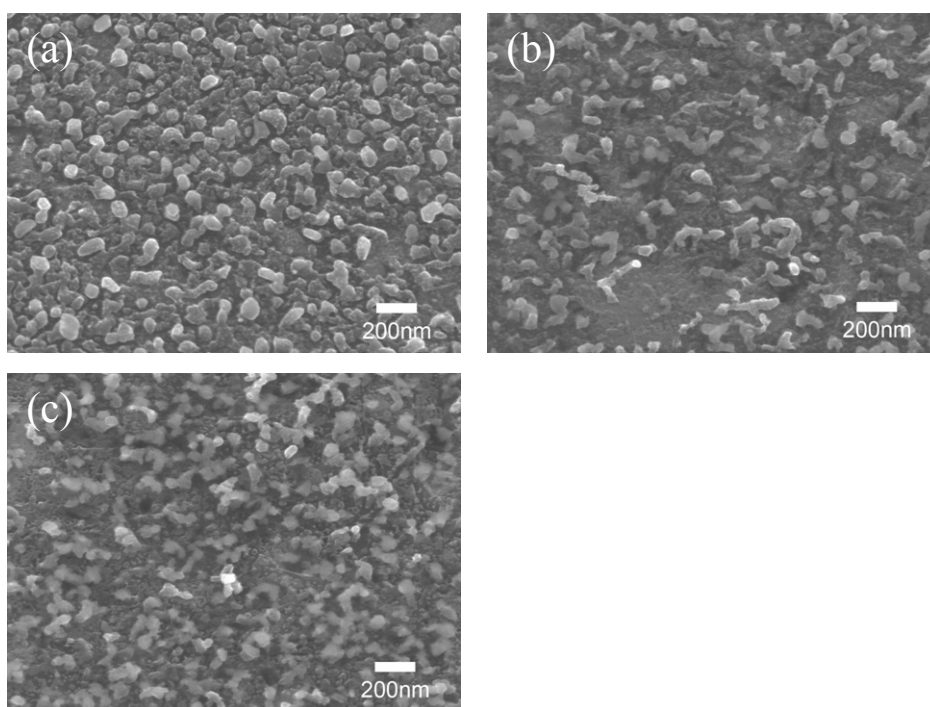
Fig. 4.5 Surface morphologies after H₂ plasma treatment for (a) 15min, (b) 30min and (c) 60min.
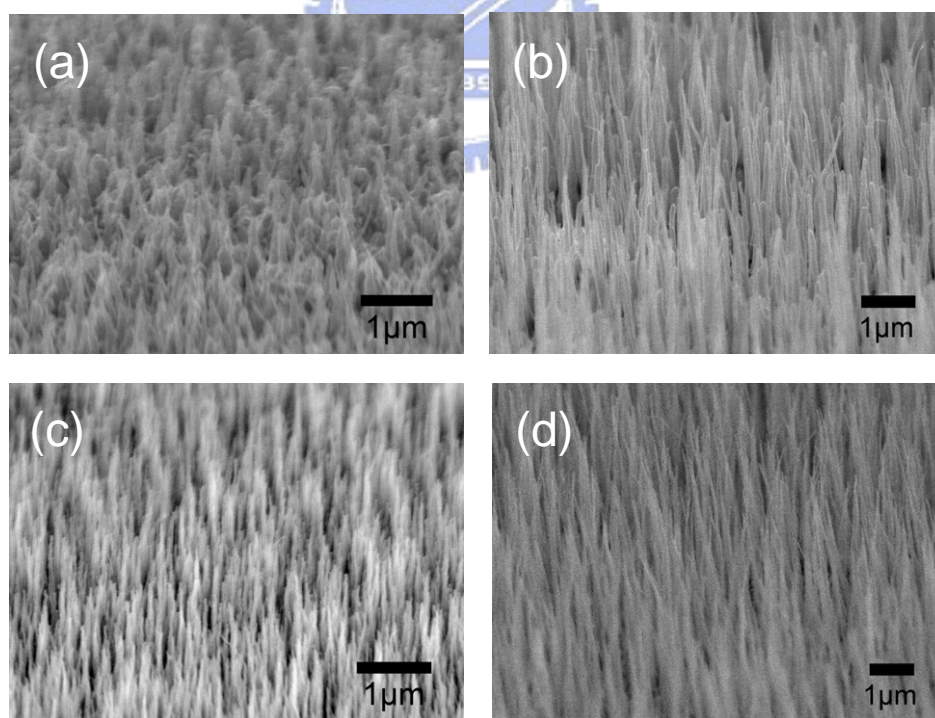
Fig. 4.6 SEM images of carbon nanotubes using Cr as catalyst with different H₂ flows; (a) H₂/CH₄=20/10, (b) H₂/CH₄=30/10, (c) H₂/CH₄=40/10, (d) H₂/CH₄=50/10.
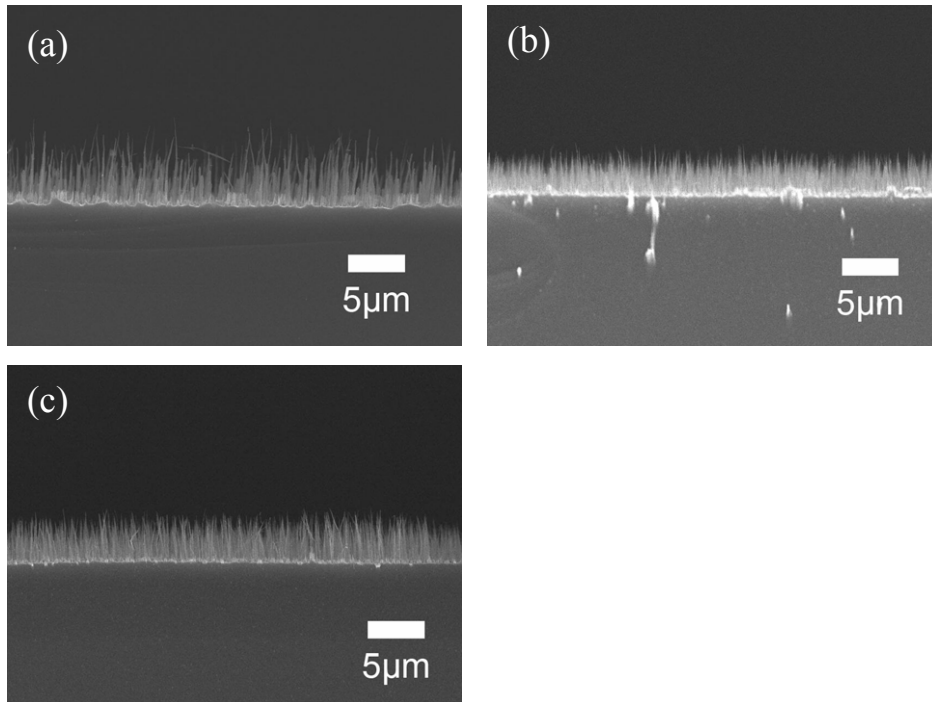
Fig. 4.7 Cross-section SEM images of CNTs grew at different H_2/CH_4 concentration. (a) H_2/CH_4=30/10, (b) H_2/CH_4=40/10, (c) H_2/CH_4=50/10.
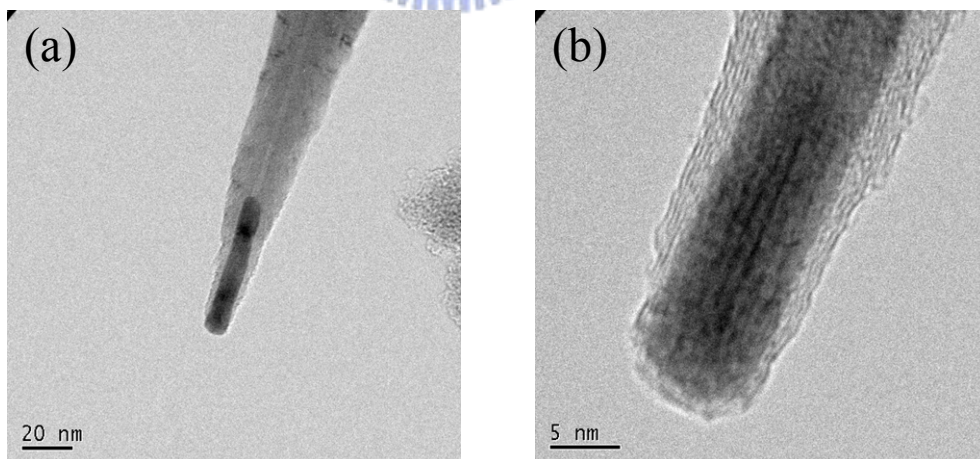
Fig. 4.8 TEM images of CNT grow with Cr. (a) The tip with catalyst on the top with tubular structure and (b) magnified view of the tip.
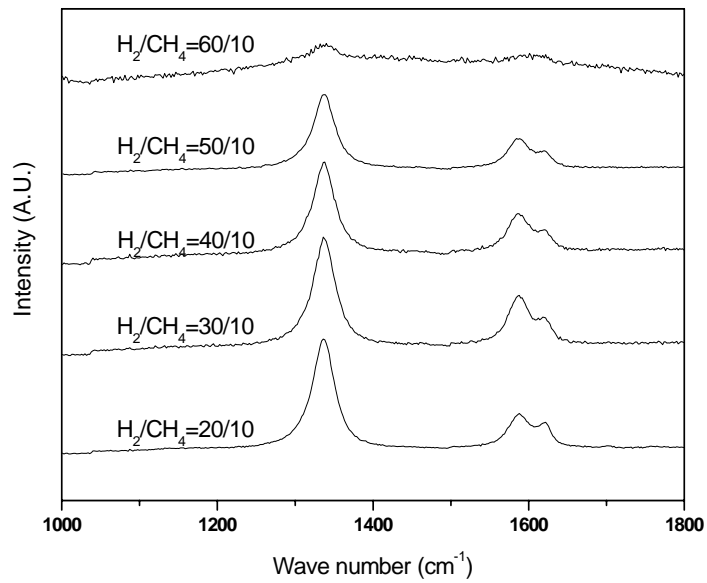
(a)
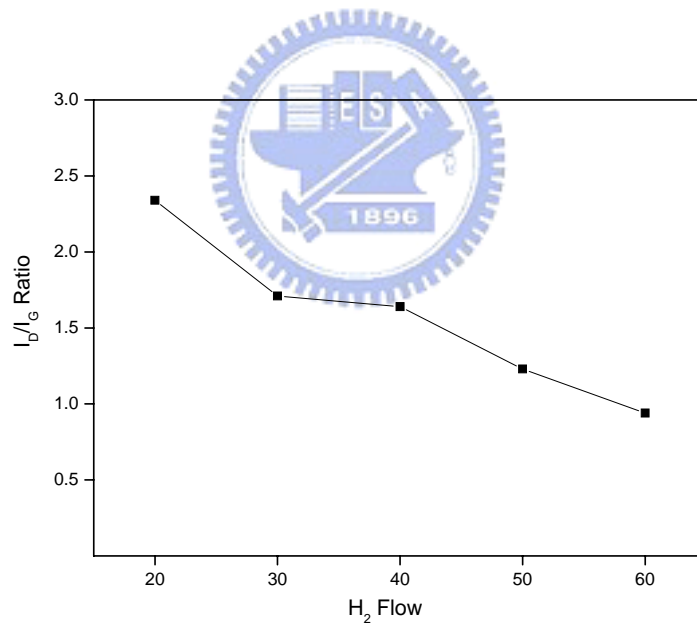
(b)

Fig. 4.9 Raman spectrum of (a) different hydrogen to methane flows and (b) correspond I_D/I_G ratio.
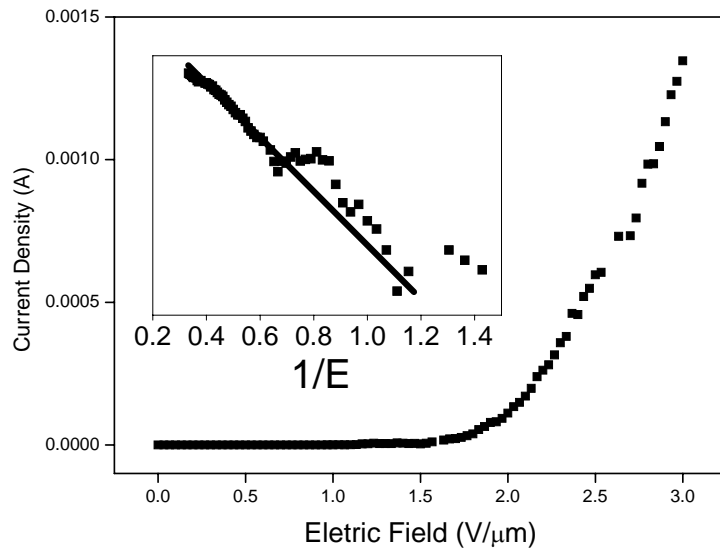
(a)
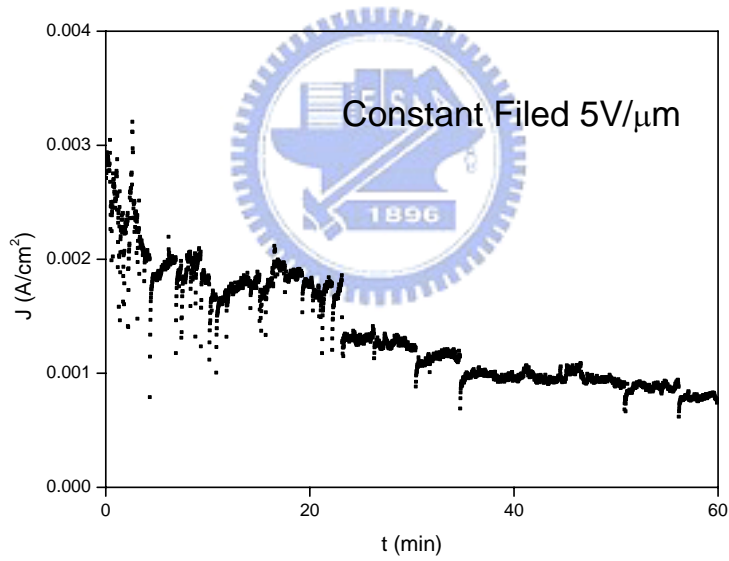
(b)

Fig. 4.10 (a) I-V measurement and (b) life-time measurement of CNTs grew by Cr. The inset in (a) is an F-N plot showing field emission behavior.

4.2 Growth of Carbon Nanotubes with Controllable Density

It has been reported that field emission from a single multi-walled CNTs reaches 10^3 A/cm^2 [136], which is an order close to the upper limit of the conduction current to 10^4A/cm^2 [137,138]. These current densities are far beyond the field emission current density for practical field emission applications.[139] Efforts have been made to improve the filed emission efficiency of CNTs, which includes purification[140] or doping,[141] but the most effective ways are decreasing the density of the CNTs.[142,143] Methods like screen printing, anodic aluminum oxide (AAO)[144] and plasma etching[145-146] were used to tune the field emission behavior while complicated procedures generates more problems. It has been reported that the density of CNTs plays a significant role in the field emission behaviors, and theoretical value of the optimal CNTs' density was calculated as 2.5×10^7 emitters/cm^2.[120] The screening effect varies with the CNTs' density drastically and the field enhancement is changed. In this study, CNTs' density can be tuned by varying the catalyst's composition or size and the density effect is confirmed experimentally.

Nickel and gold film with total thickness of 200 Å was deposited sequentially on SiO$_2$ using an e-gun evaporator. The specimen was then introduced into a programmable furnace and anneals at a temperature of 900℃ and kept for two hours under argon atmosphere and then cooled to room temperature.

4.2.1 Effects of Catalyst Treatment on Surface Morphology

After furnace annealing, it was shown in Fig.4.11 that the surface roughness increased and the catalyst film tend to form spherical particles as the composition of gold increase due to relief of surface energy. The catalyst particles gradually increased their size from flat surface to hundreds of nanometers in diameter. The increasing of the gold content lead to the decreasing of the nickel-gold alloy melting point and thus the particles size were increasing. It can be seen from the Ni-Au phase diagram that nickel and gold tend to dissolve to each easily, which means that the catalyst particle contains both nickel and gold. Although nickel and gold

completely dissolve to each other at 900℃ and spinodal decomposition area exists, insufficient cooling rate may contribute to nickel-rich and gold-rich domains exists which is the main idea of growing CNTs (the nickel –rich domain) or not (gold-rich domain).

The heat treated surface provided a template for further synthesis of different densities of CNTs. Fig. 4.12 shows the surface morphology of different CNTs density with different heat treatment conditions. The CNTs grew to about 60 nanometers in diameter and several micrometers in length. Under the same conditions for CNTs' growth, it was found that the CNTs preferred to grew around the catalyst particles as show in Fig. 4.11. It was reported[147] that the island model formatted by pre-treatment of the catalyst was favorable for continuous CNTs' film growth. The difference is that in this study, the gold or the Ni-Au solutions act as a CNTs growth inhibitor, which means the poor solvability of carbon in gold lead to a minor extrusion of carbon from the catalyst. The density therefore been reduced by the gold content which was unfavorable for CNTs growth and the increasing particle size which leads to fewer growth sites. Also, the bias in the microwave plasma chemical vapor deposition system provided a strong etching effect on the catalyst surface[148] which resisted the CNTs nucleation. However, it was found that the catalyst provided a shield of ion bombardment to the bottom of the particles near silicon surface and nickel rich domains hence initiate the vapour-liquid-solid[149] growth of the CNTs. More precise analyses still needs to be done in this complex system contain elements of silicon, oxygen, nickel and gold. The calculated CNTs densities of figure (a), (b), (c) and (d) are $2.2 \times 10^8 \text{cm}^{-2}$, $6.1 \times 10^7 \text{cm}^{-2}$, $4.7 \times 10^7 \text{cm}^{-2}$ and $3.3 \times 10^7 \text{cm}^{-2}$, respectively.

Fig. 4.13(a) and (b) shows the TEM images of the CNTs obtained in Fig. 4.12 (a) and (c), respectively. The tubular structure with the encapsulated catalyst could be verified. Fig. 4.13(a) shows the curved CNT where some curved CNTs on top of the vertical aligned CNTs could be found in Fig. 4.12(a). For the help of the EDS analysis in the TEM system, we found that the catalyst part of the CNTs contained detectable gold composition relative to the nickel. This

phenomenon suggested that the gold content of the catalyst resulted in the formation of pentagon and heptagon carbon rings, which due to different carbon solvability and lead to the winding CNTs to compensate the strain.[150] However, the EDS analysis obtained from figure 3(a) shows no detectable gold content was found in the catalyst and straight CNTs were formed by the applied negative bias voltages.[151]

4.2.2 Effect of CNTs Density on Field Emission

In order to examine the effects of CNTs' density on field emission properties, I-V measurement was utilized. Figure 4 shows the I-V curves measured with different CNTs density. The corresponding turn-on fields are 5.55V/μm, 3.55 V/μm, 2.34 V/μm and 2.78 V/μm, respectively. Apparently, field emission efficiency was enormously improved relatively to the sample which continuous CNTs film was present. By decreasing the amount of CNTs, there was improvement in the emission current. The field emission efficiency should relate to two terms, which dense CNTs will reduce the enhancement factor while too low the density will cause poor emission sites. The best density of CNTs was unable to be acquired from the plot yet which the suggested value of $2.5 \times 10^7 cm^{-2}$[120] is not attainable in this experiment.

Fowler-Nordheim[109] equations have always been used to describe the relationship between the performance, geometrical parameters and material properties for field emission cases. Under the situation of the same material is used, which means the work function is assumed to be identical, field enhancement factor or the geometrical term, β, is commonly introduced to characterized whether the performance is good or not. The larger the β is, the better the field emission properties will be. Figure 5 shows the β value versus the CNTs' density. The enhancement factor increased exponentially from 1900 to 2400 with decreasing CNTs densities of $2.2 \times 10^8 cm^{-2}$ to $3.3 \times 10^7 cm^{-2}$. It was found that the slope of the curve nearly vertical when density of CNTs approached the calculated value of $2.5 \times 10^7 cm^{-2}$ from the simulation,[120] and suggested a maxim enhancement factor can get with the density.
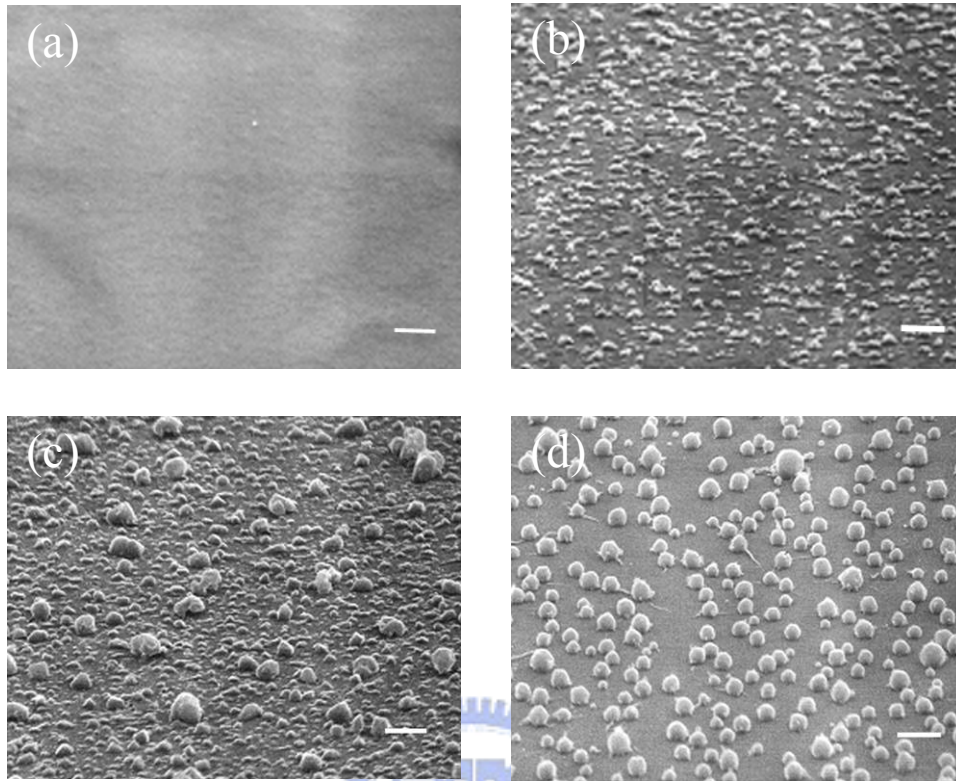
Fig. 4.11 Surface morphologies with different film composition of (a) Ni 200Å (b) Ni 150Å ,Au 50Å (c)Ni 130Å , Au 70Å (d)Ni 100Å, Au 100Å , which show different surface roughness. The scale bar in the image is 1μm.
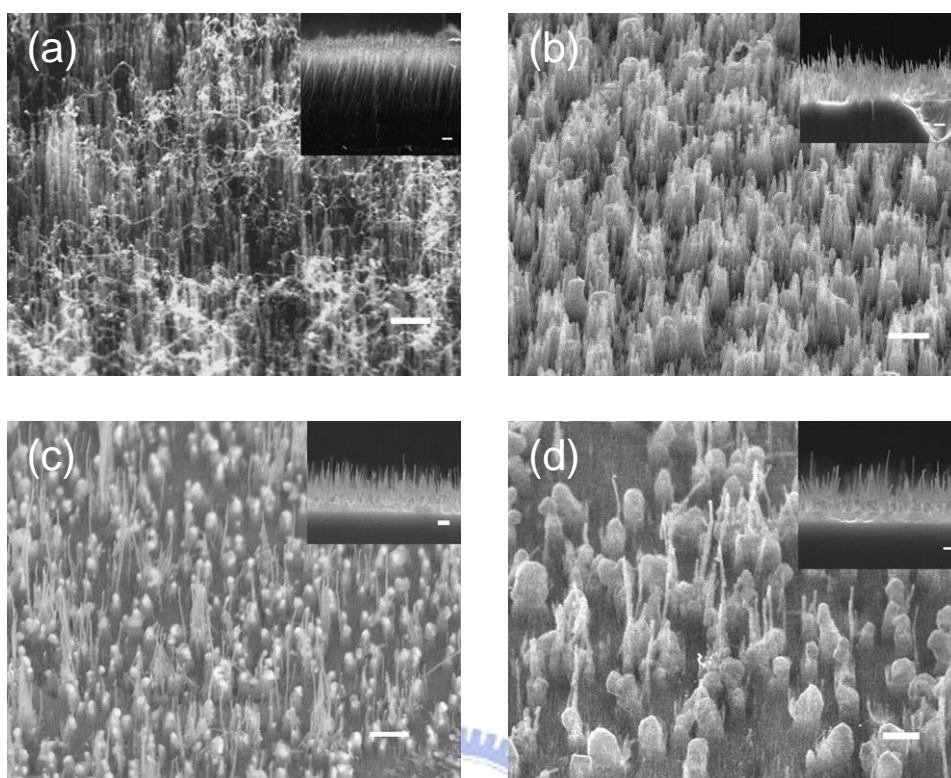
Fig. 4.12 SEM images of different density of CNTs (a) 2.2×10^8cm^{-2} (b) 6.1×10^7cm^{-2} (c) 4.7×10^7cm^{-2} (d) 3.3×10^7 cm^{-2} and the insets show the corresponding cross section images. The scale bar in the image is 1μm.
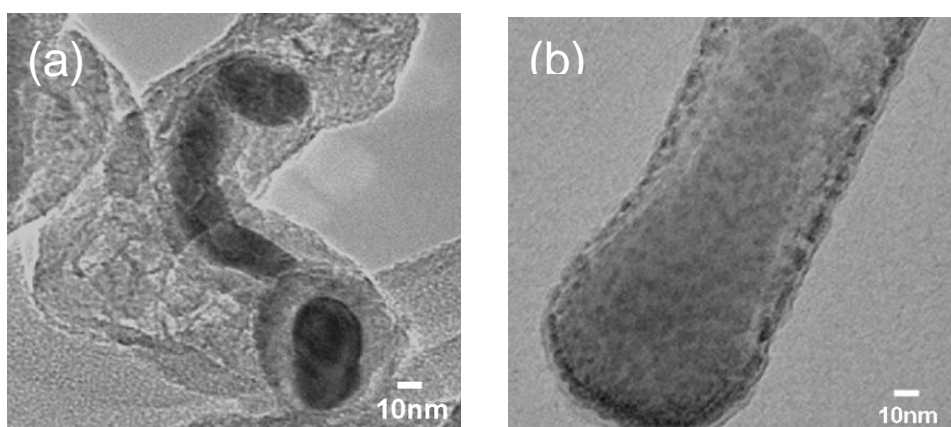
Fig. 4.13 TEM images of the CNTs showing (a) the curved CNT consist of nickel and gold, (b) straight CNT consist of nickel.
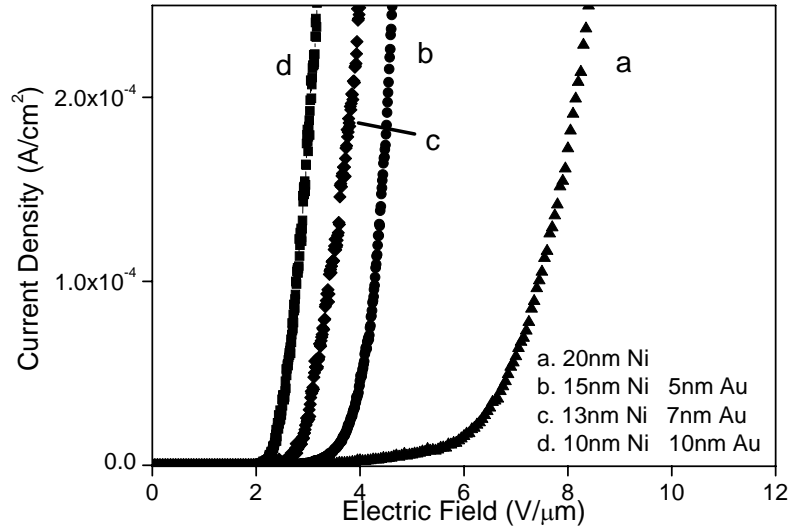
Fig.4.14 Field emission from different densities of CNTs shown in Fig. 4.12.
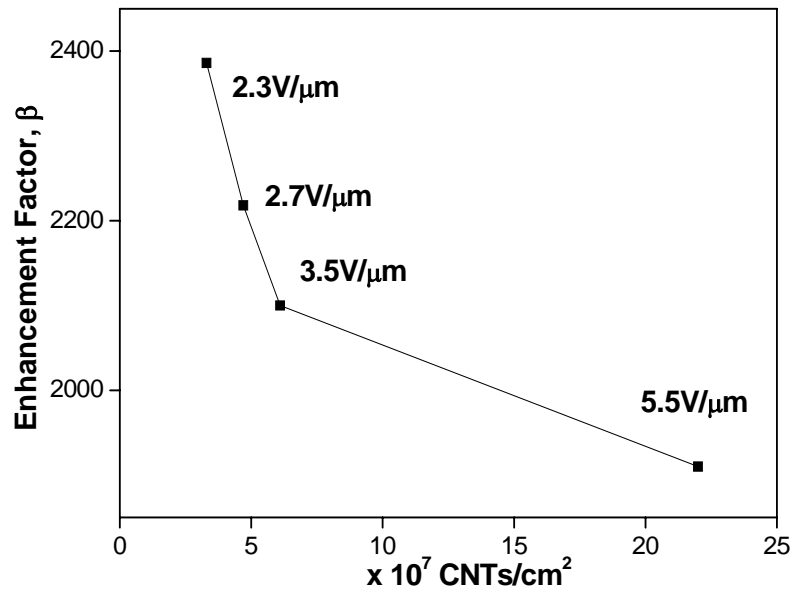
Fig. 4.15 Plot of field enhancement factors and turn-on fields versus density of CNTs.

4.3 Growth of Silicon Oxide Nanowires by Rapid Annealing Process

4.3.1 Growth and Characterization of Octopus-like Structure

In this study, SiONWs were implemented without an additional reaction gas. This process could be achieved by simply heating the catalyst coated on a silicon dioxide substrate in vacuum. Moreover, as several factors are considered in this process, specific catalyst amount, composition and cooling rate play key roles in the growth of aligned SiONWs. Compared with general vapor-liquid-solid (VLS) growth,[152] a similar solid-liquid-solid (SLS) process[153] is a SiONW growth model representative.

Our experiment began with an n-type (100) silicon wafer cleaned with a standard RCA process. Wet oxidation was then carried out in order to form a silicon dioxide film layer with a thickness of 500 nm. Nickel and gold films with different film thicknesses were then deposited on the substrate by PVD. The sequence of nickel and gold deposited on the silicon dioxide film did not show an observable difference in the experiment. The coated substrate was placed on an alumina crucible and then in a quartz tube furnace. The furnace was evacuated to 10^{-2}Torr and then purged with argon to ambient pressure with a flow rate of 500cm^3/min. The system was heated and held at 1000℃ for 2 h. After the isothermal process, the furnace was then cooled to room temperature with the same argon flow rate. During the heat treatment, the temperature was measured using a thermal couple, which was inserted into the quartz tube and was about 1cm above the sample. The cooling rate was manipulated by the stressed air flow between the quartz tube and a heater.

To investigate the effect of the catalyst composition, the specimens were deposited on 20nm multilayer with different nickel and gold thickness ratios on Si substrates. A cooling rate of about 2℃/s was obtained at the initial cooling stage. A surface morphology containing two structures is shown in Fig. 4.16. In Fig. 4.16(a), only randomly distributed SiONWs are found. These nanowires appeared to have diameters ranging from 20 to 60nm and lengths larger than 10μm. With increasing nickel amount, particles appeared at the ends of

the SiONWs and their diameters increased [Figs. 4.16(b) - 1(d)]. In contrast, the lengths of the SiONWs decreased from (a) to (d) with gold amount though the yields of the nanowires stretching from the matrix increased. In Fig. 4.16(b), only few SiONWs support the particles. The rising particles interfering with the electron beam of SEM caused the distortion of the image .The SiONWs started to grow upward from Fig. 4.16(c). In Fig. 4.16(d), the substrate is shown and only the monolayer of the structure is present. The lengths of the nanowires increased from the matrix drop from tens of microns to less than 2 um. The phenomenon suggests that the different growth behavior is due to the film composition that varies with the melting temperature of the catalyst particle. Paulose et al.[153] have reported the growth of nanowires with only a gold film. Their results showed a randomly distributed morphology similar to that shown in Fig. 4.16(a). In this study, nickel played an opposite role, which is slowing down the precipitation process, and SiONWs could hardly be found when only nickel was present. By adjusting the gold/nickel ratio, the yields of the SiONWs could be controlled. Fig 4.17 shows the trend toward the yield (length) of the SiONWs and the diameter of the particle. With the increasing gold content, the yield of the SiONWs increase and the diameter of the particle decrease. As only Au presents, the particle disappears. In addition, unlike the reported cumulate structure by Pan et al.[154,155] only the monolayer of the octopus-like structure was present since the growth originated from the local catalyst/silicon oxide film.

In this study, we found that the nanostructures could be formed only with a very high cooling rate and temperatures higher than 1000℃; otherwise, only particles with micron sizes were found [Fig. 4.18]. Annealing with a temperature of 900℃ was also carried out; however, it did not show a similar morphology. Therefore, only the initial cooling rate was considered since a very low temperature would not affect the growth. Although the temperature measurement may not be precise, a cooling rate higher than 100℃/min was estimated. Because no additional gases were used, we also inferred that the growth of the nanostructures occurs during cooling and is completed within only 1 or 2 min. During cooling, the liquid

solution containing gold, nickel and silicon oxide underwent super-saturation and the tremendous driving force made the silicon oxide to precipitate rapidly. The head part of the structure was gradually lifted off until the temperature was not sufficient for diffusion. Here, we propose a growth mechanism of the rapid cooling head-growth solid-liquid-solid process. This mechanism is different from a conventional SLS growth model, in which only base growth occurs and the continuous supply of materials from the substrate contributes to steady growth[156]. In this study, the total amount of materials for the growth of SiONWs was determined in a constant-temperature alloying process and the growth started and stopped during cooling. Further analysis also showed that the catalyst is on top of the SiONWs and suggested a tip (head) growth procedure.

Figure 4.19(a) shows the SEM image of the sample prepared with 8nm gold and 15nm nickel. The surface morphology clearly shows a less dense octopus-like structure. The diameters of the nanowires growing from the spherical particles ranged from 10 to 100 nm and appeared as empty lantern frames. The head parts of the octopus-like structures may be about 1μm high from the substrate and the sizes of the heads were about hundreds of nanometers. Due to the high cooling rate, a ball structure appeared with a rough surface. The microstructures were confirmed by TEM observation, as shown in Fig. 4.19(b). The inset in Fig. 4.19(b) shows the high-resolution TEM image of the SiONW, in which an amorphous structure can be observed. The spherical ball had been identified to consist of silicon, oxygen, nickel and gold by energy dispersion X-ray (EDX) analysis in TEM. The gold content could only be found in the EDX measurement with a low intensity but could hardly be found in the diffraction pattern in TEM. This result shows that gold and nickel could dissolve a large amount of silicon oxide at a high temperature and precipitate during cooling. Fig. 4.19 (c) shows the elemental analysis of the octopus-like structure obtained by surface Auger microscopy (SAM) in order to understand the composition and bonding structure. The detection points P1, P2 and P3 represent the spherical particle, nanowires and substrate,

respectively. The results showed that gold and nickel could only be found in the spherical particle. The silicon peaks of the three points in the diagram showed identical distributions and the relative intensities of minor peaks indicate oxygen bonding according to the database.

4.3.2 Growth of Aligned Silicon Oxide Nanowires

To achieve practical applications or further scientific research studies, a uniform surface structure is necessary. Under critical conditions in which the gold/nickel ratio, total metal amount and cooling rate were moderate, the catalyst/silicon oxide ball was completely consumed by precipitation and transformed into SiONWs. Fig. 4.20 shows the images of the samples prepared with the nickel and gold film thicknesses of 15 and 8 nm and the cooling rate of about $1.8°C/s$ which is lower than that in the case of Fig. 4.16. Figure 4.20 (a) shows the planar view of the SEM image at a defective area and the inset shows the cross-sectional view of the substrate of the aligned SiONWs. The image shows a surface similar to carbon nanotubes. The average diameter and length of the nanowires were about 50 nm and 3 μm, respectively. The SiONWs grew upward with a small curvature caused by the argon flow during cooling and without a zigzag structure. Fig. 4.20(b) shows the TEM image of a single SiONW. The diffraction pattern on the upper left shows a diffused ring, which is responsible for the amorphous structure obtained from the nanowires' body. The diffraction pattern obtained from the dark area shows a crystalline structure, which is shown on the lower right. According to the phase diagram of nickel and gold, the two metals mix completely at any composition to form a solid solution, which is an fcc structure. During the examination, it was found that all the ends of the aligned SiONWs have catalysts and none was found on the substrate. It is worth mentioning that due to the high growth rate, other interesting structures could also be found but with few amounts. For example, some comb like structures with all branches having catalyst particles were found near the substrate; we believed that the growth of these structures is due to the residue of the catalyst on the side wall of the main body and

this is also an evidence of the SLS process [Fig. 4.21(a), (b)]. The unbundled and high surface area of the aligned SiONWs may be suitable for some applications. In contrast to carbon nanotubes, the silicon oxide surface is easily functionalized by chemical treatment. Such advantages make it possible to realize surface-enhanced Raman spectroscopy (SERS)[157] and molecular sensing[158,159], or other applications that require surface treatment for further use.
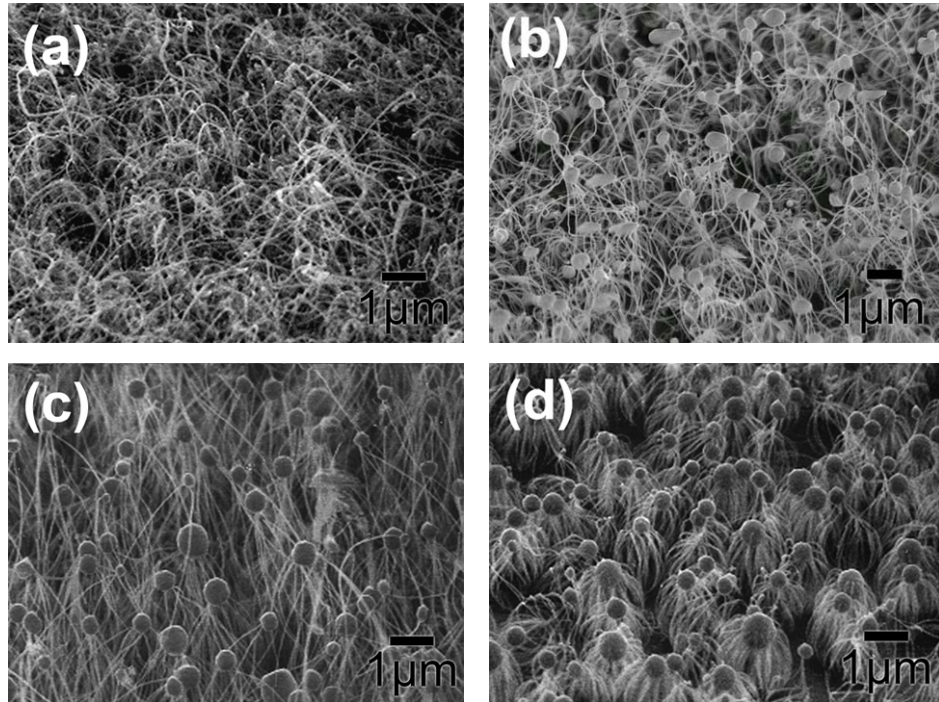
Fig. 4.16 SEM images of nanostructures with different catalyst amounts and compositions. (a)20 nm gold, (b)15 nm gold with 5 nm nickel, (c) 10 nm gold with 10 nm nickel and (d) 5 nm gold with 15 nm nickel.
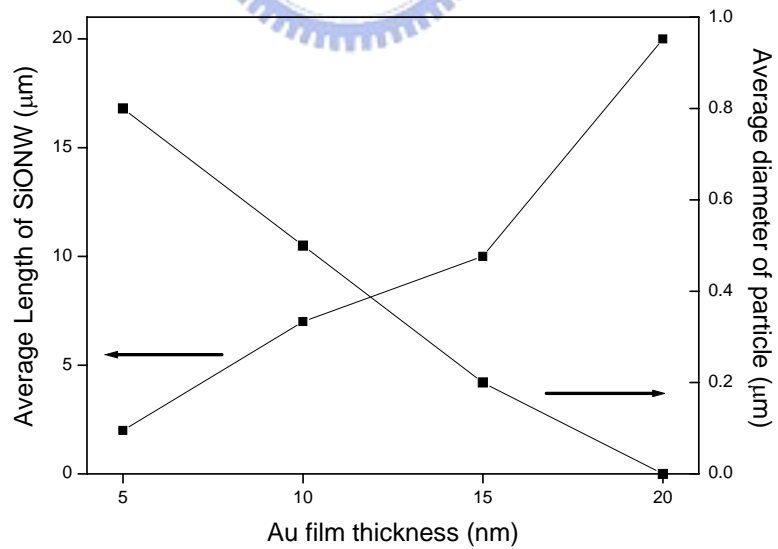
Fig. 4.17 Dimension change of the nanostructure shown in Fig 4.16
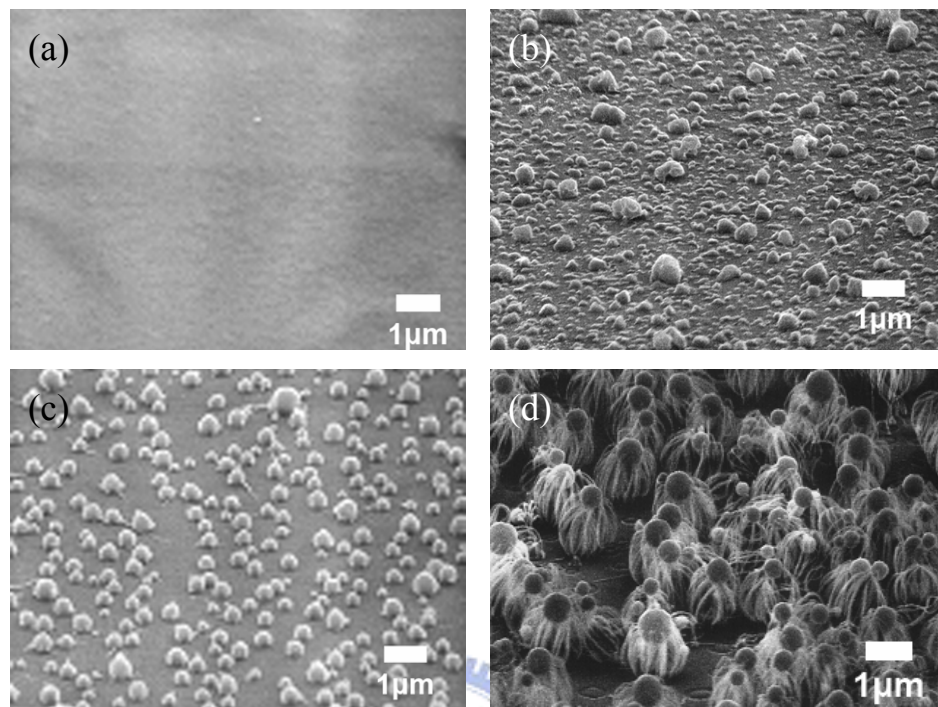
Fig. 4.18 Effects of annealing temperature on surface morphologies. (a) as deposit film, (b) annealed at 800℃, (c) annealed at 900℃ and (d) annealed at 1000℃.
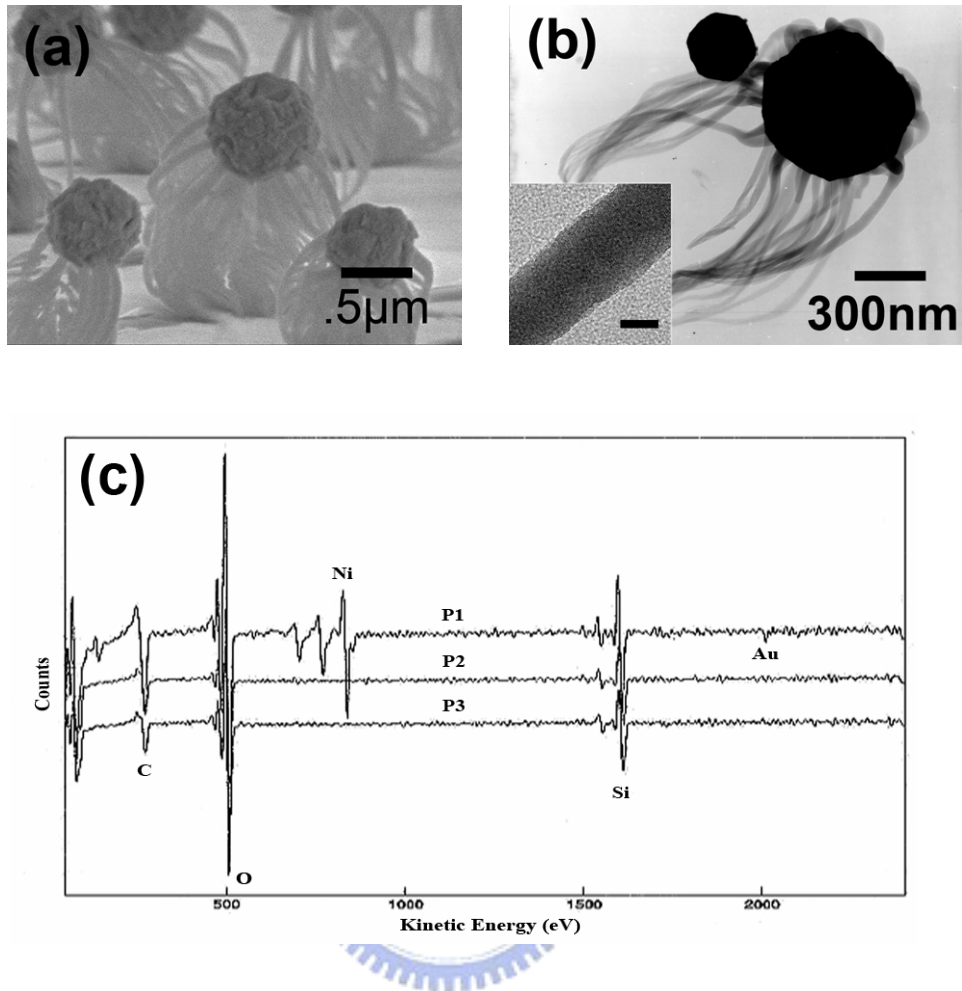
Fig. 4.19 (a) SEM images of octopus-like structures with gold and nickel film thicknesses of 5 and 18nm. (b) TEM image of an octopus-like structure. The inset shows the high-resolution image of the SiONW. The scale bar in the inset represents 20 nm. (c) Elemental analysis of structure by SAM. P1 denotes the catalyst particle, P2 denotes the nanowires and P3 denotes the substrate, respectively.
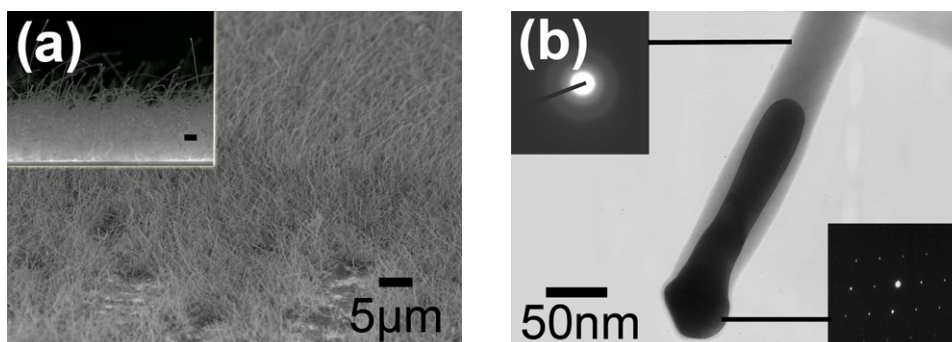
Fig. 4.20 (a) SEM image of aligned SiONWs. The inset shows the cross-sectional image and the scale bar also represents 5 um. (b) TEM image of aligned SiONW. The insets show the diffraction patterns of the silicon oxide body and catalyst.
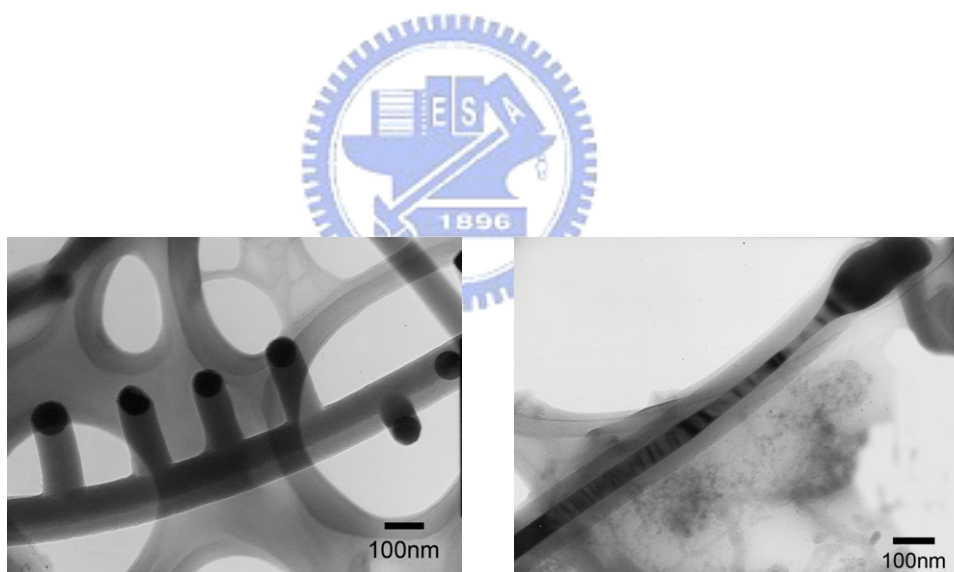
Fig. 4.21 (a) A comb-like SiONW structure and (b) SiONW fill with catalyst inside.

4.3.3 Proposed Growth Mechanism and Kinetics

To explain the growth of the nanostructure, we use the classic phase transformation kinetics to deduce the mechanism because of the similarity of the rapid cooling process. In general metal alloys, cellular and dendritic solidifications are commonly found in rapid solidification[160]. The structure appears with elongated cells that are perpendicular to the mold, or more importantly, in the direction opposite to the heat flow. The cell structure starts with a small undercooling area which in this case is the tip of the nanowire. The solute from the solidifying liquid was rejected and pile up at the root of the protrusion. With the same temperature, the increasing liquid concentration increases the melting point and the liquid phase ahead of the tip front therefore becomes "constitutional supercooling", which is crucial to the formation. Finally the tips develop into long cells growing parallel to the direction of heat flow. The supercooling tip front thus continues to grow steadily until the temperature is not sufficient for the growth and the remaining areas are solidified. The surroundings of the cells solidified at the lowest temperature and the tips (cell) growing into the hottest liquid contain the least solute. Figure 4.22 shows the nucleation and initial growth processes of the structure. In this study, by examining the content of the structure, the solutes (gold and nickel) were hardly found in the SiONWs (solvent) but exit in the head catalyst. This behavior suggests that a strong supercooling occurs and that a cell structure is formed. At stage A in Fig. 4.22, the structure starts with nucleation on the interface of the liquid phase and substrate due to heat removal. Nuclei start to grow upward owing to constitution supercooling and the elongated cell structure becomes SiONWs (stage B). In this case, the solutes (nickel and gold) are released back to the matrix. The liquid ball is then gradually lifted off during the growth of the nanowires and holds its shape by surface tension. At the final stage C, the liquid phase is solidified and the SiONWs are bended owing to the weight of the micro size ball.

Fig. 4.23 shows the schematic diagram of the growth process of the SiONWs. The growth starts with a silicon oxide substrate coated with nickel and gold (a). The next step is

annealing and a micro size particle consisting of nickel, gold and silicon oxide is formed (b). During the rapid cooling process, silicon oxide precipitates from the particle to form the silicon oxide nanowires and lift the matrix up (c). The resulting SiONW length and residue catalyst particle size depend on the catalyst composition, which is also the corresponding melting point. If the conditions are adequate, the particle is completely consumed by precipitation and only SiONWs form (d).
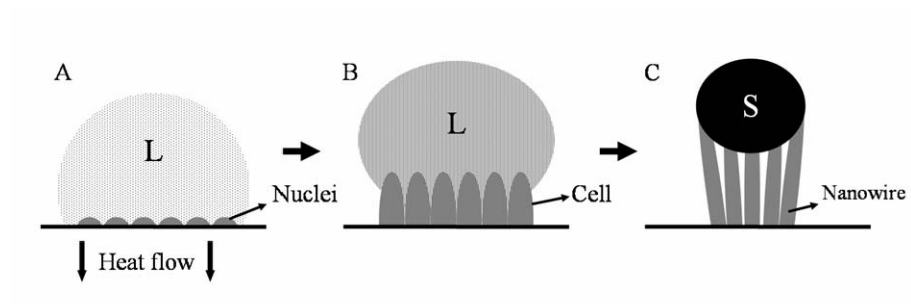
Fig. 4.22 Schematic representation of cellular growth stages induced by constitutional supercooling during rapid solidification.
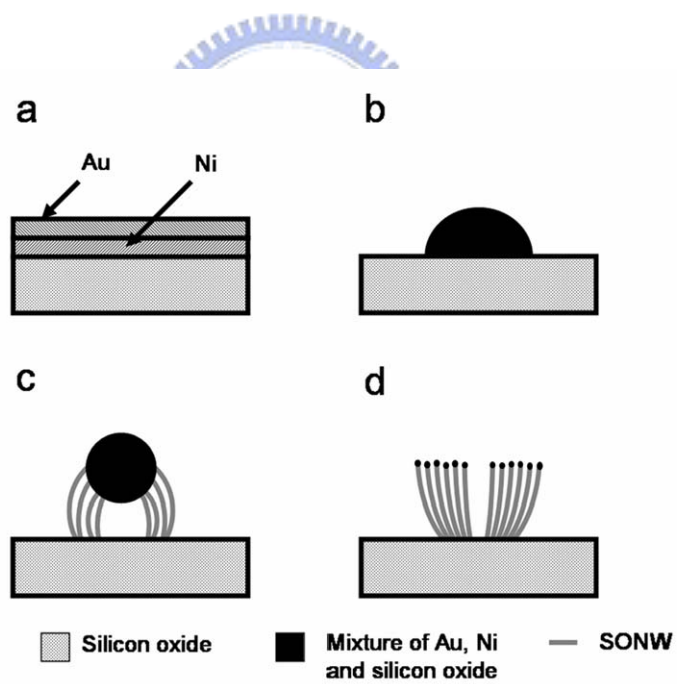
Fig. 4.23 Schematic diagram of growth processes of octopus-like and aligned SiONW structures.

4.4 Growth of Chromium Carbide Capped Carbon Nanotips Using Cr as Catalyst

4.4.1 Characterization of Chromium Carbide Capped Carbon Nanotips

In field emission theory, field enhancement factor, ß, is a term that further improved the field emission efficiency by geometric appearance. For a material that used as an emitter, ß would be larger when the emitter stands vertical from the substrate or parallel to the electric field because of the higher aspect ratio and smaller tip radius. Approaches have been made to aligned carbon nanotubes.[161-163] In particular we have recently synthesized a new material[164] using bias-assisted microwave plasma chemical vapor deposition, which grow perpendicular to the substrate with amazing uniformity.

Fig. 4.24(a) shows the surface morphology of chromium carbide capped carbon nanotips from the edge part of silicon substrate. The specimen was grown with a bias of 150V for 30min and the $H_2/CH_4=30/10$. The image demonstrates the great uniformity and the selective growth of the nanotips, which are important issues in field emission applications. Fig. 4.24(b) shows the magnified view of the nanotips. It has to be noticed that there are white spots on top of the nanotips for each one and the tip-like structure with their root connect to each other. The average size of the nanoparticle on the tip is 50nm with its neck, the as-grown carbon nanotip of 40nm and increasing it's diameter to the root part.

Fig. 4.25(a) shows the cross-section TEM image of the chromium carbide capped carbon nanotip. It is also found that the dark spots exit only on top of the nanotips without any residual at the bottom, this is quite distinct from carbon nanotubes where tip growth model and base growth model co-exist.[165] Analysis from diffraction pattern shows that the specific composition of the crystalline structure to be Cr_7C_3.[164] Fig. 4.25(b) shows individual crystalline chromium carbide embedded on a carbon nanotip with lots of defects such as twins or stacking faults. The phenomenon is believed due to the low temperature process and rapid formation of chromium carbide relative to the typical high temperature and log time for hard

coatings of Cr_7C_3.[166] In fact, in the XRD analysis, several minor peaks indicate other carbides which include Cr_3C_2 and $Cr_{23}C_6$. Report[167] has shown that chromium forms three stable carbides, Cr_3C_2, $Cr_{23}C_6$ and Cr_7C_3. Below 1000℃ no significant homogeneity has been detected for either the three carbides. This indicates that the three carbides are inevitable exit at the same time. The phenomenon makes it hard to determine the electronic property, for example, work function, that is important for the field emission. The inset in Fig. 4.25(b) shows the lateral section of the carbon nanotips with tip end points to the right. It shows the parallel graphitic layers stretch along the growth direction just like carbon nanofiber[168] but accompany with decreasing shorter layer around them.

Fig 4.26 shows the surface morphologies of nanotips grew with different H_2/CH_4 ratio. As can be seen, the nanotip structure grows when the H_2/CH_4 ratio is higher than 30/10 [Fig. 4.26(b), (c)], otherwise only carbon film is formed [Fig. 4.26(a)]. When the H_2/CH_4 ratio reaches 100/10, the structure starts to lose its shape [Fig. 4.26(d)]. Fig. 4.27 shows the morphologies of nanotips grew at different biases. No nanotips would grow [Fig. 4.27(a)] unless there's sufficient bias. It is found that only when the bias is larger than 100V, the nanotips would grow [Fig. 4.27(b)]. With the increasing bias, the nanotips change their appearance. With high bias of 200V or 300V [Fig. 4.27(c), (d)], an "asparagus-like" structure is formed.

The graphitization of the nanotips is shown in Fig. 4.28 and is expressed by I_D/I_G ratio obtained from Raman spectroscopy. The curve of I_D/I_G ratio on the top-right indicates the trend of graphitization with the same bias of 150V. Similar to carbon nanotubes, the I_D/I_G ratio decrease with the increasing hydrogen flow that represents the higher degree of graphitization due to selective etching between amorphous carbon and graphite. Another curve represents the graphitization degree with different biases that grow with H_2/CH_4=40/10. The increasing bias corresponding to a lower I_D/I_G ratio shows that the applied bias effectively assists the deposition of graphite and removes the amorphous carbon. Fig. 4.29 shows the growth of tip

length with time under bias of 150V and 300V. The results show that the high bias of 300V is effective in assisting the growth of nanotips at initial stage; however, the ultimate length is about 0.5μm, much shorter than the 150V case, which is about 1.5μm.

The surface morphologies change with growth time is demonstrated in Fig 4.30. Fig. 4.31 represents the schematic diagram of the corresponding growth stages showed in Fig. 4.30 for the growth of chromium carbide capped carbon nanotips. The substrate was first treated with H_2 plasma to remove the passive layer and created certain roughness [Fig. 4.30(a) and Fig. 4.31(a)]. The reaction gas mixtures were then flow into the chamber to join the deposition process [Fig. 4.30(b) and Fig. 4.31(b)]. As the deposition keeps on, the carbon tends to deposit on the root of the nanotips and the nanotips therefore connect to each other on the root part [Fig. 4.30(c) and Fig. 4.31(c)]. After the catalyst lost its activity, the nanotips stop to grow and the following carbon therefore forms a continuous film [Fig. 4.30(d) and Fig. 4.31(d)]. Analogous to carbon nanotubes, chromium act as catalyst for the precipitation of carbon atoms, which may be a vapor-liquid-solid growth mechanism similar to the growth of carbon nanotubes[169] or carbon nanofiber.[168] But one thing is that the chromium did carburize during deposition, which the carbide is very stable. This suggests that surface diffusion[170] become the main process for the growth. The carbon nanotips also increase its diameter during growth by vapor-solid process which means the carbon species deposited directly onto the tip body. The applied bias larger than 100V is essential for the growth of chromium carbide capped carbon nanotips. This is probably because the bias provides a higher reactant concentration around the chromium with relatively higher ion energy, and also the sharpness of the tips induces strong charge to attract positive ions. The high activation energy of chromium to diffuse carbon also leads to the growth of carbon nanotubes using chromium as catalyst been rarely seen.

Interestingly, bias helps the growth of the tips, but also destroys it, too. Accompany with the growth of nanotips, ion bombardment effect is drastic due to the strong field applied

by the DC bias[171]. The growth of chromium carbide capped carbon nanotip is a competition between carbon deposition and ion bombardment. Under bias of 150 volts, the diameter of carbon nanotips increases from the as-grown diameter of 40nm with increasing time. But under high bias of 300V, the diameter of nanotip maintains about 40nm or less and some even breakdown from its neck, which is revealed in Fig. 4.27(c), (d). This is also direct evidence that the chromium carbide is efficiently resistant to ion bombardment and provides shield the carbon nanotip, which might indicate a way to improve field emission life time for applications. According to the phenomenon we observed, unlike carbon nanotubes of carbon nanofiber, a length limit exists. This might due to the fully carburization of chromium that leads to a result of deficiency in diffusing carbon. Bias in microwave plasma chemical vapor deposition for most of cases increases the deposition rate.[151] The higher bias contributes to the faster formation of chromium carbide that limits the length of the nanotip. The following carbon thus starts to deposit around the chromium carbide, where the high field induced by tip sharpness and a higher carbon supplement become the preferential sites and makes them look like asparagus.

In fact, some similar phenomenon were also been observed for other elemental catalyst. In this way, from Fowler–Nordheim model,[109] the work function, φ, can be easily tuned for further improvement in field emission or use the special property of materials in some specific applications.
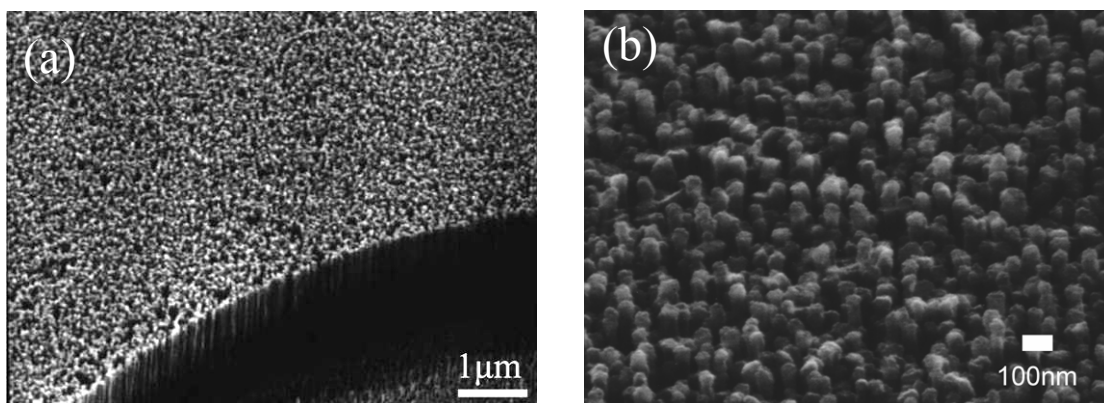
Fig. 4.24 (a) Low magnification SEM image showing the uniformity of the vertical aligned chromium carbide capped carbon nanotips and (b) higher magnification top view image.
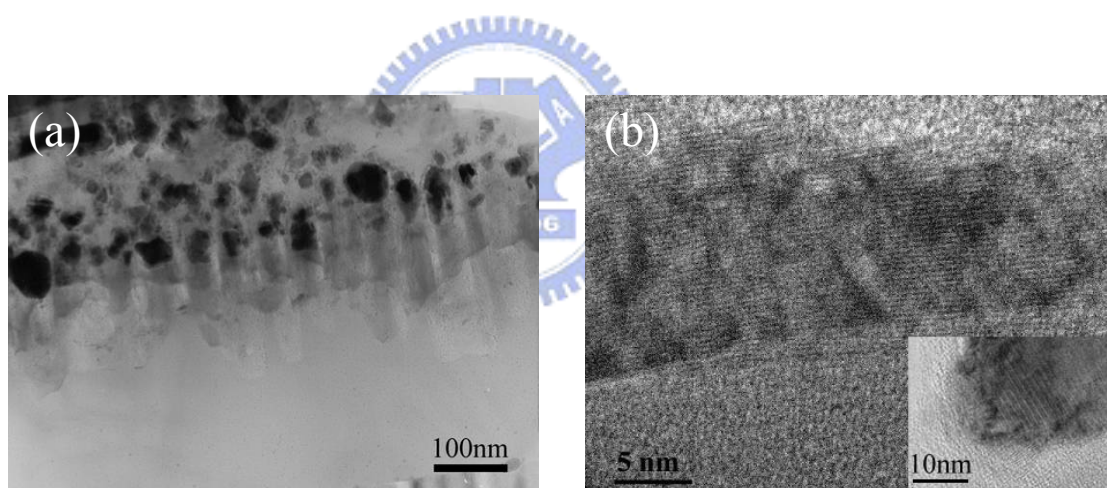
Fig. 4.25 TEM images showing (a) the cross-section view of chromium carbide capped carbon nanotips and, (b) high magnification view of an individual carbon nanotip and the inset shows the chromium carbide head.[164]
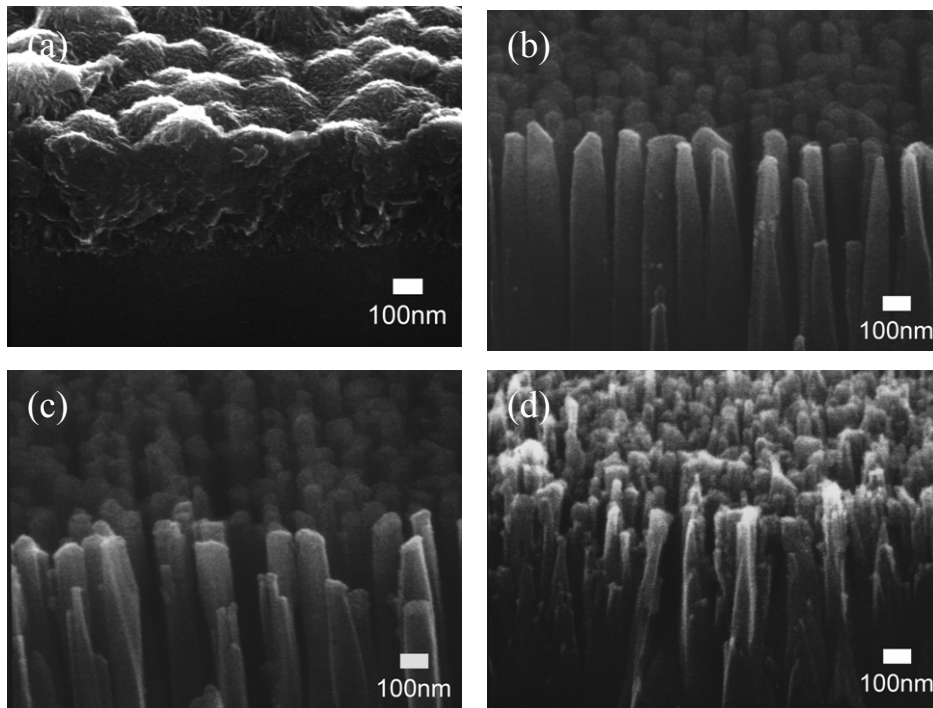
Fig. 4.26 SEM images of surface morphology change with H_2/CH_4 of (a) 10/10, (b) 30/10, (c) 50/10 and (d) 100/10.
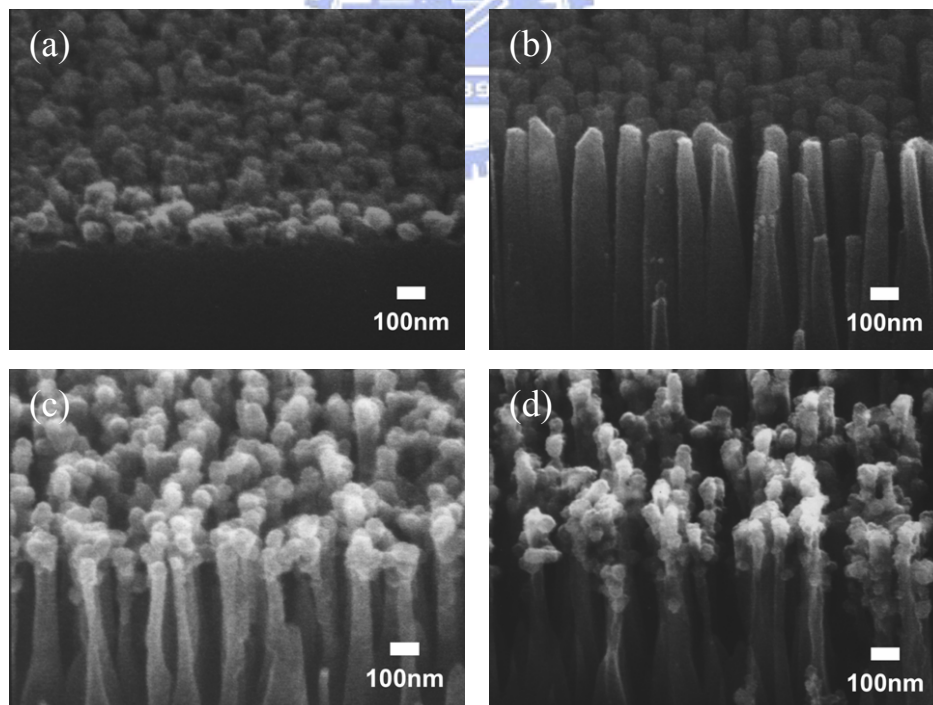
Fig. 4.27 SEM images of surface morphologies with applied biases: (a) 100V, (b) 150V, (c) 200V and (d) 300V.
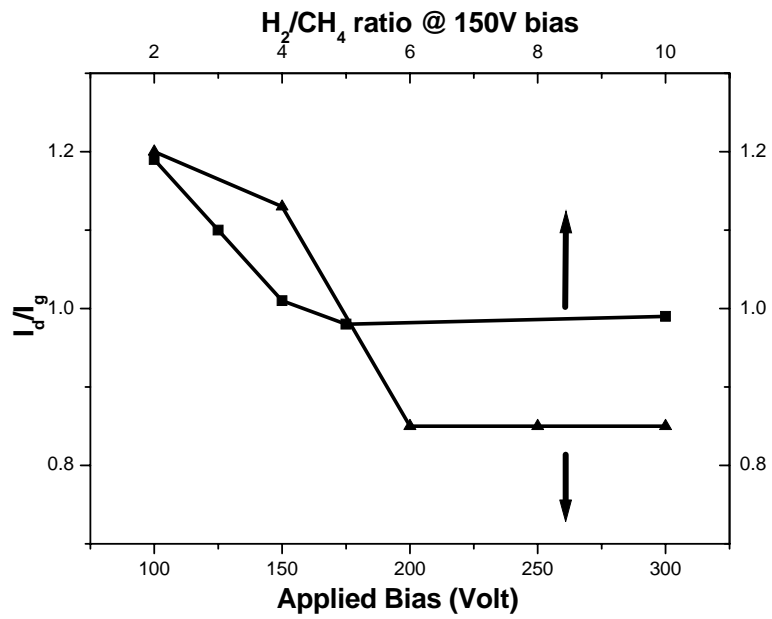
Fig. 4.28 Ratios of I_D/I_G with methane concentrations and biases.
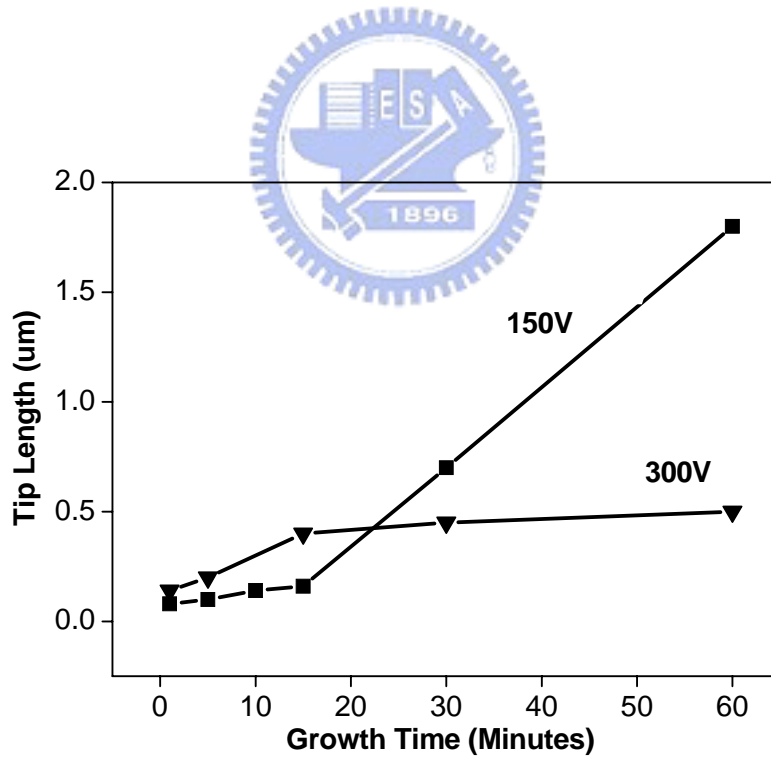
Fig. 4.29 Tip length variation with growth time under applied bias of 150V and 300V.
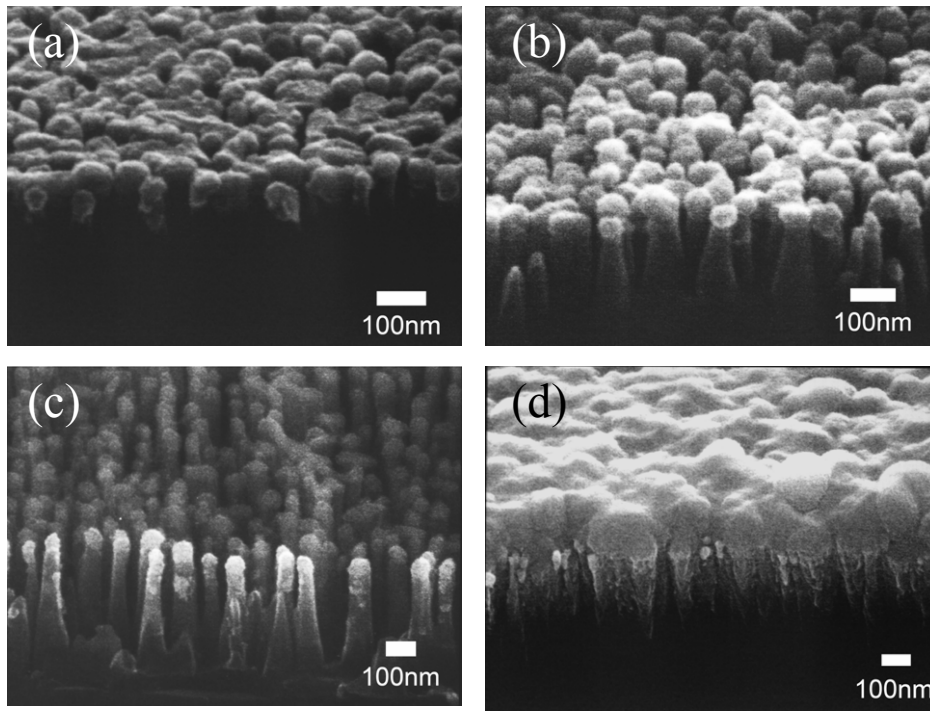
Fig. 4.30 Surface morphologies of chromium carbide capped carbon nanotips with different growth time.
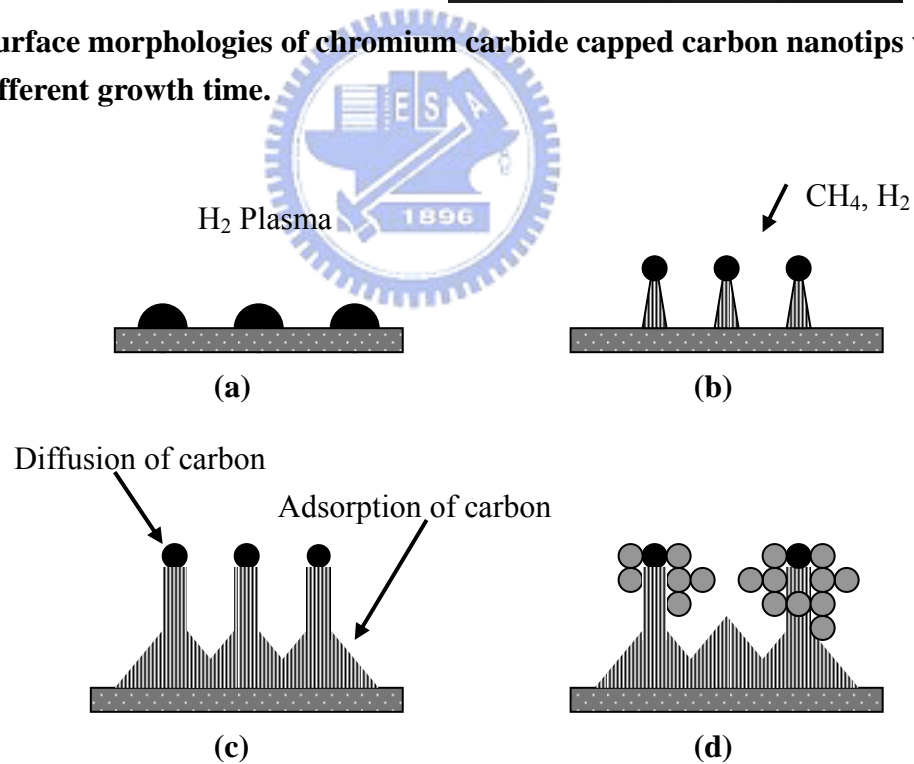
Fig. 4.31 Schematic diagram of the proposed growth model: (a) formation of the nucleation process; (b) cap growth; (c) deposition of carbon; (d) asparagus-like structure forms.

4.4.2 Field Emission Properties of Chromium Carbide Capped Carbon Nanotips and

    Bare Carbon Nanotips

The previous section has shown the uniformity and nanosize of the chromium carbide capped carbon nanotips. The characters make it a good candidate for field emission applications. In our team's previous work, an original type of carbon nanotips was synthesized on bare silicon. Due to their similarities of structure (which both consist of graphite body) and dimension (which are about 1μm, relatively short compare to the CNTs), we compare the two materials to figure out the effects of the chromium carbide on the field emission properties.

Fig. 4.32(a) and (c) show the surface morphology of the carbon nanotips and chromium carbide capped carbon nanotips, respectively by SEM observation. The growth parameters were chosen to grow the two kinds of nanotips to about 0.5μm in their length, as to ensure the similar conditions for field emission measurements. The tip end of the carbon nanotips consist of several graphene layers which were less than 0.1 nm [Fig. 4.32(b)]. The d-spacing of the graphite is 3.57Å which showed a deviation from perfect crystalline graphite (002) plane of 3.395Å and a large difference from Si(100) of 3.290Å. The chromium carbide capped carbon nanotips ends with crystalline nanoparticles which was about 40nm and the diameter of the graphite right beyond the chromium carbide was a few nanometers smaller than the chromium carbide [Fig. 4.32(d)]. The chromium film deposited for the growth of the capped carbon nanotip was used as catalyst and was carburized into chromium carbide which was gradually lifted-off during growth. The diameter of the two kinds of nanotips gradually increased toward the substrate via vapor-solid growth and may reach to about a hundred nanometers. The graphene layers of the nanotips body were perpendicular to the silicon substrate for both nanotips and were important to electron conduction.

Relationship between field emission current density with electric field of the as grown materials was shown in Fig. 4.33. Due to the ultra-sharpness of the bare carbon nanotips, a

low turn-on field (defined as the field required to emit a current density of $10\mu A/cm^2$) of 1.40V/μm can be reached. With chromium carbide, the tip structure exhibited a much higher turn-on field of 3.50V/μm. Basically, the results differed from the surface appearances of which the field enhancement factor was greatly affected by the geometrical distribution. The sharp and less dense of the carbon nanotips also comparatively reduced screening effect [10, 11] due to a larger tip-to-tip spacing. The insets of Fig. 4.33(a) and (b) show respectively the Fowler-Nordheim (FN) relations. The linearity of the plot at the initial applied voltages before turn-on suggested the behavior of FN tunneling of the electron emission process.

Fig. 4.34 shows the applied field as a function of emission time under constant current density which was set to 1mA. Total emission time was 36,000 seconds, which was 10 hours. The degree of stability of field emission was obviously quite different. The mean electric field for chromium carbide capped carbon nanotips was 8.02V/μm with fluctuation less than 5 percent can be achieved. On the contrary, although the carbon nanotips showed a superior turn-on and thresholds field on the beginning of the test, the situation became chaotic after about ten thousand seconds. The oscillation was mainly due to the physical damage of the tip, which was confirmed by post observation of SEM. Instead, the chromium carbide capped carbon nanotips showed a smoother surface after the test without distinguishable major change. This phenomenon suggests that chromium carbide, known for its excellent oxidation resistance and hardness, effectively shield the carbon nanotips from destruction, which may mainly due to ion bombardment, heating and oxidation. Here we had assumed that the field emission current arise from the chromium carbide nanoparticles since the ends of the nanotips suffer a larger electric field and field enhancement, in contrast to the graphite body.

On the other hand, the extremely sharp of the carbon nanotips would cause a great amount of current density arise over the tip and generate a lot of heat due to ohmic heating. The uniformity of the capped carbon nanotips also benefited to the lifetime experiment while the disorderliness of the uncapped nanotips causes un-equivalent current contribution and as a

result of breakdown sequentially.

Chromium carbide has been synthesized and used for long period of time, but were focus on the bulk applications such as hard coatings for tribological use. Therefore, the electric properties have not been totally explored so far. Reports have shown that Cr_3C_2 with conductivity of $6.8\times10^6\Omega^{-1}cm^{-1}$ was used as conductive ceramics[172] and Cr_7C_3, which was the main structure of the chromium carbide nanoparticles in this study, may exhibit metallic behavior proposed from the chemical bonding structure.[173] In fact, the defects in the chromium carbide may also provide a low energy conduction path.[174]. In this case the situation may be more complex since we were dealing with more than one material. The difference in work function between the carbides or between carbide and graphite could form ohmic and Schottky junctions which may limit the current. Even though the existence of the chromium carbide may not be favorable for electron conduction, the steady emission had shown importance for practical application.

Fig. 4.35 shows the image that was taken by digital camera from the vacuum chamber during the field emission measurement for chromium carbide capped carbon nanotips. The image shows the phosphor being light up by the field emission current with an acceptable uniformity.
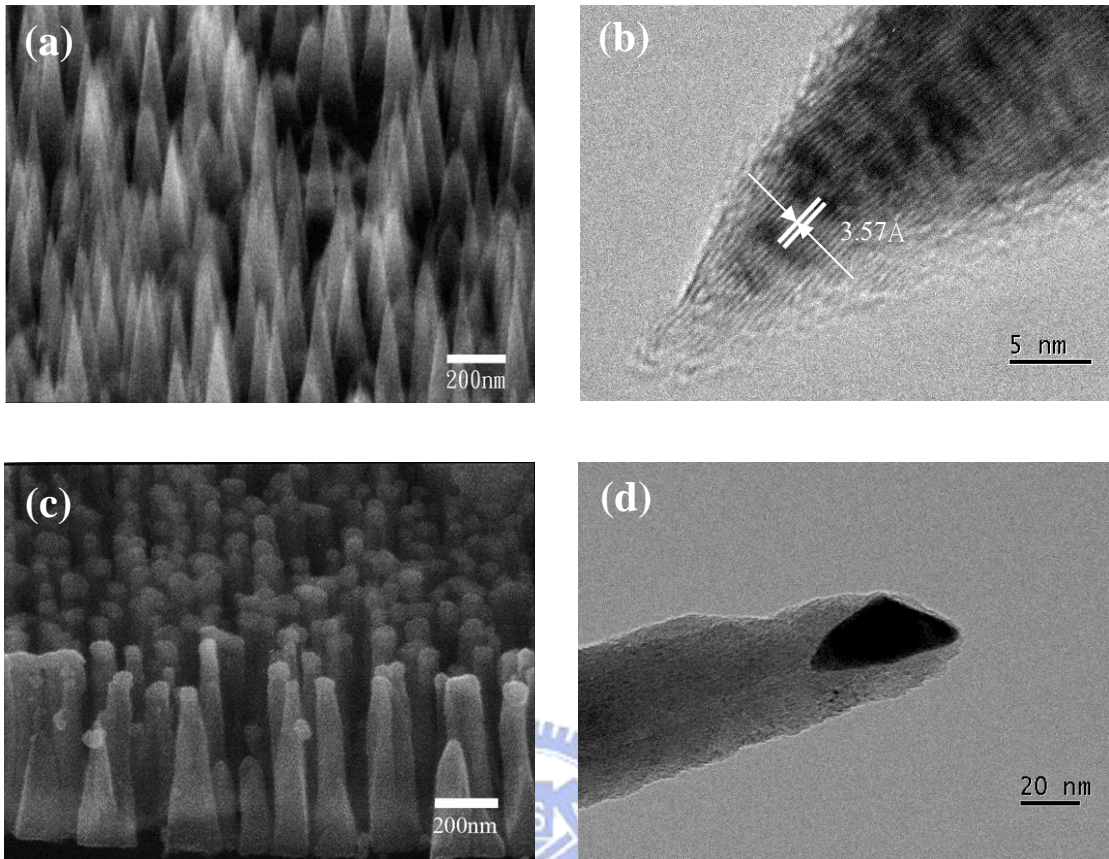
Fig. 4.32 SEM images showing the surface morphology of (a)(b) carbon nanotips and (c)(d) chromium carbide capped carbon nanotips.
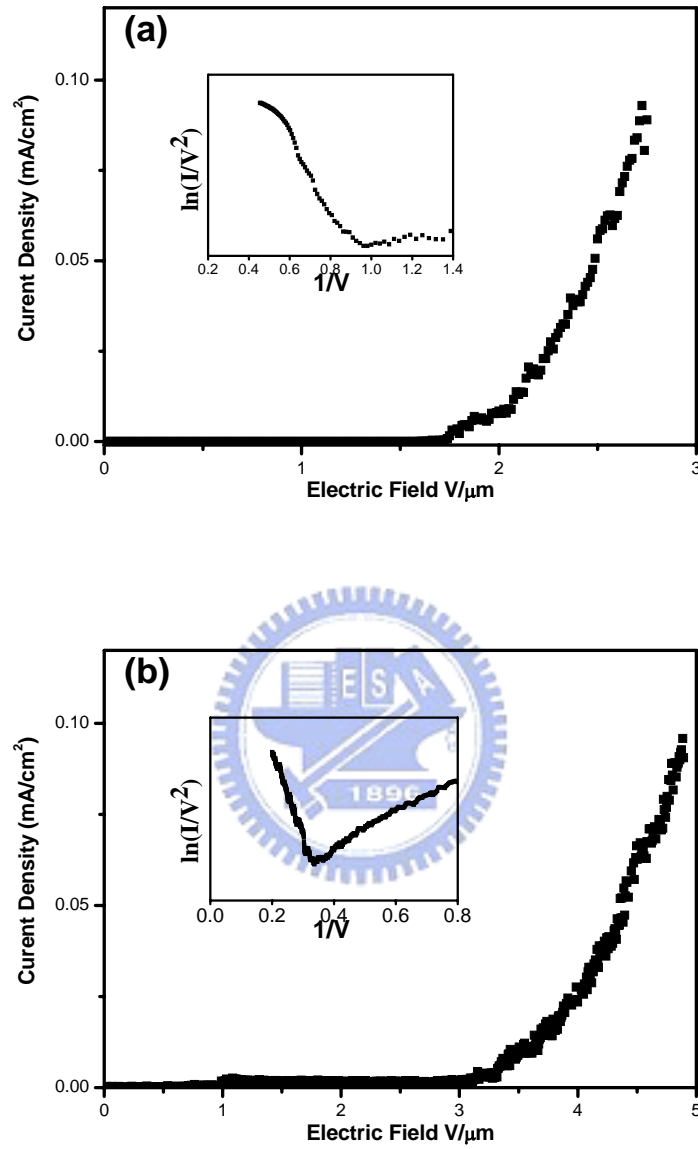
Fig. 4.33 The field emission current density as a function of the electric field for (a) carbon nanotips and (b) chromium carbide capped carbon nanotips. The insets show the Fowler-Nordheim plot for each material.
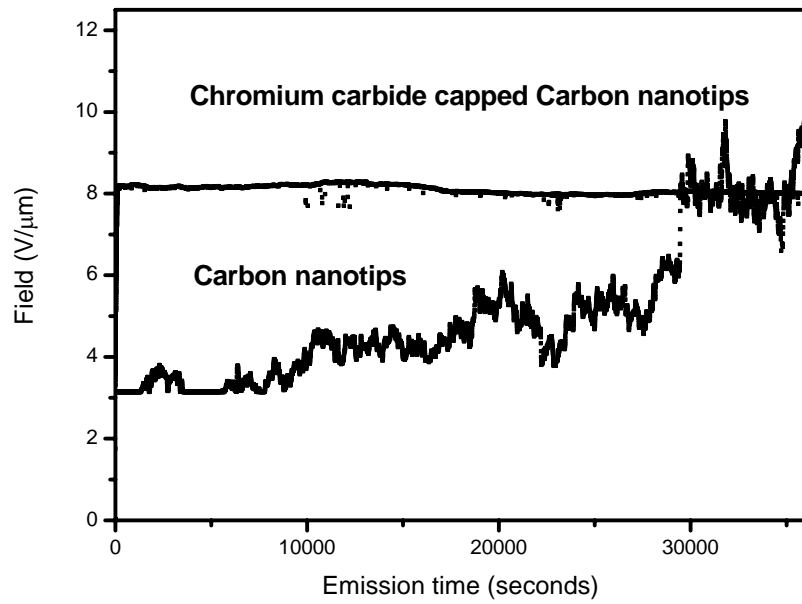
Fig. 4.34 Plot of electric field with emission time for carbon nanotips and chromium carbide capped carbon nanotips. The current was set to a constant value of 1mA.
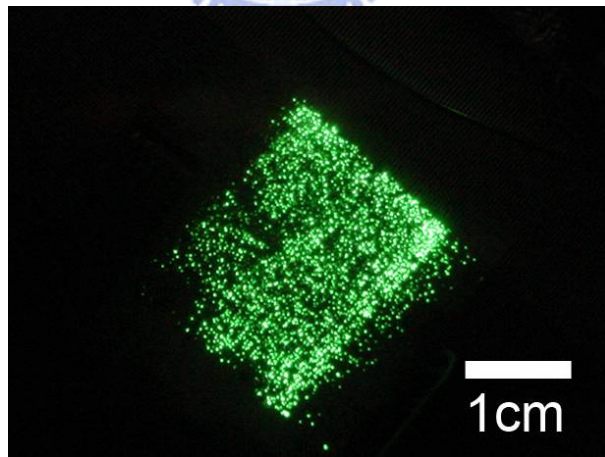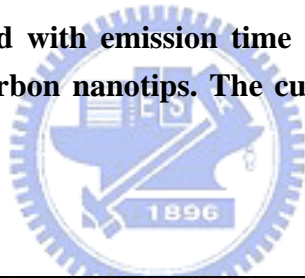
Fig. 4.35 Image of the lighted phosphor in vacuum chamber during field emission measurement test which is taken by digital camera.

4.5 Synthesis and Field Emission of Chromium Carbide capped Carbon Nanotips in Gated Structures

In chapter 3, the fabrication process of the gated structure using Pt and Ti as conductive layer has been shown. Generally the structure can also be achieved by using n^+ poly-Si as the gate material. Fig. 4.36 shows the schematic diagram of the fabrication processes. Compare to the processes using metal as the gate material, several steps were reduced when using poly-silicon. It is due to that only one photolithography step is required since the patterned poly-Si can easily be removed by reactive ion etcher. The poly-Si and oxide can therefore be etched away in a single step. Also the pattern for the etching of poly-Si and silicon oxide can also be used as the pattern for Cr deposition. The photoresist is removed at the last fabrication step. Though the n^+ poly-Si simplifies the fabrication process, however, the material caused problem in the growth step of the chromium carbide capped carbon nanotips. Fig. 4.37 shows the surface morphology of the structure. In Fig. 4.37(a) and (b), it is obviously seen that the carbon tend to deposit on the edge of the hole pattern. It should be due to the poor conductivity of the poly-Si (compare to metals) that the negative charges tend to pile up at the edge and creates a preferential site for the deposition. The charges also contributed to irregular growth inside the hole. There's a more serious problem which can be seen in Fig. 4.37(b). Half of the poly-Si is etched away during a 30min growth and only 100nm of poly-Si left. Hence, we preferentially used Pt as the gate material to prevent such problems, only we had to tune the parameters to prevent the deposition of carbon on the Pt in which the poly-Si has fewer problems.

Fig. 4.38 shows the gated structure with chromium carbide capped carbon nanotips grew inside. Fig. 4.38(a), (b) show the structure with 4μm diameter and Fig. 4.38(c), (d) show the structure with 8μm diameter. The growth was achieved with bias of 150V and $H_2/CH_4=50/10$ and duration for 15min with 15min of H_2 pretreatment. The parameters show that the three dimension structure induced a barrier for the gas diffusion and higher hydrogen flow was

needed. Besides, the images show that there's no much difference for the two pattern size. Fig. 4.39 shows the cross-section image of the nanotips in the hole. The interface between the nanotips and the silicon wafer indicates a selective growth behavior instead of directly etching of the wafer. As for the planer case, the material also exhibits vertical alignment in the hole-structure. However, due to the poor diffusion inside the structure, the nanotips only grow for maximum length of 0.5μm which is much shorter than the 1.5μm for the planer case.

In order to further increase the length of the nanotips in the gated structure which also means to decrease the distance between the tip and gate, we make efforts on the effects of the applied biases. Fig. 4.40 shows the cross-section images of the 8μm structure. The results show that the applied biases can further increase the tip length; however, the augmentative length is due to the etching of the Si substrate [Fig. 4.40(b), (c)] and the tip-to-gate distance remains the same. Besides, the deposition of carbon on Pt has many disadvantages for the further field emission measurements. Here we suggest that a bias of 150V [Fig. 4.40(a)] is the optimized bias for the growth of nanotips in the structure.

The result of field emission measurement of the structure is shown in Fig. 4.41. Fig. 4.41 shows the typical I-V curve. We can obtain that when the voltage is 3.30V, a current of 10μA can be achieved. Fig. 4.41(b) shows the F-N plot of the device showing a field emission behavior. Since there are some argues about the definition of the field emission area for the gated device due to the field distribution,[175] we defined the turn-on field from the F-N plot which demonstrates in Fig. 4.41(b), a value of 2.63V (or 5.26V/μm) could be obtained. Fig. 4.42 shows the images of chromium carbide capped carbon nanotips grew on a planer surface. The images show the selective growth behavior from a pre-pattern silicon wafer. The gaps between the two sides of nanotips are 6μm, 10μm and 20μm, respectively. The approaches may be applied to another field emission device that the controlling gate is located on the same plane. The SED or SCE[176] (Surface conducted emission device) makes it even more easy to fabricate the devices.

1. 6" n-type (100) Si wafer

2. Wet oxidation (5800Å) by furnace

3. Deposit n+ poly-Si by furnace

4. Define photoresist

5. Etch of poly-Si and silicon oxide

6. Cr coated by PVD

7. Photoresist life-off

8. Selective growth of Carbon nanotips by MPCVD

Si   SiO$_2$ PR   Cr

n+ poly-Si   Nanotips
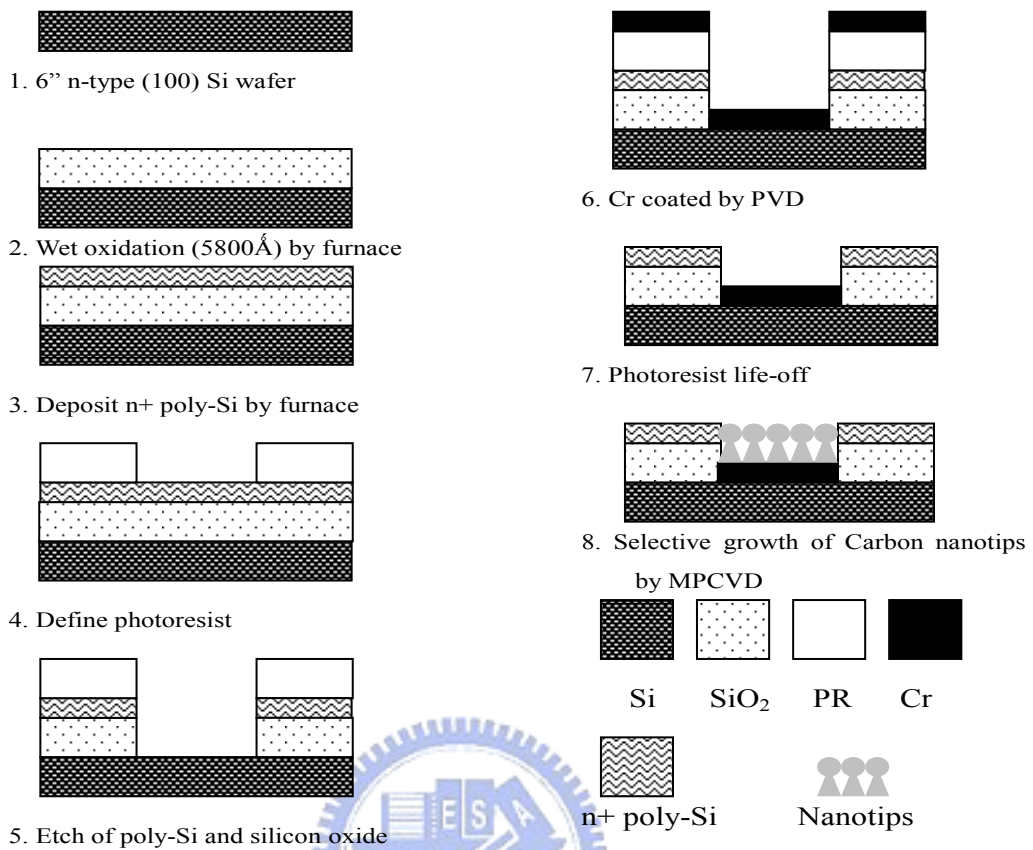
Fig. 4.36 Fabrication process of the gated structure using n$^+$ poly-Si.
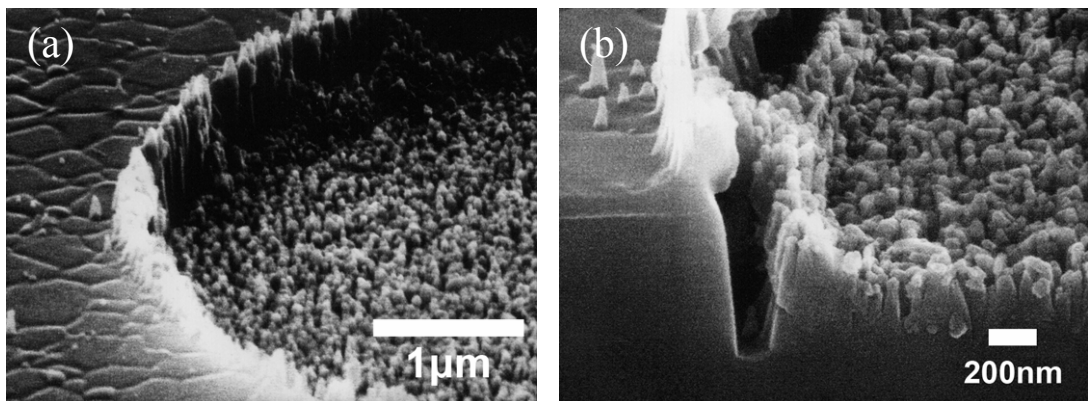
Fig. 4.37 SEM images of the gated device with n$^+$ poly-Si layer showing (a) carbon deposit on the edge of the poly Si and (b) the poly-Si is etched away in plasma.
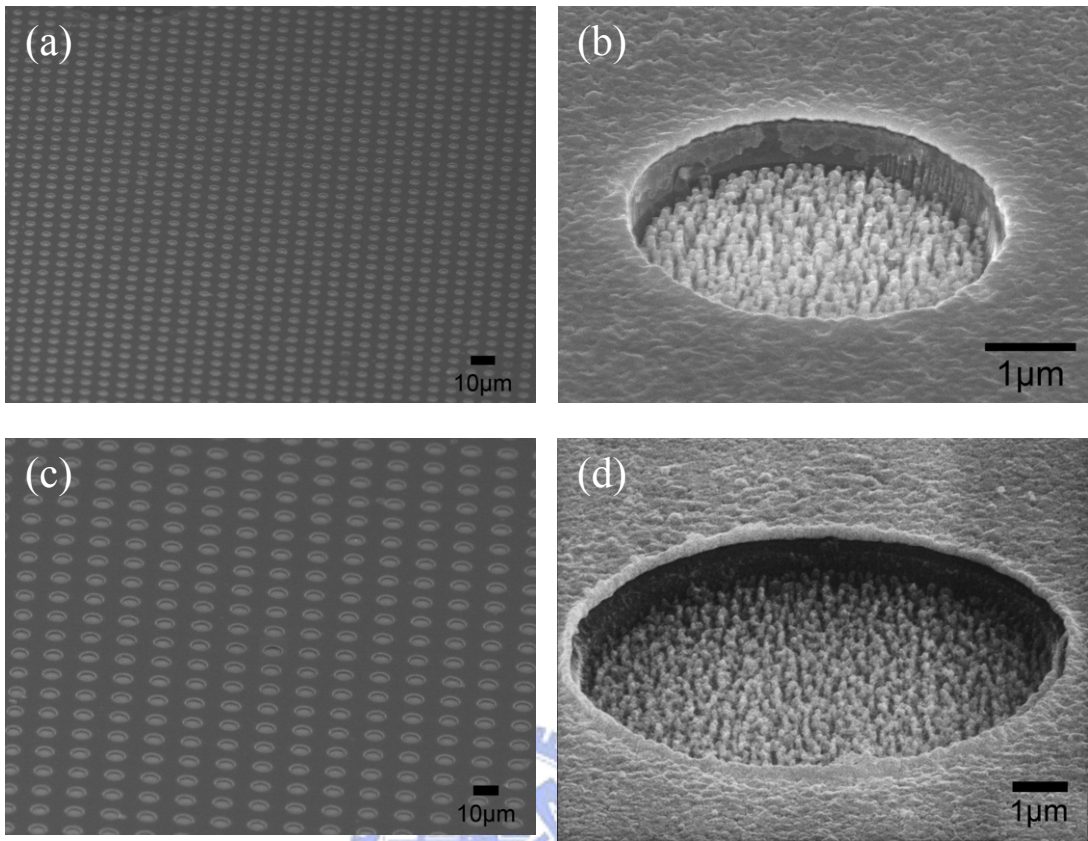
Fig. 4.38 SEM images of chromium carbide capped carbon nanotips grow in the gated structure.
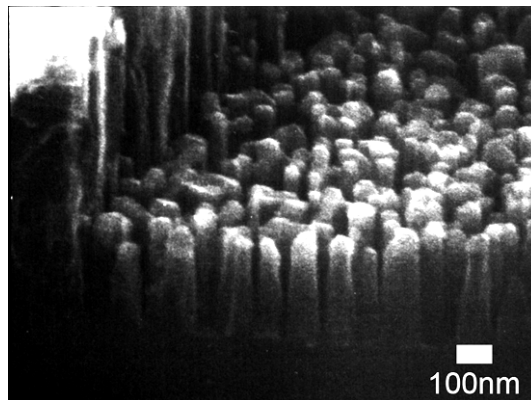
Fig. 4.39 SEM image of the chromium carbide capped carbon nanotips showing high alignment.

Top-View   **Cross-section View**
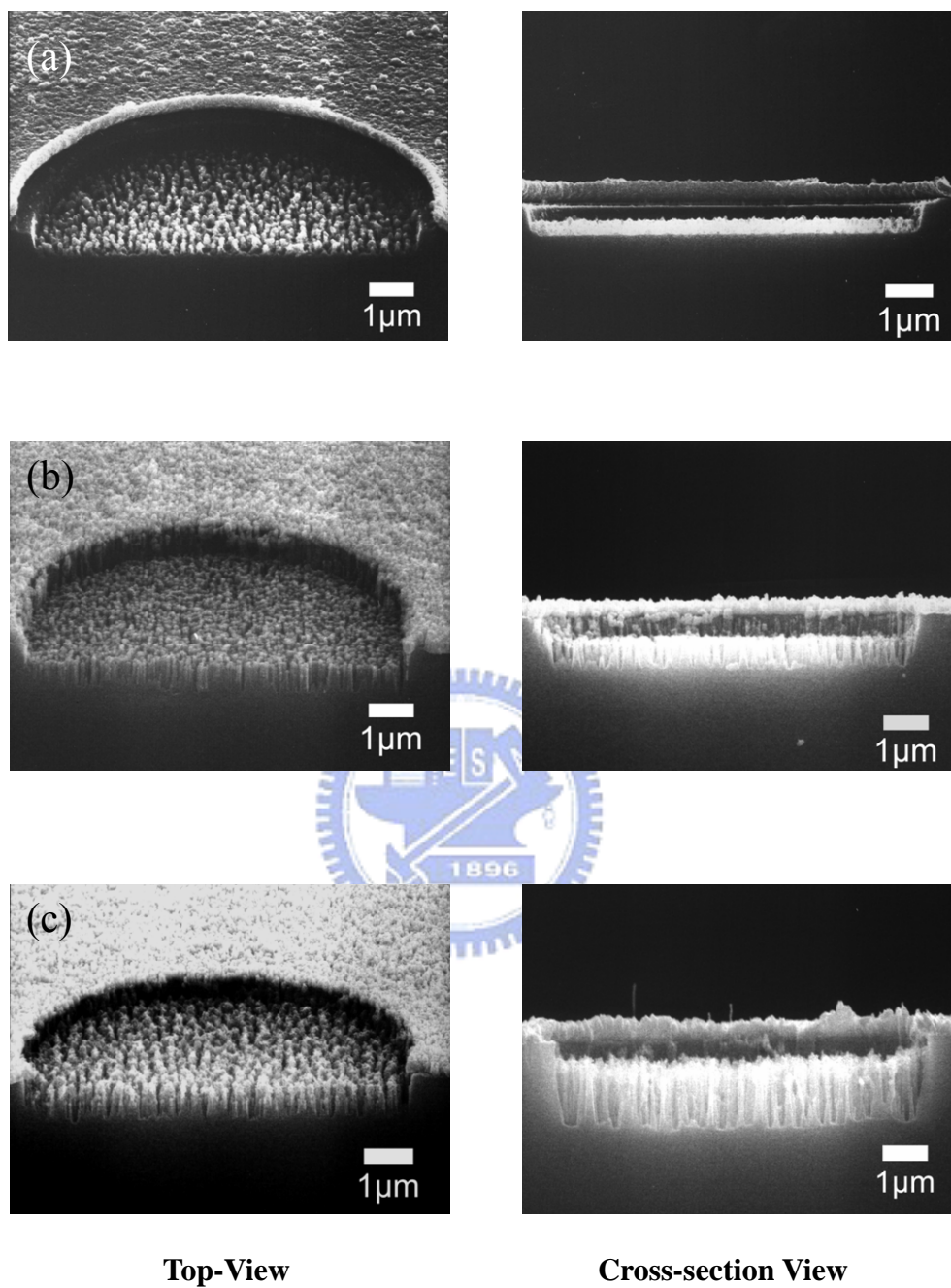
Fig. 4.40 SEM images of chromium carbide capped carbon nanotips grow in triode structure with bias of (a) 150V (b) 200V (c) 250V, respectively.
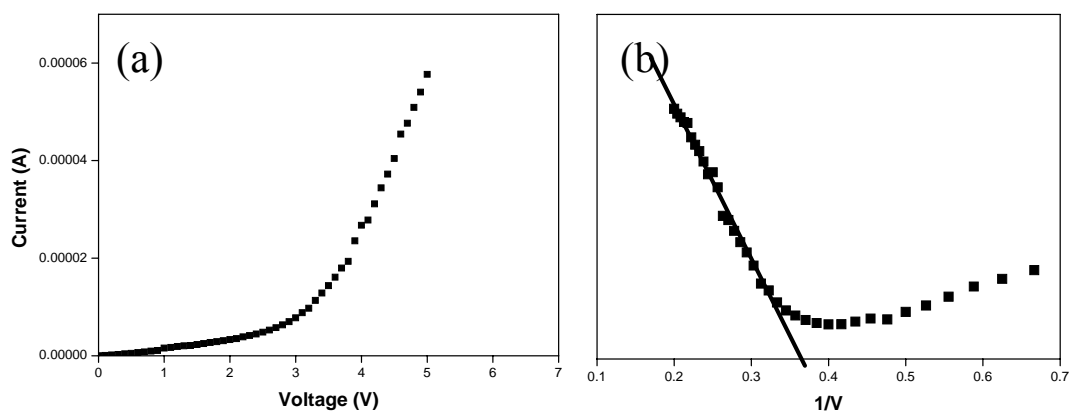
Fig. 4.41 Field emission measurements of the gated structure: (a) I-V and (b) F-N plot.
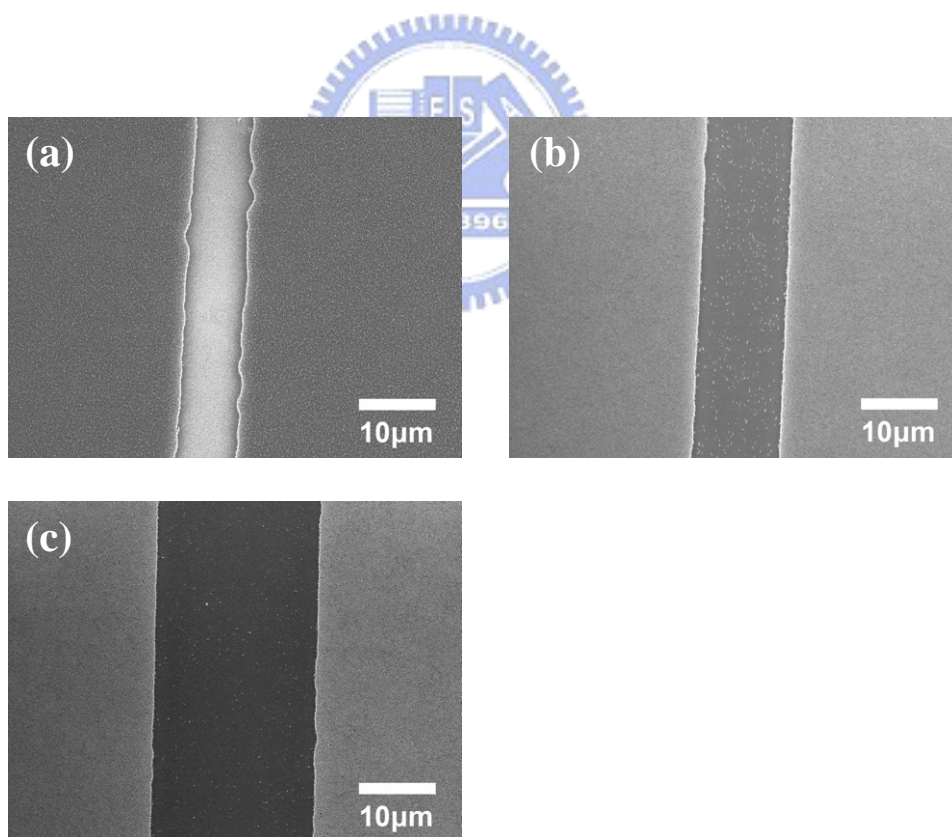
Fig. 4.42 Selective growth of chromium carbide capped carbon nanotips on planer surface with gaps of (a) 6μm, (b) 10μm and (c) 20μm.

4.6 Comparisons between Carbon Nanomaterials in the Study

Table 4 shows a brief summary of experiment results of the carbon nanomaterials in the thesis. Among these materials, bare carbon nanotips have the sharpest tip radius which is more favorable for field emission. However, the catalyst-free growth contributes to a slow growth rate. Besides, the field emission stability is poor and shows no trend of aging effect like CNTs do. On the contrary, by using catalyst of Fe or Ni, the growth rate can increase enormously to a value of 2μm/min. In the case of chromium carbide capped carbon nanotips, due to the low diffusivity of carbon in chromium and loses of activity; they can only grow to a maximum length of about 1.5μm/min. CNTs grown by Cr and Ni/Au alloy show a value of 0.33μm/min.

The differences of the growth rate of chromium and iron on the growth of CNTs could be explained by thermodynamic analysis. Table 5 shows the Gibbs free energy for the formation of the carbides. It has been mentioned in section 4.4.1 that chromium easily forms three carbides. The high negative values shown in Tab. 5 indicate stable phases are preferred. The stable carbides loose the catalytic behavior and diffusion of carbon therefore becomes much difficult. On the contrary, iron carbide has a positive free energy which indicates a non preferred reaction. Although the values are about zero, the reverse reaction could more easily proceed. On the other hand, the melting point of chromium is 1857°C, much higher than iron (1535°C) or nickel (1453°C), which makes the VLS route more difficult. For the same chromium case, the long H_2 plasma pretreatment time leads to fine catalyst particles which make it possible for more inter-granular diffusion. The higher carbon diffusion rate therefore assists the growth of CNTs or otherwise chromium carbide capped carbon nanotips are formed.
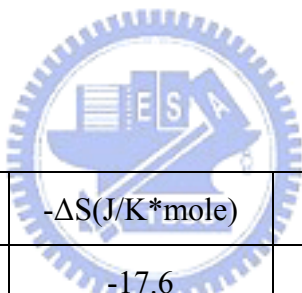
Fig. 4.43 shows the field emission I-V comparison of the carbon nanotips and CNTs grown by Fe and Cr. The turn-on fields of bare carbon nanotips and CNTs grown by Fe and Cr are about 1.50V/μm due to their good conductivity and aspect ratio. On the contrary, the

chromium carbide capped carbon nanotips show a highest turn-on field of 3.50V/μm. However, the chromium carbide capped carbon nanotips show superior field emission stability (Fig. 4.34) because of the uniformity and the resistance to decade. In the case of CNTs, although the initial stability is poor, aging could provide a way to improve the performance after 30min of field emission which can be seen in Fig. 4.44. Except of the intrinsic properties that affect the field emission properties, we could use special pretreatment of annealed Ni/Au alloy to decrease the density of CNTs to effectively lower the turn-on field.

	CNTs			Carbon nanotips	
Catalyst	Fe	Cr	Ni,Au	None	Cr
Tip diameter (nm)	50	10	50	0.1	50
Length (μm)	30	5	5	0.5	0.5
Growth rate (μm/min)	2	0.33	0.33	0.02	0.04
Turn-on field (V/μm)	1.49	1.55	2.8-5.5	1.40	3.50
Stability	Medium (Aging)			Poor	Good

Table 4 Comparisons between carbon materials in the thesis.

	ΔH(J/mole)	$-\Delta S$(J/K*mole)	Range (K)	ΔG(J/Mole) @ 1000K
Cr_3C_2	-79,100	-17.6	298-2130	-93,700
Cr_7C_3	-153,500	-37.2	298-2130	-190,700
$Cr_{23}C_6$	-309,000	-77.4	298-1773	-386,400
Fe_3C (α)	29,000	-28.0	298-1000	1
Fe_3C (γ)	11,200	-11.0	1000-1410	0.2

Table 5 Thermodynamic data of the chromium carbide and iron carbide.[177]
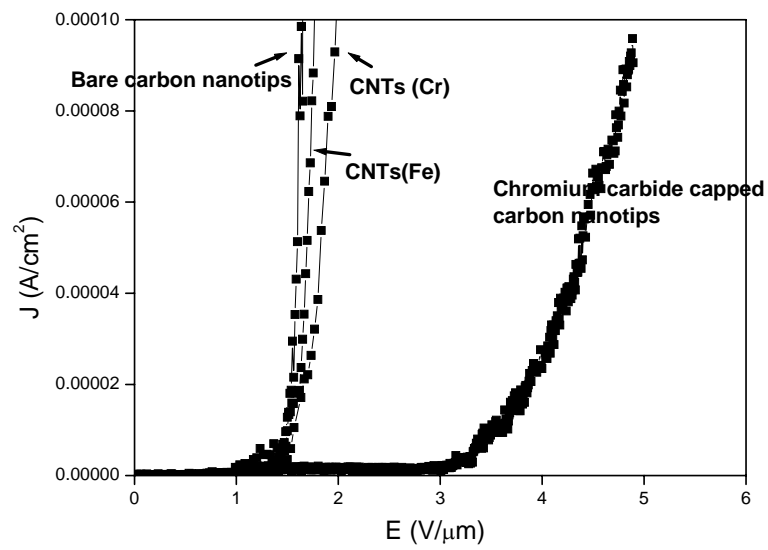
Fig. 4.43 Field emission I-V curves of different carbon nanomaterials.
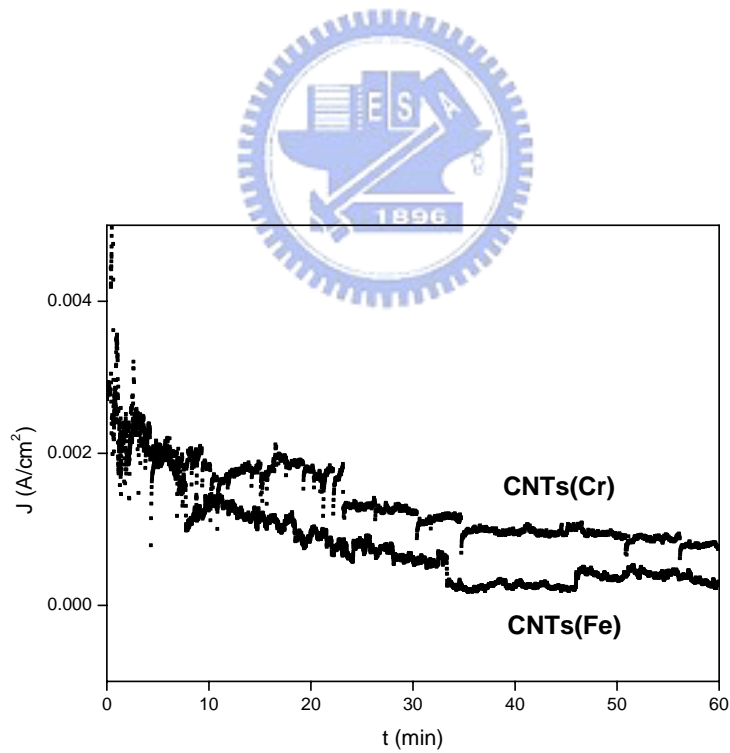
Fig. 4.44 Life-time measurements of CNTs grew from Fe and Cr.

Chapter 5 Conclusions

1. Instead of Fe, Cr is able to grow CNTs with good alignment and high density. Under H_2 plasma treatment for 30min and H_2/CH_4=40/10 with bias of 150V for 15 min, CNTs with length of 3μm and tip-diameter of 10nm. The field emission stability for both Fe and Cr can be improved after a 30min field emission aging.

2. Binary system with gold and nickel successfully inhibits the continuous film of carbon nanotubes formation. The density of CNTs can be reduced to the value of $3.3 \times 10^7 cm^{-2}$ by changing the composition and the heat treatment of the catalyst film. Field emission measurement shows a value close to the reported density of $2.5 \times 10^7 cm^{-2}$ and is possible for optimizing field emission efficiency for practical applications.

3. SiONWs could be grown on nickel/gold-coated silicon oxide substrates by rapid furnace annealing. Octopus-like structure of SiONWs could grow to tens of micrometers with diameters of tens of nanometers depending on the catalyst composition, amount and cooling rate.

4. Under critical conditions of nickel and gold film thicknesses of 15 and 8 nm and cooling rate of about 1.8℃/s, aligned SiONWs with unattached ends could be grown. The growth of the SiONWs was proposed to be a unique head-growth SLS process accompanied by cell growth induced by constitutional supercooling.

5. Instead of CNTs, Cr can be used as a catalyst to grow chromium carbide capped carbon nanotips. These nanotips grow with good uniformity and show good alignment. The results show that bias larger than 150V is necessary for the growth and helps the graphitization.

6. Field emission characteristics of carbon nanotips and chromium carbide capped carbon nanotips were investigated and showed a turn-on field of the bare carbon nanotips (1.4V/μm) lower than the chromium carbide capped carbon nanotips

(3.5V/µm). The bare carbon nanotips show poor stability while chromium carbide capped carbon nanotips reveal a much stable emission.

7. Growth of chromium carbide capped carbon nanotips in the gated structure is achieved. Turn-on field (defined as the linear fit of F-N plot intercept the 1/V axis) is approximately 2.63V. The current of 10uA is achieved at 3.3V.

References

[1]   G. E. Moore, "Cramming More Components onto Integrated Circuits," Proceedings of the IEEE, 86 (1998) 1.

[2]   A. P. Alivisators, "Semiconductor Clusters, Nanocrystals, and Quantum Dots," Science, 271 (1996) 933.

[3]   J. M. Krans, J. M. van Rutenbeek, V. V. Fisun, I. K. Yanson and L. J. de Jongh, "The signature of conductance quantization in metallic point contacts," Nature, 375 (1995) 767.

[4]   K. K. Likharev, "Correlated discrete transfer of single electrons in ultrasmall tunnel junctions," IBM J. Res. Dev., 32 (1998) 144.

[5]   G. Markovich, C. P. Collier, S. E. Henrichs, F. Remacle, R. D. Levine and J. R. Heath, "Architectonic Quantum Dot Solids," Acc Chem. Res., 32 (1999) 415.

[6]   O. H. Elibol, D. Morisette, D. Akin, J. P. Denton, and R. Bashir, "Integrated nanoscale silicon sensors using top-down fabrication," Appl. Phys. Lett., 83 (2003) 22.

[7]   M. A. Reed, C. Zhou, C. J. Muller, T. P. Burgin and J. M. Tour, "Conductance of a Molecular Junction," Science, 278 (1997) 252.

[8]   M. Shimomura and T. Sawadaishi, "Bottom-up strategy of materials fabrication: a new trend in nanotechnology of soft materials," Current Opinion in Colloids and Interface Science, 6 (2001) 11.

[9]   A. Thess, R. Lee, P.Nikolaev, H. Dai, P. Petit, J. Robert, C. Xu, Y. J. Lee, S. G. Kim, A. G. Rinzler, D. T. Colbert, G. E. Scuseria, D. Tomanek, J. E. Fischer and R. E. Smalley, "Crystalline Ropes of Metallic Carbon Nanotubes," Science, 273 (1996) 483.

[10]   M. A. Kastner, "Artificial atoms," Phys. Today, 46 (1993) 24.

[11]   L. N. Lewis, "Chemical catalysis by colloids and clusters," Chem.Rev., 93 (1993) 2693.

[12]   R. Freer, Nanoceramics, Woodhead, England, (1993)

[13]   N. M. Rodriguez, A. Chambers and R. T. K. Baker, "Catalytic engineering of carbon nanostructures," Langmuir, 11 (1995) 3862.

[14]   K, Ziemelis, "The future of microelectronics," Nature, 406 (2000) 1021.

[15]   H. W. Kroto, J. R. Heath, S. C. Obrien, R. F. Curl, and R. E. Smalley, "C(60): Buckminsterfullerene ((carbon molecule formation in space and stellar envelopes))," Nature, 318 (1985) 162.

[16]   S. Iijima, "Helical microtubules of graphite carbon," Nature, 354 (1991) 56.

[17]   J. W. Mintmire, B. I. Dunlap and C. T. White, "Are fullerene tubules metallic?" J. Phys. Rev. Lett., 68 (1992) 631.

[18]   N. Hamada, S. Sawada and A. Oshiyama, "New one-dimensional conductors:

Graphitic microtubules," J. Phys. Rev. Lett., 68 (1992) 1579.

[19]   J. Tersoff and R. S. Ruoff, "Structural properties of a carbon-nanotube crystal," J. Phys. Rev. Lett., 73 (1994) 676.

[20]   P. Kim, L. Shi, A. Majumdar and P. L. McEuen, "Thermal Transport Measurements of Individual Multiwalled Nanotubes," Phys. Rev. Lett., 87 (2001) 215502.

[21]   G. Gao, T. Cagin and W. A. Goddard III, "Energetics, structure, mechanical and vibrational properties of single-walled carbon nanotubes," Nanotechnology, 9 (1998) 184.

[22]   T. W. Ebbesen, "Carbon nanotube," Phys. Today, 49 (1996) 26.

[23]   P. M. Ajayan and T. W. Ebbesen, "Nanometre-size tubes of carbon," Rep. Prog. Phys., 60 (1997) 1025.

[24]   B. I. Yakobson and R. E. Smalley, "Fullerene nanotubes: C1,000,000 and beyond," Am. Sci., 85 (1997) 324.

[25]   C. Dekker, "Carbon nanotubes as molecular quantum wires," Phys. Today, 52 (1999) 22.

[26]   M. S. Dresselhaus, G. Dresselhaus and P. C. Eklund, "Science of fullerenes and carbon nanotubes," Academic Press, Boston (1996).

[27]   T. W. Ebbesen, Carbon nanotubes: preparation and properties, CRC Press, Boca Raton, FL. (1997).

[28]   K. Tanaka, T. Yamabe and K. Fukui, "The science and technology of carbon nanotubes," Amsterdam, Elsevier (1999).

[29]   E. T. Thostenson, Z. Ren and T. W. Chou, "Advanced in the science and technology of carbon nanotubes and their composites: a review," Composites Science and Technology, 61 (2001) 1899.

[30]   K. Tanaka, K. Okahara, M. Okada and T. Yamabe, "Structure and electronic state of C60," Chem. Phys. Lett., 191 (1992) 469.

[31]   D. Bernaerts, M. Op De Beeck, S. Amelinckx, J. Van Landuyt and G. Van Tendeloo, "The chiralty of carbon nanotubes determined by dark-field electron microscopy," Philos. Mag., A 74 (1996) 723.

[32]   X. F. Zhang, X. B. Zhang, G. Van Tendeloo, S. Amelinckx, M. Op de Beeck and J. Van Landuyt, "Carbon nano-tubes; their formation process and observation by electron microscopy," J. Cryst. Growth, 130 (1993) 3.

[33]   R. Saito, M. Fujita, G. Dresselhaus and M. S. Dresselhaus, "Electronic structure of chiral graphene tubules," Appl. Phys. Lett., 60 (1992) 2204.

[34]   N. Hamada, S. I. Sawada and A. Oshiyama, "New one-dimensional conductors: graphite microtubules," Phys. Rev. Lett., 68 (1992) 1579.

[35]   X. Blase, L. X. Benedict, E. L. Shirley and S. G. Louie, "Hybridization effects and metallicity in small radius carbon nanotubes," Phys. Rev. Lett., 72 (1994) 1878.

[36]   J. W. Mintmire and C. T. White, "Electronic and structural properties of carbon

nanotubes," Carbon, 33 (1995) 893.

[37]   C. L. Kane and E. J. Mele, "Size, shape, and low energy electronic of carbon nanotubes," Phys. Rev. Lett., 78 (1997) 1932.

[38]   P. R. Wallace, "The band theory of graphite," Phys. Rev., 71 (1947) 622.

[39]   J. W. G. Wildöer, L. C. Venema, A. G. Rinzler, R. E. Smalley and C. Dekker, "Electronic structure of atomically resolved carbon nanotubes," Nature, 391 (1998) 59.

[40]   T. W. Odom, J. L. Huang, P. Kim and C. M. Lieber, "Atomic structure and electronic properties of single-walled carbon nanotubes," Nature, 391 (1998) 62.

[41]   L. C. Venema, J. W. G. Wildöer, C. Dekker, A. G. Rinzler and R. E. Smalley, "STM atomic resolution images of single-wall carbon nanotubes," Appl. Phys. A, 66 (1998) S153.

[42]   T. W. Odom, J. L. Huang, P. Kim and C. M. Lieber, "Structure and electronic properties of carbon nanotubes," J. Phys. Chem. B, 104 (2000) 2794.

[43]   L.C. Venema, J.W.G. Wildöer, J.W. Janssen, S.J. Tans, H.L.J. Temminck Tuinstra, L.P. Kouwenhoven and C. Dekker, "Imaging electron wave functions of quantized energy levels in carbon nanotubes," Science, 283 (1999) 52.

[44]   P. Kim, T.W. Odom, J.-L. Huang and C.M. Lieber, "Electronic density of states of atomically resolved single-walled carbon nanotubes: Van Hove singularities and end states," Phys. Rev. Lett., 82 (1999) 1225.

[45]   S.J. Tans, A.R.M. Verschueren and C. Dekker, "Room-temperature transistor based on a single carbon nanotube," Nature, 393 (1998) 49.

[46]   R. Martel, T. Schmidt, H.R. Shea, T. Hertel and Ph. Avouris, "Single- and multi-wall carbon nanotube field effect transistors," Appl. Phys. Lett., 73 (1998) 2447.

[47]   M. Bockrath, D.H. Cobden, P.L. McEuen, N.G. Chopra, A. Zettl, A. Thess and R.E. Smalley, "Single-electron transport in ropes of carbon nanotubes," Science, 275 (1997) 1922.

[48]   S.J. Tans, M.H. Devoret, H. Dai, A. Thess, R.E. Smalley, L.J. Geerligs and C. Dekker, "Individual single-wall carbon nanotubes as quantum wires," Nature, 386 (1997) 474.

[49]   S.J. Tans, M.H. Devoret, R.J.A. Groeneveld and C. Dekker, "Electron-electron correlations in carbon nanotubes," Nature, 394 (1998) 761.

[50]   M. Bockrath, D.H. Cobden, J. Lu, A.G. Rinzler, R.E. Smalley, L. Balents and P.L. McEuen, "Luttinger-liquid behaviour in carbon nanotubes," Nature, 397 (1999) 598.

[51]   A. Bachtold, C. Strunk, J.-P. Salvetat, J.-M. Bonard, L. Forró, T. Nussbaumer and C. Schönenberger, "Aharonov-Bohm oscillations in carbon nanotubes," Nature, 397 (1999) 673.

[52]   H.T. Soh, C.F. Quate, A.F. Morpurgo, C.M. Marcus, J. Kong and H. Dai, "Integrated nanotube circuits: Controlled growth and ohmic contacting of single-walled carbon nanotubes," Appl. Phys. Lett., 75 (1999) 627.

[53]   C. Schönenberger, A. Bachtold, C. Strunk, J.P. Salvetat and L. Forró, "Interference and interaction in multi-wall carbon nanotubes," Appl. Phys. A, 69 (1999) 283.

[54]   J. Kong, C. Zhou, A. Morpurgo, H.T. Soh, C.F. Quate, C. Marcus and H. Dai, "Synthesis, integration, and electrical properties of individual single-walled carbon nanotubes," Appl. Phys. A, 69 (1999) 305.

[55]   K. Liu, M. Burghard, S. Roth and P. Bernier, "Conductance spikes in single-walled carbon nanotube field-effect transistor," Appl. Phys. Lett., 75 (1999) 2494.

[56]   P.L. McEuen, M. Bockrath, D.H. Cobden, Y.G. Yoon and S.G. Louie, "Disorder, pseudospins, and backscattering in carbon nanotubes," Phys. Rev. Lett. 83 (1999) 5098.

[57]   H. Dai, E.W. Wong and C.M. Lieber, "Probing electrical transport in nanomaterials: conductivity of individual carbon nanotubes," Science, 272 (1996) 523.

[58]   L. Langer, V. Bayot, E. Grivei, J.-P. Issi, J.P. Heremans, C.H. Olk, L. Stockman, C. Van Haesendonck and Y. Bruynseraede, "Quantum transport in a multiwalled carbon nanotubes," Phys. Rev. Lett., 76 (1996) 479.

[59]   T.W. Ebbesen, H.J. Lezec, H. Hiura, J.W. Bennett, H.F. Ghaemi and T. Thio, "Electrical conductivity of individual carbon nanotubes," Nature, 382 (1996) 54.

[60]   J.-M. Bonard, H. Kind, T. Stöckli and L.O. Nilsson, "Field emission from carbon nanotubes: the first five years," Solid State Electronics, 45 (2001) 893.

[61]   A. V. Melechko, V. I. Merkulov, T. E. McKnight, M. A. Guillorn, K. L. Klein, D. H. Lowndes and M. L. Simpson, "Vertically aligned carbon nanofibers and related structures:Controlled synthesis and directed assembly," J. Appl. Phys., 97 (2005) 041301.

[62]   T. V. Hughes and C. R. Chambers, Manufacture of Carbon Filaments, US Patent No. 405, 480, (1889).

[63]   R. T. K. Baker and P. S. Harris, "Chemistry and Physics of Carbon," Marcel Dekker, New York, (1978).

[64]   H. W. Kroto, J. R. Heath, S. C. Obrien, R. F. Curl, and R. E. Smalley, "C(60): Buckminsterfullerene ((carbon molecule formation in space and stellar envelopes))," Nature, 318 (1985) 162.

[65]   Y. Chen, Z. L. Wang, J. S. Yin, D. J. Johnson, and R. H. Prince, "Well-aligned graphitic nanofibers synthesized by plasma-assisted chemical vapor deposition," Chem. Phys. Lett., 272 (1997) 178.

[66]   Z. F. Ren, Z. P. Huang, J. W. Xu, J. H. Wang, P. Bush, M. P. Siegal, and P. N. Provencio, "Synthesis of Large Arrays of Well-Aligned Carbon Nanotubes on Glass," Science, 282 (1998) 1105.

[67] A. Krishnan, E. Dujardin, M. M. J. Treacy, J. Hugdahl, S. Lynum, and T. W. Ebbesen, "Graphitic cones and the nucleation of curved carbon surfaces," Nature, 388 (1997) 451.

[68] M. Endo, Y. A. Kim, T. Hayashi, Y. Fukai, K. Oshida, M. Terrones, T. Yanagisawa, S. Higaki and M. S. Dresselhaus, "Structural characterization of cup-stacked-type nanofibers with an entirely hollow core," Appl. Phys. Lett., 80 (2002) 1267.

[69] C. F. Chen, C. L. Lin and C. M. Wang, "Field emission from aligned carbon nanofibers grown in situ by hot filament chemical vapor deposition," Appl. Phys. Lett., 82 (2003) 2515.

[70] V. I. Merkulov, A. V. Melechko, M. A. Guillorn, D. H. Lowndes, and M. L. Simpson, "Effects of spatial separation on the growth of vertically aligned carbon nanofibers produced by plasma-enhanced chemical vapor deposition," Appl. Phys. Lett., 80 (2002) 476.

[71] M. A. Guillorn, A. V. Melechko, V. I. Merkulov, D. K. Hensley, M. L. Simpson and D. H. Lowndes, "Self-aligned gated field emission devices using single carbon nanofiber cathodes," Appl. Phys. Lett., 81 (2002) 3660.

[72] S. Bhattacharyya and S. V. Subramanyam, "Metallic conductivity of amorphous carbon films under high pressure," Appl. Phys. Lett., 632 (1997) 71.

[73] C. J. Huang, Y. K. Chih, J. Hwang, A. P. Lee and C. S. Kou, "Field emission from amorphous-carbon nanotips on copper," J. Appl. Phys., 94 (2003) 6796.

[74] K. S. Yeong, C. B. Boothroyd and J. T. L. Thong, "The growth mechanism and field-emission properties of single carbon nanotips," Nanotechnology, 17 (2006) 3655.

[75] H. Adachi, H. Nakane and M. Katamoto, "Field emission characteristics of a carbon needle made by use of electron-beam-assisted decomposition of methane," Appl. Surf. Sci., 76/77 (1994) 11.

[76] S. D. Johnson, D. G. Hasko, K. B. K. Teo, W. I. Milne and H. Ahmed, "Fabrication of carbon nanotips in a scanning electron microscope for use as electron field emission sources," Microelectron. Eng., 61/62 (2002) 665.

[77] Y. Akama, E. Nishimura, A. Sakai and H. Murakami, "New scanning tunneling microscopy tip for measuring surface topography," J. Vac. Sci. Technol. A, 8 (1990) 429.

[78] G. Y. Zhang, X. Jiang and E. G. Wang, "Tubular Graphite Cones," Science, 300 (2003) 472.

[79] R. C. Mani, X. Li, M. K. Sunkara and K. Rajan," Carbon nanopipettes," Nano Lett., 3 (2003) 671.

[80] J. J. Li, C. Z. Gu, Q. Wang, P. Xu, Z. L. Wang, Z. Xu and X. D. Bai, "Field emission from high aspect ratio tubular carbon cones grown on gold wire," Appl. Phys. Lett., 87 (2005) 143107.

[81]   L. R. Baylor, V. I. Merkulov, E. D. Ellis, M. A. Guillorn, D. H. Lowndes, A. V. Melechko, M. L. Simpson and J. H. Whealton, "Field emission from isolated individual vertically aligned carbon nanocones," J. Appl. Phys., 91 (2002) 4602.

[82]   C. L. Tsai, C. F. Chen, and C. L. Lin, "Field emission from well-aligned carbon nanotips grown in a gated device structure ," Appl. Phys. Lett., 80 (2002) 1821.

[83]   C. L. Tsai, C. F. Chen, and L. K. Wu, "Bias effect on the growth of carbon nanotips using microwave plasma chemical vapor deposition," Appl. Phys. Lett., 81 (2002) 721.

[84]   S. Iijima and T. Ichihashi, "Single-shell carbon nanotubes of 1-nm diameter," Nature, 363 (1993) 603.

[85]   P. M. Ajayan, J. M. Lambert, P. Bernier, C. Colliex and J. M. Planeix, "Growth morphologies during cobalt-catalyzed single-shell carbon nanotube synthesis," Chem, Phys, Lett., 215 (1993) 509.

[86]   S. Seraphin and D. Zhou, "Single-walled carbon nanotubes produced at high yield by mixed catalysts," Appl. Phys. Lett., 64, 2087 (1994)

[87]   T. W. Ebbesen, Carbon Nanotubes –Preparation and properties, CRC Press, New York (1997)

[88]   T. Guo, P. Nikolaev, A. Thess, D. T. Colbert and R. E. Smalley, "Catalytic growth of single-walled nanotubes by laser vaporization," Chem. Phys. Lett., 243 (1995) 49.

[89]   T. Guo, P. Nikolaev, A. G. Rinzler, D. Tomanek, D. T. Colbert and R. E. Smalley, "Self-Assembly of Tubular Fullerenes," J. Phys, Chem., 99 (1995) 10694.

[90]   B. I. Yakobson and R. E. Smalley, ""Fullerene nanotubes: $C_{1000,000}$ and beyond," American Scientist 85 (1997) 324.

[91]   D. Robertson, "Carbon formation from methane pyrolysis over some transition metal surfaces," Carbon, 8 (1970) 365.

[92]   T. Baird, J. R. Frayer and B. Grant, "Structure of Fibrous Carbon," Nature, 233 (1971) 329.

[93]   M. J. Yacaman, M. M. Yoshida, L. Rendon and J. G. Santiesteben, "Catalytic growth of carbon microtubules with fullerene structure," Appl. Phys. Lett., 62 (1993) 202.

[94]   Y. Chen, Z. L. Wang, J. S. Yin, D. J. Johnson and R. H. Prince, "Well-aligned graphitic nanofibers synthesized by plasma-assisted chemical vapor deposition," Chem. Phys. Lett., 272 (1997) 178.

[95]   L. C. Qin, D. Zhou, A. R. Krauss and D. M. Gruen, "Growing carbon nanotubes by microwave plasma-enhanced chemical vapor deposition," Appl. Phys. Lett., 72 (1998) 3437.

[96]   C. Laurent, E. Flahaut, A Peigney and A. Rousset, "Metal nanoparticles for the catalytic synthesis of carbon nanotubes," New J. Chem., 1229 (1998).

[97]   C. F. Chen, C. L. Tsai and C. L. Lin, "Characterization of phosphorus-doped and boron-doped diamond-like carbon emitter arrays," J. Appl. Phys., 90 (2001) 4847.

[98] A. Grill, <u>Cold Plasma in Materials Fabrication</u>. IEEE Press, New York (1993).

[99] D. A. Carl, D. W. Hess, M. A. Lieberman, T. D. Nguyen and R. Gronsky, "Effects of dc bias on the kinetics and electrical properties of silicon dioxide grown in an electron cyclotron resonance plasma," J. Appl. Phys., 70 (1991) 3301.

[100] A. Gorbunov, O. Jost, W. Pompe and A. Graff, "Solid–liquid–solid growth mechanism of single-wall carbon nanotubes," Carbon, 40 (2002) 113.

[101] R. S. Wagner and W. C. Ellis, "Vapor-liquid-solid mechanism of single crystal growth," Appl. Phys. Lett., 4 (1964) 89.

[102] G. G. Tibbetts, "Why are carbon filaments tubular?" J. Cryst. Growth, 66 (1984) 632.

[103] Y. Saito, T. Yoshikawa, M. Inagaki, M. Tomita and T. Hayashi, "Growth and structure of graphitic tubules and polyhedral particles in arc-discharge," Chem. Phys. Lett., 204 (1993) 277.

[104] Y. Saito, "Nanoparticles and filled nanocapsules," Carbon, 33 (1995) 979.

[105] T. J. Trentler, K. M. Hickman, S. C. Goel, A. M. Viano, P. C.Gibbons and W. E. Buhro, "Solution-liquid-solid growth of crystalline III-V semiconductors: An analogy to vapor-liquid-solid growth," Science, 270 (1995) 1791.

[106] T. J. Trentler, K. M. Hickman, S. C. Goel, A. M. Viano, P. C.Gibbons, W. E. Buhro, M. Y. Chiang and A. M. Beatty, "Solution-Liquid-Solid Growth of Indium Phosphide Fibers from Organometallic Precursors: Elucidation of Molecular and Nonmolecular Components of the Pathway," J. Am. Chem. Soc. 119 (1997) 2172.

[107] R. Gomer, <u>Field Emission and Field Ionization</u>, Harvard University Press, Cambridge, MA (1961)

[108] D. Temple, "Recent progress in field emitter array development fpr high performance applications," Mat. Sci. Eng., R24 (1999) 185.

[109] R.H. Fowler and L. Nordheim, "Electron Emission in Intense Electric Fields," Roy. Soc. Proc. A, (1928) 173 .

[110] R. Gomer, <u>Field Emission and Field Ionization</u>, Harvard University Press, Cambridge, MA, 1961.

[111] R. Stratton, "Field Emission from Semiconductors," Proc. Phys. Soc. London B, 68 (1955) 746.

[112] N.A. Cade, R. Johnston, A. J. Miller, and C. Patel, "Studies into the emission uniformity of large silicon field emitter arrays," J. Vac. Sci. Technol. B, 13 (1995) 549.

[113] R. Greene and H.F. Gray, "A simple theory of semiconductor field emission saturation," Proc. 1st Int. Vacuum Microelectronics Conf., Williamsburg, VA (1988).

[114] L.M. Baskin, O.I. Lvov and G.N. Fursey, "Theory of Field Emission From p-Type Semiconductors," Phys. Stat. Sol., 47 (1971) 49.

[115] H.F. Gray, G.J. Campisi and R.F. Greene, "A vacuum field effect transistor using silicon field emitter arrays," Technical Digest of the IEDM, 86 (1986) 776.

[116] S. Kanemaru, T. Hirano, H. Tanoue, J. Itoh, "Control of emission characteristics of silicon field emitter arrays by an ion implantation technique," J. Vac. Sci. Technol., B 14 (1996) 1885.

[117] K.L. Jensen and A.K. Ganguly, "Numerical simulation of field emission from silicon," J. Vac. Sci. Technol. B 11 (1993) 371.

[118] K.L. Jensen and A.K. Ganguly, "Time dependent, self-consistent simulations of field emission from silicon using the Wigner distribution function," J. Vac. Sci. Technol. B 12 (1994) 770.

[119] K.L. Jensen, "Improved Fowler–Nordheim equation for field emission from semiconductors," J. Vac. Sci. Technol. B 13 (1995) 516.

[120] L. Nilsson, O. Groening, C. Emmenegger, O. Kuettel, E. Schaller, L. Schlapbach, H. Kind, J. M. Bonard and K. Kern, "Scanning field emission from structured carbon nanotube films," Appl. Phys. Lett., 76 (2000) 2071.

[121] Y. Tu, Z. P. Huang, D. Z. Wang, J. G. Wen and Z. F. Ren, "Growth of aligned carbon nanotubes with controlled site density," Appl. Phys. Lett., 80 (2002) 4018.

[122] F. Tuinstra and J. L. Koenig, "Raman Spectrum of Graphite," J. Chem. Phys., 53 (1970) 1126

[123] A. C. Ferrari and J. Robertson, "Interpretation of Raman spectra of disordered and amorphous carbon," Phys. Rev. B., 61 (2000) 14095

[124] J. Kastner, T. Pichlert, H. Kuzmany, S. Curran, W. Blau, N. Weldon, M. Delamesiere, S. Draper and H. Zandbergen "Resonance Raman and infrared spectroscopy of carbon nanotubes," Chem. Phys. Lett., 221 (1994) 53

[125] A. Thess, R. Lee, P.Nikolaev, H. Dai, P. Petit, J. Robert, C. Xu, Y. J. Lee, S. G. Kim, A. G. Rinzler, D. T. Colbert, G. E. Scuseria, D. Tomanek, J. E. Fischer and R. E. Smalley, Science, 273, 483 (1996)

[126] E. Flahaut, A. Govindaraj, A. Peigney, Ch. Laurent, A. Rousset and C. N. R. Rao, "Synthesis of single-walled carbon nanotubes using binary (Fe, Co, Ni) alloy nanoparticles prepared in situ by the reduction of oxide solid solutions" Chem. Phys. Lett., 300 (1999) 236.

[127] C. J. Lee, J. Park and J. A. Yu, "Catalyst effect on carbon nanotubes synthesized by thermal chemical vapor deposition," Chem. Phys. Lett., 360 (2002) 250.

[128] S. H. Tsai, C. W. Chao, C. L. Lee, and H. C. Shih, "Bias-enhanced nucleation and growth of the aligned carbon nanotubes with open ends under microwave plasma synthesis," Appl. Phys. Lett. 74 (1999) 3462.

[129] H. Machida, S. Honda, S. Fujii, K. Himuro, H. Kawai, K. Ishida, K. Oura and M. Katayama, "Effect of Electrical Aging on Field Electron Emission from Screen-Printed Carbon Nanotube Film," Jap. J. Appl. Phys., 46 (2007) 867.

[130] J. M. Kim, W. B. Choi, N. S. Lee and J. E Jung, " Field emission from carbon nanotubes for displays" Diamond Relat. Mater., 9 (2000) 1184.

[131] J. Wong-Leung, D. J. Eaglesham, J. Sapjeta, D. C. Jacobson, J. M. Poate and J. S. Williams, "The precipitation of Fe at the Si–SiO$_2$ interface," J. Appl. Phys. 83 (1998) 580.

[132] W. B. Henley, L. Jastrzebski and N. F. Haddad, "Effects of iron contamination in silicon on thin oxide breakdown and reliability characteristics," J. non-cryst. Solids, 187 (1995) 134.

[133] A. A. Istratov, H. Hieslmair and E.R. Weber, "Iron contamination in silicon technology," Appl. Phys. A: Mater. Sci. Proc. 70 (2000) 489.

[136] J. C. She, N. S. Xu, S. Z. Deng, Jun Chen, H. Bisjop, S. E. Huq, L. Wang, D. Y. Zhong and E. G. Wang, "Vacuum breakdown of carbon-nanotube field emitters on a silicon tip," Appl. Phys. Lett., 83 (2003) 2671.

[137] H. Dai, E. W. Wong, and C. M. Lieber, "Probing electrical transport in nanomaterials: Conductivity of individual carbon nanotubes," Science, 272 (1996) 523.

[138] S. Frank, P. Poncharal, Z. L. Wang, and W. A. De Heer, "Carbon nanotube quantum resistors," Science, 280 (1998) 744.

[139] M. Kasu and N. Kobayashi, "Large and stable field-emission current from heavily Si-doped AlN grown by metalorganic vapor phase epitaxy," Appl. Phys. Lett., 76 (2000) 2910.

[140] C. M. Chen , M. Chen , F. C. Leu , S. Y. Hsu , S. C. Wang , S. C. Shi and C. F. Chen, "Purification of multi-walled carbon nanotubes by microwave digestion method," Diamond Relat. Mater., 13 (2004) 1182.

[141] C.F. Chen, C. L. Tsai and C. L. Lin, "Field emission from well-aligned carbon nanotips grown in a gated device structure," Diamond Relat. Mater., 12 (2003) 1500.

[142] L. Nilsson, O. Groening, C. Emmenegger, O. Kuettel, E. Schaller, L. Schlapbach, H. Kind, J. M. Bonard and K. Kern, "Scanning field emission from structured carbon nanotube films," Appl. Phys. Lett., 76 (2000) 2071.

[143] Y. Tu, Z. P. Huang, D. Z. Wang, J. G. Wen and Z. F. Ren, "Growth of aligned carbon nanotubes with controlled site density," Appl. Phys. Lett., 80 (2002) 4018.

[144] J. S. Suh, K. S. Jeong and J. S. Lee, "Study of the field-screening effect of highly ordered carbon nanotube arrays," Appl. Phys. Lett., 80 (2002) 2392.

[145] C. Y. Zhi, X. D. Bai and E. G. Wang, "Enhanced field emission from carbon nanotubes by hydrogen plasma treatment," Appl. Phys. Lett., 81 (2002) 1690.

[146] J. H. Choi, S. H. Choi, J. H. Han, J. B. Yoo, C. Y. Park, T. Jung, S.Yu, I. T. Han and J. N. Kim, "Enhanced electron emission from carbon nanotubes through density control using *in situ* plasma treatment of catalyst metal," J. Appl. Phys., 94 (2003) 487.

[147] Y. B. Zhu, W. L. Wang, K. J. Liao and Y. Ma, "Theoretical analysis of external diameter distributions of carbon nanotubes by CVD," Diamond Relat. Mater. 12 (2003) 1862.

[148] C. H. Hsu, S. C. Shi and C. F. Chen, "Growth of chromium carbide capped–carbon nanotip using bias-assisted microwave plasma chemical vapor deposition," Thin Solid Film, 469/470 (2004) 131.

[149] Y. Saito, T. Yoshikawa, M. Inagaki, M. Tomita and T. Hayashi, "Growth and structure of graphitic tubules and polyhedral particles in arc-discharge," Chem. Phys. Lett., 204 (1993) 277.

[150] P. Lambin, J. P Vigneron, A. Fonseca, J. B. Nagy and A. A. Lucas, "Atomic structure and electronic properties of a bent carbon nanotube," Synthetic Metals 77 (1996) 249.

[151] C.L. Tsai and C.F. Chen, "Characterization of bias-controlled carbon nanotubes," Diamond Relat. Mater., 12 (2003) 1615.

[152] D. P. Yu, Q. L. Hang, Y. Ding, H. Z. Zhang, Z. G. Bai, J. J. Wang, Y. H. Zou, W. Qian, G. C. Xiong, and S. Q. Feng, "Amorphous silica nanowires: Intensive blue light emitters," Appl. Phys. Lett., 73 (1998) 3076.

[153] M. Paulose, O. K. Varghese, and C. A. Grimes, "Synthesis of gold-silica composite nanowires through solid-liquid-solid phase growth," J. Nanosci. Nanotechnology, 3 (2003) 341.

[154] Z. W. Pan, S. Dai, D. B. Beach, and D. H. Lowndes, "Temperature Dependence of Morphologies of Aligned Silicon Oxide Nanowire Assemblies Catalyzed by Molten Gallium," Nano Lett., 3 (2003) 1279.

[155] Z. W. Pan, S. Dai, D. B. Beach, and D. H. Lowndes, "Liquid gallium ball/crystalline silicon polyhedrons/aligned silicon oxide nanowires sandwich structure: An interesting nanowire growth route," Appl. Phys. Lett., 84 (2003) 3159.

[156] T. J. Trentler, K. M. Hickman, S. C. Goel, A. M. Viano, P. C.Gibbons, and W. E. Buhro, "Solution-liquid-lolid growth of crystalline III-V semiconductors: An analogy to vapor-liquid-solid growth," Science, 270 (1995) 1791.

[157] S. H. Christiansen, M. Becker, S. Fahlbusch, J. Michler, V. Sivakov, G. Andra, and R. Geiger, Signal enhancement in nano-Raman spectroscopy by gold caps on silicon nanowires obtained by vapour–liquid–solid growth," Nanotechnology, 18 (2007) 035503.

[158] E. J. Bjerneld, F. Svedberg, and M. Kall, "Laser-induced growth and deposition of noble-metal nanoparticles for surface-enhanced Raman scattering," Nano Lett., 3 (2003) 593.

[159] A. Tao, F. Kim, C. Hess, J. Goldberger, R. He, Y. Sun, Y. Xia, and P. Yang, "Langmuir-Blodgett silver nanowire monolayers for molecular sensing using surface-enhanced raman spectroscopy," Nano Lett., 3 (2003) 1229.

[160]   Duwez, R. H. Willens, and W. Klement Jr., "Continuous series of metastable solid solutions in silver-copper alloys," J. Appl.. Phys., 31 (1960) 1136.

[161]   Z. F. Ren, Z. P. Huang, J. W. Xu, J. H. Wang, P. Bush, M. P. Siegal and P. N. Provencio, "Synthesis of large arrays of well-aligned carbon nanotubes on glass," Science, 282 (1998) 1105.

[162]   W. Z. Li, S. S. Xie, L. X. Qian, B. H. Chang, B. S. Zou, W.Y . Zhou, R. A. Zhao and G. Wang, "Large-scale synthesis of aligned carbon nanotubes," Science, 274 (1996) 1701.

[163]   S. Fan, M.G. Chapline, N.R. Franklin, T.W. Tombler, A.M. Casell and H. Dai, "Self-oriented regular arrays of carbon nanotubes and their field emission properties," Science, 283 (1999) 512.

[164]   C. L. Tsai, J. H. Hsu, and C. F. Chen, "Self-embedded nanocrystalline chromium carbides on well-aligned carbon nanotips," Appl. Phys. Lett., 82 (2003) 4337.

[165]   L. C. Chen, C. Y. Wen, C. H. Lian, W. K. Hong, K. J. Chen, H. C. Chen, C. S. Shen, C. T. Wu and K. H. Chen, "Controlling steps during early stages of the aligned growth of carbon nanotubes uing microwave plasma enhanced chemical vapor Deposition," Adv. Func. Mat., 12 (2002) 687.

[166]   P.K. Rajagopalan , T.S. Krishnan and D.K. Bose, "Development of carbothermy for the preparation of hepta chromium carbide," J. Alloy Compd, 297 (2002) L1.

[167]   R. G. Coltters and G. R. Belton, "High temperature thermodynamic properties of the chromium carbides Cr_7C_3 and Cr_3C_2 determined using a Galvanic cell tehcniqe," Metall. Trans. B, 15 (1983) 517.

[168]   C. F. Chen, C. L. Lin, and C. M. Wang, "Field emission from aligned carbon nanofibers grown *in situ* by hot filament chemical vapor deposition," Appl. Phys. Lett., 82 (2003) 2515.

[169]   E. F. Kukovitsky, S. G. L'vov and N. A. Sainov, "Correlation between metal catalyst particle size and carbon nanotube growth," Chem. Phys. Lett., 317 (2000) 65.

[170]   D. B. Hash and M. Meyyappan, "Model based comparison of thermal and plasma chemical vapor deposition of carbon nanotubes," J. Appl. Phys., 93 (2003) 750

[171]   D. A. Carl, D. W. Hess, M. A. Lieberman, T. D. Nguyen and R. Gronsky, "Effects of dc bias on the kinetics and electrical properties of silicon dioxide grown in an electron cyclotron resonance plasma." J. Appl. Phys. Lett., 70 (1991) 3301.

[172]   C. T. Fu, J. M. Wu and A. K. Li, "Microstructure and mechanical properties of Cr_3C_2 particulate reinforced Al_2O_3 matrix composites," J. Mat. Sci., 29 (1994) 2671.

[173]   D. Music, U. Kreissig, R. Mertens and J. M. Schneider, "Electronic structure and mechanical properties of Cr_7C_3," Phys. Lett. A, 326 (2004) 473.

[174]   Y. Show, F. Matsuoka, M. Hayashi, H. Ito, M. Iwase and T. Izumi, "Influence of defects on electron emission from diamond films," J. Appl. Phys., 84 (1998) 6351.

[175]   K. H. Park, W. J. Seo, S. Lee, and K. H. Koh, "Triode field emitter with a gated

planar carbon-nanoparticle cathode," Apply. Phys. Lett. 81 (2002) 358.

[176] E. Yamaguchi, K. Sakai, I. Nomura, T. Ono, M. Yamanobe, N. Abe, T. Hara, K. Hatanaka, Y. Osada, H. Yamamoto and T. Nakagiri, "A 10-in. surface-conduction electron-emitter display," J. SID, 5 (1997) 345.

[177] E. T. Turdogan, <u>Physical Chemistry of High Temperature Technology</u>, Academic Press, New York, 1980.

List of Publications

Journal Papers

1. <u>Cheng-Hang Hsu</u>, Shih-Shi Chen and Chia-Fu Chen, Growth of chromium carbide capped carbon nanotip using bias-assisted microwave plasma chemical vapor deposition, Thin Solid Films, 469 (2004) 131.

2. <u>Cheng-Hang Hsu</u>, Chia-Fu Chen, Chien-Chung Chen and Shih-Yu Chan, Density controlled carbon nanotubes, Diamond and Related Materials, 14 (2005) 739.

3. Chien-Chung Chen, Chia Fu Chen, <u>Cheng-Hang Hsu</u> and I-Hsuan Li, Growth and characteristics of carbon nanotubes on carbon cloth as electrodes, Diamond and Related Materials, 14 (2005) 770.

4. <u>Cheng-Hang Hsu</u> and Chia-Fu Chen, Field emission characteristics of chromium carbide capped carbon nanotips, Thin solid films, 515 (2006) 1025.

5. <u>Cheng-Hang Hsu</u>, Shih-Yu Chan, and Chia-Fu Chen, Structural evolution of silicon oxide nanowires via head-growth solid-liquid-solid Process, Japanese Journal of Applied Physics, 46 (2007).

Conference Papers and Presentations

1. 奈米碳尖錐上自組碳化鉻晶粒之成長與研究, 中華民國鍍膜科技研討會暨國科會計畫研究成果發表會 2003.

2. Growth of chromium carbide capped carbon nanotip using bias-assisted microwave plasma chemical vapor deposition, The International Conference on Metallurgical Coatings and Thin Films, San Diego, CA, USA. 2004.

3. Density controlled carbon nanotubes, 15th European Conference on Diamond, Diamond-Like Materials, Carbon Nanotubes, Nitrides & Silicon Carbide, Riva del Garda, Italy 2004.

4. Field emission from chromium carbide capped carbon nanotips, The 3rd Asian Conference on Chemical Vapor Deposition, Taipei, Taiwan. 2004.

5. 奈米碳管成長之密度控制，台灣鍍膜科技研討會暨國科會計畫研究成果發表會 2005.

6. High efficient and stable field emission from self-assembled chromium carbide carbon nanotips, The International Conference on Metallurgical Coatings and Thin Films, San Diego, CA, USA. 2006.

學經歷資料

- 姓名：徐振航
- 性別：男
- 生日：68 年 2 月 15 日，桃園人
- 電子郵件信箱：gooddaytosleep@yahoo.com.tw
- 聯絡電話：0939129264
- 永久地址：338 桃園縣蘆竹鄉大竹村南竹路五段 134-1 號

學歷

學位	就讀系所	論文題目	指導教授	起迄
博士	國立交通大學材料科學與工程學系暨研究所	奈米碳材料之場發射特性與應用之研究	陳家富博士	2003.9 ~ 2007.11
碩士	國立交通大學材料科學與工程學系暨研究所	奈米碳尖錐上自組碳化鉻晶粒之成長與研究	陳家富博士	2001.9 ~ 2003.6
學士	成功大學材料科學及工程學系	尋求內電極為鎳銅之積層陶瓷電容的低溫燒結助劑	方倉澤博士	1997.9 ~ 2001.6

專長

研究專長：

1. 物理氣相沈積、化學氣相沈積。
2. 奈米合成、薄膜分析技術。
3. 顯示器技術

儀器操作：

製程儀器：磁控濺鍍物理氣相沈積、微波電漿化學氣相沈積、電子迴旋共振化學氣相沈積、高溫爐管。

分析儀器：拉曼光譜儀、掃瞄式電子顯微鏡、穿透式電子顯微鏡、原子力顯微鏡、X 光繞射儀。